Spring 3-1-1982

Aperture Admittance and Dispersion Characteristics of an Open-End Microstrip Transmission Line

Robert T. Johnk
University of Colorado Boulder

Scientific Report No. 70

APERTURE ADMITTANCE AND DISPERSION CHARACTERISTICS OF AN OPEN-END MICROSTRIP TRANSMISSION LINE

by

Robert T. Johnk†

March 1982

Electromagnetics Laboratory
Department of Electrical Engineering
University of Colorado
Boulder, Colorado 80309

†This report is based on the author's M.S. Thesis

This research was supported in part by the Office of Naval Research under contract no. N00014-76-C-0318 and the National Science Foundation under grant no. NSF 7809029.

TABLE OF CONTENTS

LIST OF TABLES

LIST OF FIGURES

Figure Page

Figure Page

CHAPTER I

INTRODUCTION

During the past ten years, printed-circuit antennas have come into widespread use. The most commonly used type is the rectangular microstrip patch antenna. A number of models have been developed for the design of rectangular patches [4,9,10], but these fail to account rigorously for the fringe fields, radiation effects, and the dispersion that is created by the presence of a dielectric substrate. At lower operating frequencies where the patch dimensions can be easily adjusted, the deficiencies in these models do not create serious design problems. Because of advantages inherent in using higher frequencies, microstrip antennas will become widely used at millimeter wavelengths. At such short wavelengths, the dimensions of patch elements become quite small so its dimensions cannot be readily adjusted with techniques consistent with current fabrication processes. Thus, at higher frequencies, the accurate design of patch elements becomes much more critical which means the line dispersion, radiation effects, and the fringe fields must be more accurately modeled.

In order to provide a more rigorous accounting of these effects, Chang and Kuester [1] have solved the canonical problem of an obliquely incident TEM wave underneath a semi-infinite patch supported by an infinite dielectric slab. The solution of this

problem rigorously accounts for the surface wave effects, fringe fields, and radiation. Chang [2] applies the solution of the canonical problem to an unloaded rectangular patch. This model accounts for the dispersion of the microstrip patch, and it results in radiating edge admittances that are a function of the dispersion, frequency of operation, and the dielectric slab parameters. The resulting admittances then are dynamic in nature.

Chang's formulation contrasts with the conventional approach where the edge conductance and susceptance are separately evaluated from a slot radiation calculation and a static fringing capacitance computation. Clearly, the slot radiation calculation does not account for the dispersive effects of the microstrip line, nor does it take into account surface waves that can be supported by the dielectric slab. Also, calculating the susceptance from a static formulation does not account for any high-frequency effects at all. It therefore appears the conventional edge admittance is inadequate to describe microstrip edge phenomena.

Thus, the purpose of this thesis is to investigate the admittance and dispersion characteristics as predicted by the Chang-Kuester model and to test the validity of this model. The thesis is divided into three major parts covered in five chapters. In the first portion, the theory of Chang and Kuester is discussed, and is applied to microstrip transmission line structures. Numerical, graphical, and analytical results pertaining to this formulation are presented and discussed. In the second part, the widely used conventional admittance formulation is presented, and numerical as

well as analytical results are given. The third and final portion consists of the construction of an experimental setup designed to provide accurate dispersion and edge admittance data. A number of microstrip transmission line configurations are investigated, and the experimental results are compared with the theoretical results of the Chang-Kuester model and the conventional admittance formulation. On the basis of this comparison, conclusions are then drawn about the validity of these two approaches.

CHAPTER II

THE WIENER-HOPF SOLUTION AND THE OPEN-END MICROSTRIP TRANSMISSION LINE

2.1. Introduction

This chapter deals with the application of the Wiener-Hopf solution of Chang and Kuester to the modeling of the dispersion characteristics and the open end admittance of an electrically wide microstrip transmission line. In the first portion of this chapter, the solution of the canonical problem of a semi-infinite microstrip is presented. This solution is first used to characterize the propagating modes that can exist on a microstrip transmission line with an infinitely long top conductor of finite width. The next problem that is dealt with is a semi-infinite microstrip transmission line with a finite width top conductor that is terminated in an open circuit. This problem is used in conjunction with the Weiner-Hopf solution to define and characterize the end admittance of an open-circuited microstrip transmission line. In the final portion of this chapter, the concept of equivalent length is introduced and developed. Throughout this chapter, numerical, analytical, and graphical results are presented.

2.2. The Canonical Problem and The Wiener-Hopf Solution

In Fig. 2.1, a perfectly conducting ground plane supports a dielectric substrate of infinite extent and thickness d. The substrate has a relative permittivity ε_r and is assumed to be non-magnetic. On top of the dielectric material, there is a perfectly conducting, semi-infinite patch of zero thickness. A TEM wave, inside the parallel plate region, is incident at an angle ϕ with respect to a line drawn normal to the edge of the top conductor. At a sufficient distance from the edge, the reflected wave is TEM, reflected back at an angle of ϕ, since the higher order waveguide type modes, generated at the discontinuity decay rapidly underneath the patch. The incident electric and magnetic fields are given by

$$E_z^i = \exp\{-jk_o[\alpha x - \sqrt{n^2 - \alpha^2}\, y]\} \tag{2.1}$$

$$\bar{H}_t^i = \frac{-1}{\eta_o}\,[\bar{a}_x\sqrt{n^2 - \alpha^2} + a_y\alpha]\exp\{-jk_o[\alpha x - \sqrt{n^2 - \alpha^2}\, y]\} \tag{2.2}$$

where

$$n = \sqrt{\varepsilon_r}$$

$$\alpha = n \sin\phi \ .$$

The reflected fields are given by

$$E_z^r = \hat{\Gamma} \exp\{-jk_o[\alpha x + \sqrt{n^2 - \alpha^2}\, y]\} \tag{2.3}$$

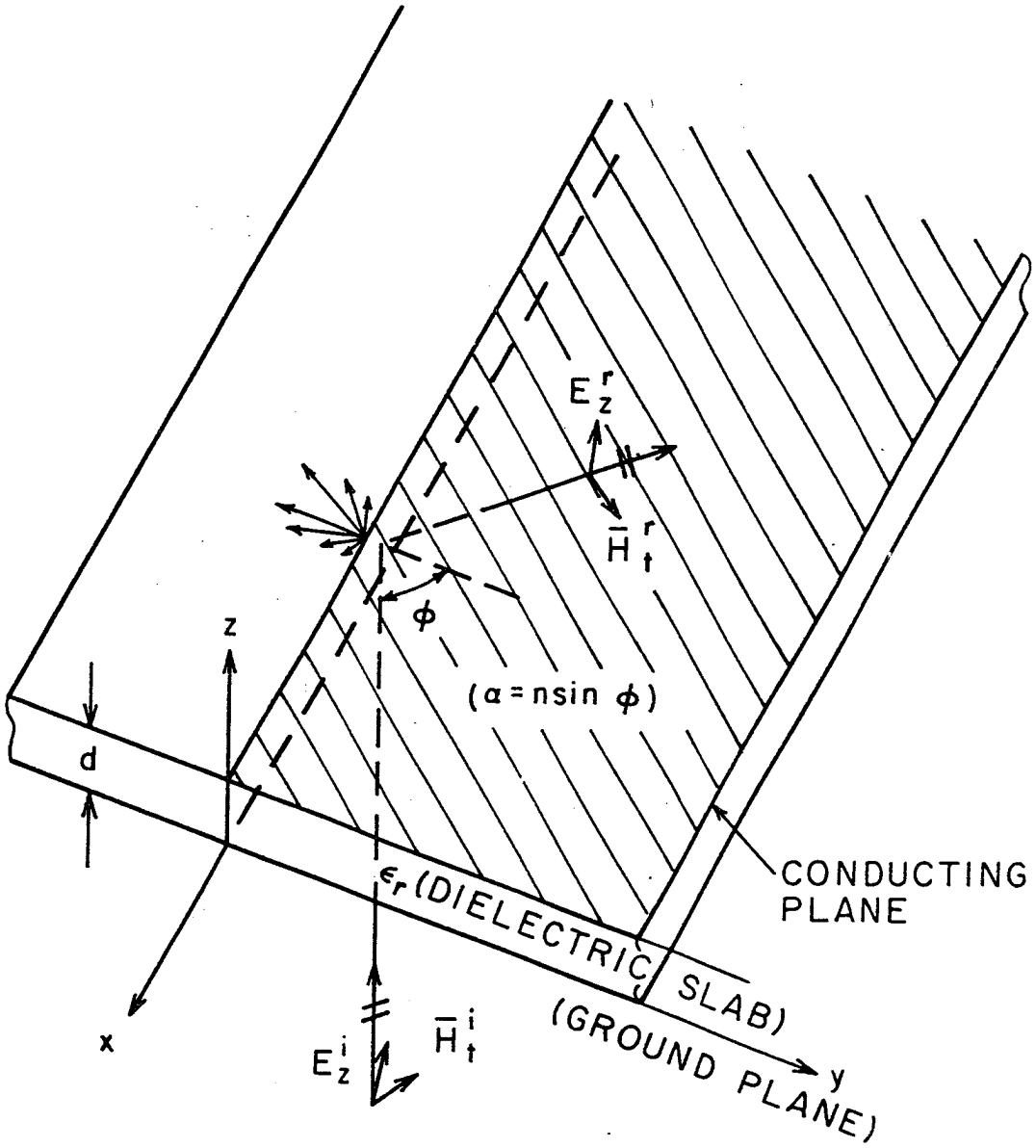
E_z^r
$\bar{H}_t^r$
ϕ
$(\alpha = n\sin\phi)$
z
d
x
ϵ_r (DIELECTRIC SLAB)
(GROUND PLANE)
y
CONDUCTING PLANE
E_z^i
$\bar{H}_t^i$

Fig. 2.1.

$$\bar{H}_t^r = \frac{\hat{\Gamma}}{\eta_o}\left[\bar{a}_x\sqrt{n^2 - \alpha^2} - \bar{a}_y\alpha\right]\exp\{-jk_o[\alpha x - \sqrt{n^2 - \alpha^2}\, y)\} \quad . \qquad (2.4)$$

In these equations, $\hat{\Gamma}$ is a complex reflection coefficient, a time factor of $\exp(+j\omega t)$ is suppressed throughout. The fields undergo either a total or partial reflection depending on the angle of incidence and the index of refraction n of the dielectric substrate. Inspection of Eqs. (2.1) through (2.4) indicates that the solution of the boundary value problem has the following variation:

$$\exp[-jk_o\alpha x] \quad .$$

From this variation, the farzone field form in the y-z plane (Fig. 2.1) can be written as

$$f(\theta)\exp[-jk_o\sqrt{1 - \alpha^2}\,\rho] \quad . \qquad (2.5)$$

Equation (2.5), of course, applies to the air region. In (2.5), θ is the angle between the ground plane and a line drawn from the parallel plate opening to a farzone field point at a distance ρ away from the edge.

From Eq. (2.8), it is observed that, for $\alpha < 1$, the scattered fields propagate radially away from the discontinuity, thereby transferring power into the region external to the parallel plates in the form of sky wave radiation. If $\alpha > 1$, these fields become evanescent, and power associated with the incident field is not removed by radiation.

Sky wave radiation, however, is not the only mechanism for transferring power. The portion of the dielectric slab that is not covered by the conducting is capable of supporting LSE or LSM (with respect to the z axis) surface waves that can propagate along the y-axis away from the parallel plate opening. Assuming that y-axis propagation occurs for $\alpha < \alpha_p$, the surface waves in the air region behave as

$$\exp[-jk_o\alpha x]\exp[-jk_o\sqrt{\alpha_p^2 - \alpha^2}\, y]\exp[-k_o\sqrt{\alpha_p^2 - 1}\, z] \quad . \tag{2.6}$$

The value(s) of α_p are determined from the following transcendental equations:

$$\varepsilon_r\sqrt{\alpha_p^2 - 1} = \sqrt{n^2 - \alpha_p^2}\, \tan[\sqrt{n^2 - \alpha_p^2}\, k_o d] \quad \text{(LSE modes)} \tag{2.7}$$

$$\sqrt{\alpha_p^2 - 1} = \sqrt{n^2 - \alpha_p^2}\, \cot[\sqrt{n^2 - \alpha_p^2}\, k_o d] \quad \text{(LSM modes)} \; . \tag{2.8}$$

The solution of either Eq. (2.7) or (2.8) at a given $k_o d$ yields a finite number of α_p values. Each α_p corresponds to an individual propagating surface wave. Inspection of Eqs. (2.7) and (2.8) reveals that the α_p values must always be greater than 1. From Eq. (2.6), a surface wave is evanescent in the y direction when $\alpha > \alpha_p$. For $\alpha < \alpha_p$, the surface wave propagates along the y axis away from the discontinuity, which means that some of the incident wave power is being used to excite surface waves. When either radiation of surface wave propagation occurs, the magnitude of $\hat{\Gamma}$ must be less than one. Otherwise, the reflection coefficient magnitude is

unity, and complete reflection occurs. Assuming $\alpha_{p,max}$ corresponds to the largest solution of either Eq. (2.7) or Eq. (2.8), the results of this discussion are summarized in Table 2.1.

Table 2.1

α Range	Sky Wave Radiation	Surface Wave Propagation	Reflection Coefficient Magnitude
$0 \leq \alpha \leq 1$	yes	yes	< 1
$1 < \alpha < \alpha_{p,max}$	no	yes	< 1
$\alpha_{p,max} < \alpha < n$	no	no	$= 1$ complete reflection

In order to solve the problem of Fig. 2.1 rigorously, D.C. Chang and E.F. Kuester [1] have employed the Wiener-Hopf technique. From their analysis, the reflection coefficient has been found to be

$$\hat{\Gamma} = e^{j\hat{\chi}} \tag{2.9}$$

where

$$\hat{\chi} = 2 \tan^{-1}\left(\frac{\alpha}{\sqrt{n^2 - \alpha^2}} \tanh \Delta\right) - f_e(-\sqrt{n^2 - \alpha^2}) \tag{2.10}$$

$$\Delta = \frac{\alpha}{\pi} \int_0^\infty \ell n \left[\frac{u_o n^2}{u_n}\left(\frac{u_n + u_o \tanh u_n k_o d}{n^2 u + u_n \tanh u_n k_o d}\right)\right] \frac{d\lambda}{\lambda^2 + \alpha^2} \tag{2.11}$$

$$f_e(-\sqrt{n^2 - \alpha^2}) = \tan^{-1}\left(\sqrt{\frac{n^2 - \alpha^2}{\alpha^2 - 1}}\right)$$

$$- \frac{2}{\pi}\sqrt{n^2 - \alpha^2}\int_0^\infty \ell n\left[\frac{(n^2 + 1)u_o^2 \tanh u_n k_o d}{u_n(n^2 u_o + u_n \tanh u_n k_o d}\right]\frac{d\lambda}{\lambda^2 - \sqrt{n^2 - \alpha^2}} \tag{2.12}$$

$$u_n = \sqrt{\lambda^2 + \alpha^2 - n^2} \quad ; \quad u_o = \sqrt{\lambda^2 + \alpha^2 - 1} \quad . \tag{2.13}$$

In order to gain insight into the Wiener-Hopf solution for $\hat{\Gamma}$, the integrals of Eqs. (2.11) and (2.12) are intestigated. These integrals are written as

$$\Delta_1 = \int_0^\infty \ell n\left[\frac{u_o n^2}{u_n}\left(\frac{u_n + u_o \tanh u_n k_o d}{n^2 u_o + u_n \tanh u_n k_o d}\right)\right]\frac{d\lambda}{\lambda^2 + \alpha^2} \tag{2.14}$$

$$\upsilon = \int_0^\infty \ell n\left[\frac{(n^2 + 1)u_o^2 \tanh u_n k_o d}{u_n(n^2 u_o + u_n \tanh u_n k_o d}\right]\frac{d}{\lambda^2 - \sqrt{n^2 - \alpha^2}} \tag{2.15}$$

The integral (2.15) is a Cauchy principal value about the pole at $\lambda = \sqrt{n^2 - \alpha^2}$. The integrands of Eqs. (2.14) and (2.15) contain logarithmic singularities which may occur along the path of integration, depending on the value of α.

In order to provide a display of the singularities that gives more physical insight into the problem, Eqs. (2.14) and (2.15) can be integrated by parts. This, of course, does not change the value of the integrals or the singularity locations. The

singularity types do change, however, the resulting integrals contain poles in the λ plane which can be determined from the following transcendental equations:

$$\sqrt{\lambda_m^2 + \alpha^2 - 1} + \sqrt{\lambda_m^2 + \alpha^2 - 1}\ \text{cotanh}\left(\sqrt{\lambda_m^2 + \alpha^2 - n^2}\ k_o d\right) = 0 \tag{2.16}$$

$$n^2\sqrt{\lambda_e^2 + \alpha^2 - 1} + \sqrt{\lambda_e^2 + \alpha^2 - n^2}\ \tanh\left(\sqrt{\lambda_e^2 + \alpha^2 - n^2}\ k_o d\right) = 0 \tag{2.17}$$

Branch points, associated with u_o, are located at

$$\lambda = \pm j\sqrt{\alpha^2 - 1} \quad .$$

The phase on each side of the square root branch cut must be selected such that $\text{Re}\ u_o > 0$ along the path of integration in accordance with the radiation condition. Making the substitutions,

$$\lambda_e^2 + \alpha^2 = \alpha_p^2$$

$$\lambda_m^2 + \alpha^2 = \alpha_p^2 \tag{2.18}$$

in Eqs. (2.16) and (2.17) results in the LSE and LSM mode equations, (2.7) and (2.8). At this point, as a matter of convenience, the dielectric slab thickness d is assumed to be small enough to allow only the LSE_1 surface wave mode (with the smallest α_p value) to propagate. In terms of Eqs. (2.7) and (2.16), the quantities

α_{pel} and λ_{el} are the quantities associated with the LSE_1 mode.

Inspection of Eqs. (2.17) and (2.18) indicates that the integrand singularity locations are a function of α and, therefore, the angle of incidence ϕ. In fact, there are three different cases relating to the singularity positions in the λ plane. For $\alpha_{pel} < \alpha < n$, the branch cuts at $\lambda = \pm j\sqrt{\alpha^2 - 1}$ and the poles at $\lambda = \pm j\sqrt{\alpha^2 - \alpha_{pel}^2}$ lie along the imaginary axis of the λ plane. In this situation, which is illustrated in Fig. 2.2a, the values of the integrals in Eqs. (2.11) and (2.12) are real, resulting in a $\hat{\chi}$ that is real and a totally reflected incident TEM wave. When $1 < \alpha < \alpha_{pel}$, the singularities are located at $\lambda_e = \pm j\sqrt{\alpha^2 - 1}$ and $\lambda_{el} = \pm\sqrt{\alpha_{pel}^2 - \alpha^2}$ as is depicted in Fig. 2.2b. Since λ_{el} is now located on the real axis, the integrals in Eqs. (2.11) and (2.12) have a complex value. Thus, $\hat{\Gamma}$ is now complex, and some of the incident power is being used to excite an LSE_1 surface wave. In the range $0 \leq \alpha < 1$, the integration path includes both the surface wave pole and the branch cut contribution, resulting in a complex $\hat{\Gamma}$. Clearly for this situation, which is illustrated in Fig. 2.2c, power is being transferred into the region external to the parallel plates in the form of both surface waves and sky wave radiation. Thus, even more power is being transferred from the incident wave in this α range. One then would expect the magnitude of $\hat{\Gamma}$ to decrease monotonically with α in the range $\alpha < \alpha_{pel}$ until the reflection coefficient magnitude is a minimum at $\alpha = 0$.

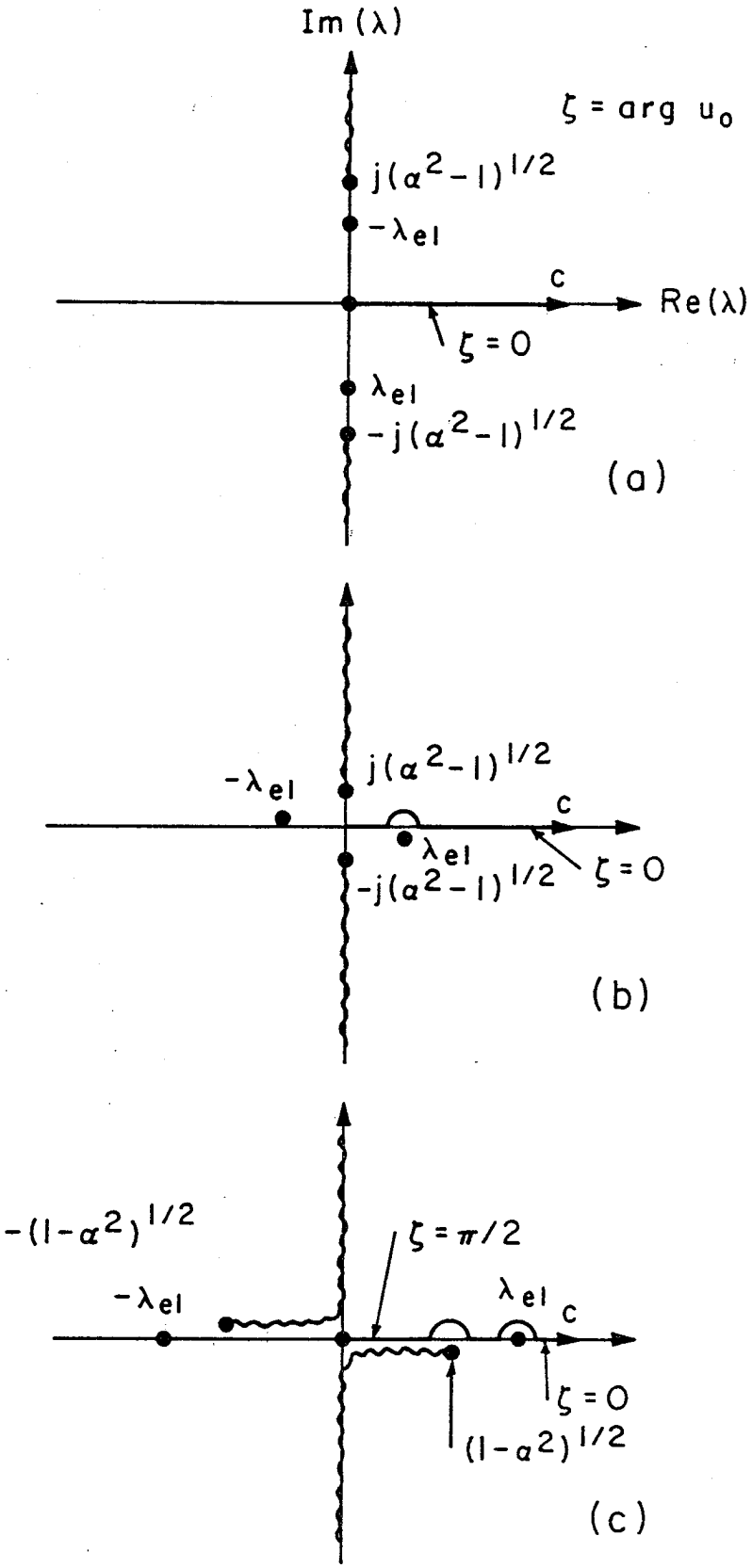
Im (λ)
ζ = arg u₀
j(α²−1)^1/2
−λel
c
Re(λ)
ζ = 0
λel
−j(α²−1)^1/2
(a)
−λel
j(α²−1)^1/2
c
λel
ζ = 0
−j(α²−1)^1/2
(b)
−(1−α²)^1/2
ζ = π/2
−λel
λel
c
ζ = 0
(1−α²)^1/2
(c)

Fig. 2.2.

2.3. The Numerical Evaluation of the Wiener-Hopf Reflection Coefficient

The integrals of Eqs. (2.11) and (2.12) cannot be evaluated analytically unless approximations are made. In order to obtain an exact value for these integrals, numerical integration is necessary. The Fortran IV program in Appendix B evaluates the integrals, and it also computes $\hat{\chi}$ and $\hat{\Gamma}$. The program contains a subroutine that is designed to integrate a complex function along the real axis. As has already been discussed, singularities may be located on the positive real axis of the λ plane. Before an integration is performed, the program predetermines the location of the singularities on the positive real axis. The program performs the integration up to a point that is close to a singularity, and then the integration resumes at a point immediately on the other side of the singular point. Assume now that a singularity is located on the positive real axis at $\lambda = x_o$. If x_o is a logarithmic singularity, the program stops the integration at $\lambda = 0.99999\ x_o$ and resumes it at $\lambda = 1.0001\ x_o$. In the case of the pole singularity at $x_o = \sqrt{n^2 - \alpha^2}$, the points are $0.99\ x_o$ and $1.01\ x_o$, respectively. The slowly varying nature of the logarithmic function allows the logarithmic singularities to be more closely approached.

In order to present some results generated by the program of Appendix B, the Wiener-Hopf reflection coefficient is written in magnitude and phase form as

$$\lambda = |\lambda|\ e^{+j\chi}$$

where $|\Gamma|$ and χ are real. In Figure 2.3, the normalized transmitted power, as a function of the electrical slab thickness $k_o d$, is plotted where $\varepsilon_r = 2.49$ and $\lambda = 0$ (normal incidence). From the curve, it is seen that the transmitted power increases linearly for small values of $k_o d$. A departure from the linear behavior is noted for larger $k_o d$. As a check of the program, the results of Fig. 2.3 were compared with curves presented in a paper by Bates and Mittra [7]. Although they compute the transmitted surface wave and sky wave power separately, adding the two components together at a given $k_o d$ results in an excellent comparison with the values of Fig. 2.3. In Fig. 2.4a, the transmitted power is plotted as a function of α at a fixed $k_o d$. The transmitted power is maximum at normal incidence, and it decreases with an increasing angle of incidence until no more power is transmitted for $\alpha > 1.02$. The value $\alpha = 1.02$ is α_{pel}, which corresponds to the LSE_1 mode wave number as determined from Eq. (2.17). Beyond $\alpha = 1.02$, complete reflection is observed, and $|\Gamma|$ is unity. The phase χ of the reflection coefficient is plotted if Fig. 2.4b. It varies from a small, negative value at $\alpha = 0$, to $+\pi$ as α approaches n. The phase curve crosses the α axis at $\alpha \simeq 2.16$. It is interesting to note that the phase does not change rapidly until α gets fairly close to n, which corresponds to nearly grazing incidence. The curve of Fig. 2.3b is quite flat near $\alpha = 0$, so the phase is essentially constant when the angle of incidence is close to being normal.

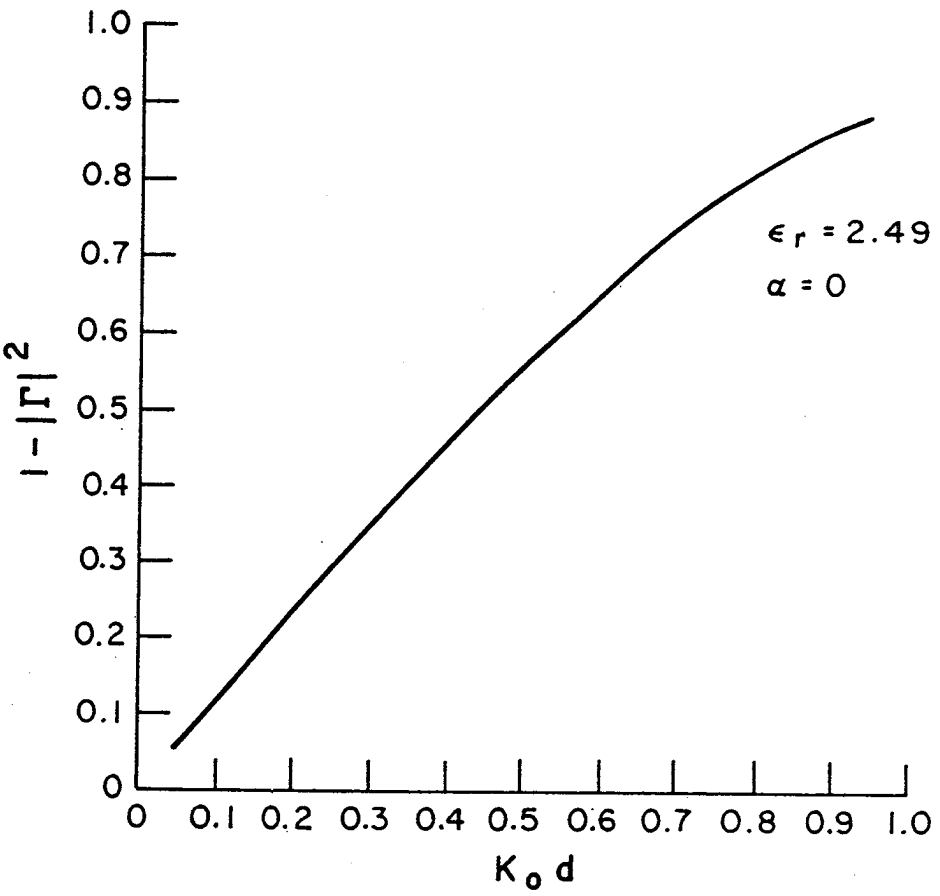
1.0
0.9
0.8
0.7
0.6
0.5
0.4
0.3
0.2
0.1
0
$1-|\Gamma|^2$
$\epsilon_r = 2.49$
$\alpha = 0$
0 0.1 0.2 0.3 0.4 0.5 0.6 0.7 0.8 0.9 1.0
$K_o d$

Fig. 2.3.

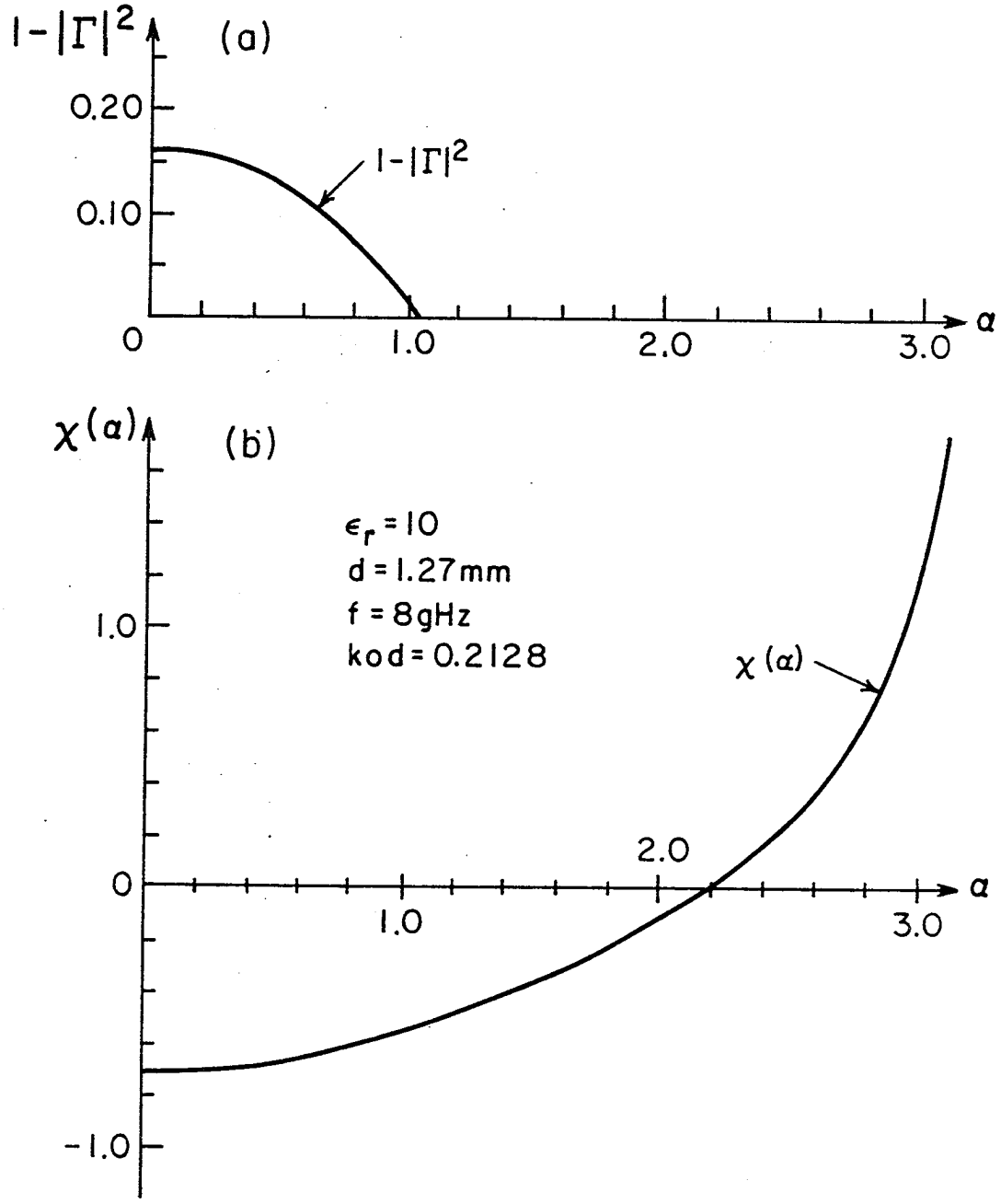
$1-|\Gamma|^2$
(a)
0.20
0.10
$1-|\Gamma|^2$
0
1.0
2.0
3.0
α
$\chi(\alpha)$
(b)
$\epsilon_r = 10$
d = 1.27mm
f = 8gHz
kod = 0.2128
1.0
$\chi(\alpha)$
2.0
0
1.0
3.0
α
-1.0

Fig. 2.4.

2.4. Approximate Analytical Formulas for The Wiener-Hopf Reflection Coefficient

So far, $\hat{\Gamma}$ has been evaluated by means of a computer program, which is cumbersome, time consuming, and expensive to use. The numerical approach also has the disadvantage of not yielding as much physical insight into the problem as can be gained from an analytical solution. D.C. Chang [8] has produced some analytical expressions for $\hat{\Gamma}$ under the assumption of a thin dielectric slab. The derivation of the analytical results is given in Appendix A, and the final results are given here. In the case of normal incidence ($\alpha = \phi = 0$) with $(nk_o d)^2 << 1$,

$$\hat{\Gamma} = |\Gamma| e^{+jX} \tag{2.19}$$

where

$$|\Gamma| = \exp(-k_o d/n) \quad ,$$

$$x = \frac{2}{\pi} nk_o d \left[\frac{1}{n^2} (\ell n\, k_o d + \gamma - 1) - \ell n\, 2\pi + 2Q_o \right] \quad ,$$

$$Q_o = \sum_{m=1}^{\infty} (-\delta_e)^m \ell n\, m \quad ,$$

$$\delta_e = \frac{n^2 - 1}{n^2 + 1}$$

and

$$\gamma = 0.57721 \ldots \quad \text{(Euler's constant)} \quad .$$

For the more general case in which $0 < \alpha < n$ (α not too close to 1

or n) and $(nk_o d) \ll 1$, the following reflection coefficient has been derived:

$$\hat{\Gamma} = e^{j\hat{\chi}} \tag{2.20}$$

where

$$\hat{\chi} = 2 \tan^{-1}\left(\frac{k_o d}{\pi}\frac{\alpha^2}{\sqrt{n^2-\alpha^2}}\left[\left(1-\frac{1}{n^2}\right)\left(1-\gamma-\ell n(k_o d\sqrt{\alpha^2-1})\right)+2Q_o\right]\right)$$

$$+\frac{2k_o d}{\pi}\sqrt{n^2-\alpha^2}\left[-\ell n\, 2\pi+\frac{1}{n^2}\left(\ell n(k_o d\sqrt{\alpha^2-1})+\gamma-1\right)+2Q_o\right] .$$

As is stated in Appendix A, when $\alpha < 1$, the proper choice of branch for $\sqrt{\alpha^2 - 1}$ is $+j\sqrt{1 - \alpha^2}$. As a check, Chang's results agree completely with those derived by Kuester, Johnk, and Chang [5] who employ a totally different approach. It is also of interest to note that for $n = 1$ (air substrate), Eq. (2.19) reduces to a result given in Lewin [15] and Weinstein [16].

In Figs. 2.5 and 2.6, a comparison of $\hat{\Gamma}$ values predicted by the approximate formulas with those generated by the computer is provided for $\varepsilon_r = 2.56$. It should be noted that the computer program provides values which in principle are exact. Thus, the program of Appendix B provides a basis for the verification of the approximate formulas. Fig. 2.5 deals with a sitaution in which $\alpha = 0$ and $k_o d$ varies. It is seen that for small $k_o d$, there is an excellent agreement between the approximate values of Eq. (2.19) and the numerical results. For larger $k_o d$, however, differences in the magnitude and phase, as predicted by the two approaches, become greater. There are two reasons for this. First, the

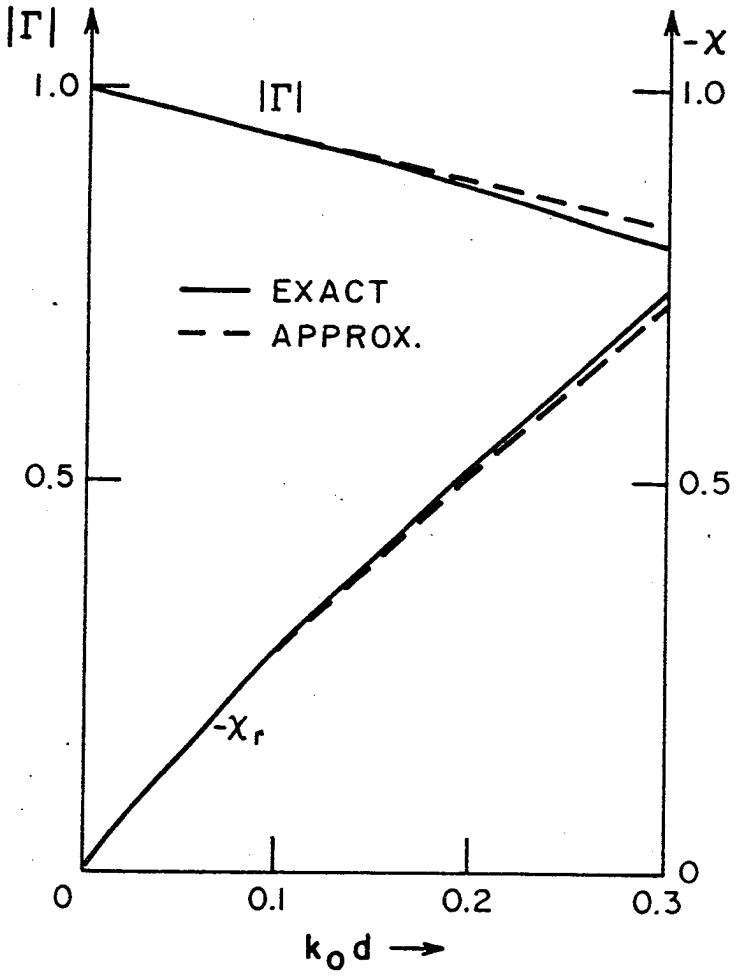

Fig. 2.5.

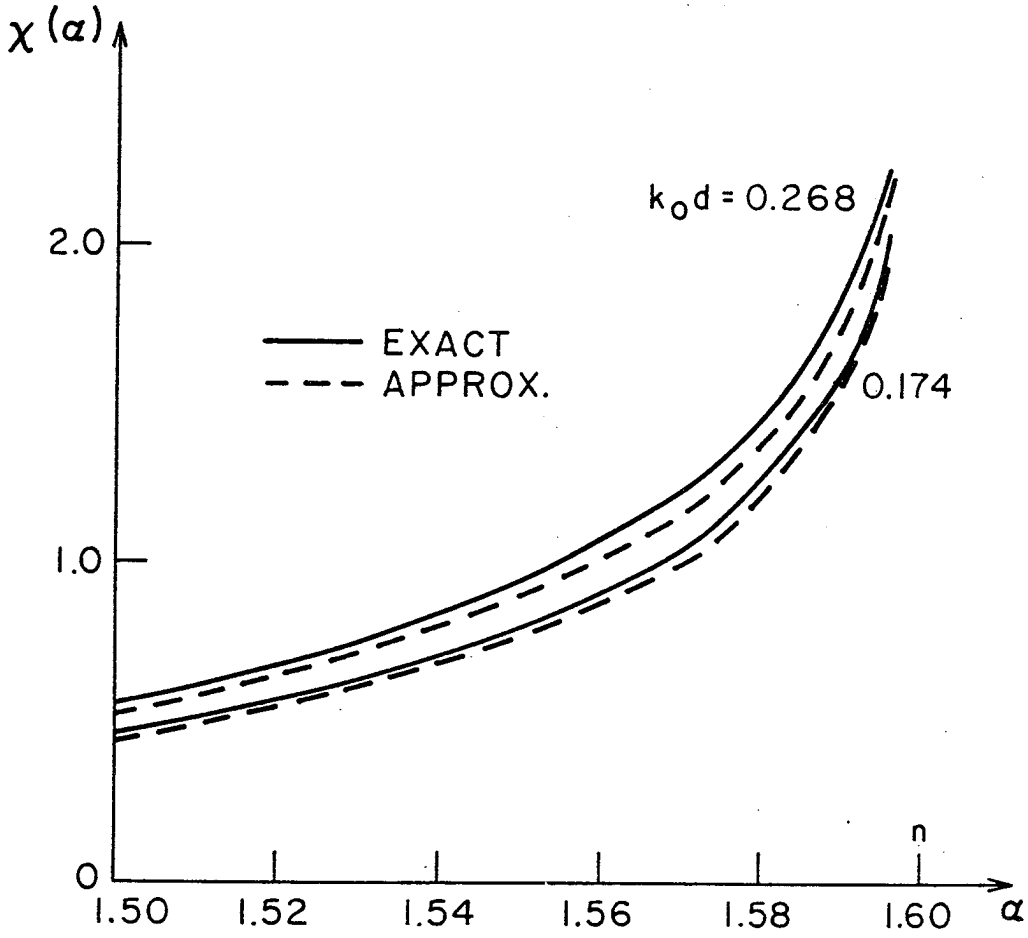

Fig. 2.6.

approximate formulas are valid when $(nk_o d)^2 << 1$. As $k_o d$ becomes larger, this condition is violated, and the accuracy of approximation deteriorates. Second, the approximate formulas do not account for the effects of surface waves (evanescent or propagating) that exist in the dielectric slab region external to the conducting patch. In the normal incidence case, the estimate of the integral of Eq. (2.12) is found to be $O\left(\frac{(k_o d)^2}{2n^3}\right)$ (see Appendix A). Thus, for small $k_o d$, the surface wave effects can be neglected. But as $k_o d$ increases, the surface wave contribution becomes more significant, and it must be accounted for. Fig. 2.6 illustrates a case of near grazing incidence in which χ is plotted as a function of α for $\varepsilon_r = 2.56$, $k_o d = 0.174$ and $k_o d = 0.268$. The agreement between the approximate phase values of Eq. (2.20) and the numerically exact phase is quite good. As in the normal incidence case, the agreement is not as good for larger $k_o d$.

2.5. The Transverse Resonance Condition and The Graphical Solution

Fig. 2.7 shows a section of an infinitely long microstrip transmission line. This configuration is similar to that of Fig. 2.1, except that the top conductor has the finite width 2ℓ. It is also assumed that the dielectric slab is thin enough to allow only an LSE_1 mode to propagate. If the slab relative permittivity is not equal to one, this structure cannot support a mode that is TEM with respect to the x-axis. However, a propagating mode can be represented as a TEM wave underneath the top conductor, bouncing

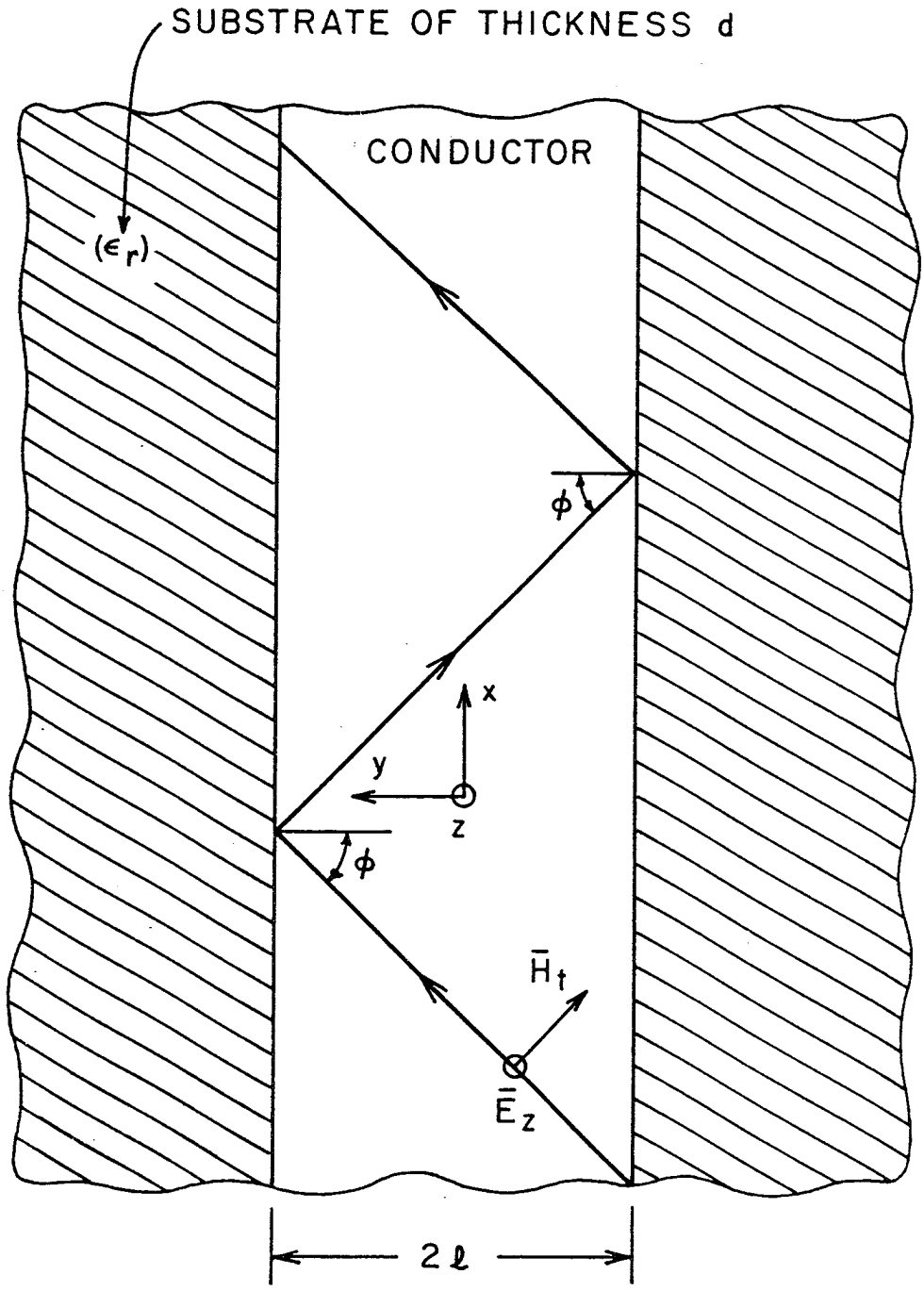
SUBSTRATE OF THICKNESS d
CONDUCTOR
(ϵ_r)
ϕ
x
y
z
ϕ
$\bar{H}_t$
$\bar{E}_z$
2ℓ

Fig. 2.7.

back and forth between the conductor edges as shown in Fig. 2.7. The TEM wave is incident at an angle ϕ with respect to a line drawn normal to the edges of the top conductor. Assuming that the two edges of the top conductor are reasonably separated, the reflection coefficient of the TEM wave, due to the discontinuities of the top conductor edges, is the same as the Wiener-Hopf reflection coefficient of the canonical problem (Fig. 2.1). Thus, the reflection coefficient at each bounce is given by Eq. (2.9).

In order for the wave to propagate in the x direction, two requirements must be met. First, constructive interference must occur on successive reflections. This means the wave must undergo a phase shift that is a multiple of 2π in a complete bounce. The second requirement is on the angle of incidence of the TEM wave. The angle should be such that neither radiation nor surface wave propagation occurs. Otherwise, energy is lost at each reflection, resulting in decay. More precisely, the requirements for propagation are

$$2k_o \ell = \frac{\chi + m\pi}{\sqrt{n^2 - \alpha^2}} \quad , \qquad m = 0, 1, 2, \ldots \tag{2.21}$$

$$\alpha > \alpha_{pel} \quad . \tag{2.22}$$

Eq. (2.21) determines the α value at which constructive interference occurs, and (2.22) defines the range of α for which neither surface wave propagation nor radiation occurs. α_{pel} is the solution of Eq. (2.7) for the lowest order LSE_1 surface wave

that propagates in the dielectric slab.

A graphical representation of Eq. (2.21) is provided in Fig. 2.8 where $f = 8$ GHz, $d = 3.2$ mm, and $\varepsilon_r = 10$. Alpha values in the range $0 \leq \alpha < n$, corresponding to $0 \leq \phi < \pi/2$, are located on the horizontal axis. The vertical axis contains values for the electrical conductor width $2k_o\ell$. The family of curves represents the function $\frac{\chi + m\pi}{\sqrt{n^2 - \alpha^2}}$, plotted as a function of α for $m = 0$, 1, and 2. These curves have been generated by means of the computer program of Appendix B. Lines drawn normal to the coordinate axis and intersecting on an mth curve in the unshaded region correspond to the $2k_o\ell$ and α values for which the mth mode propagates down the line. Constructive interference occurs in the shaded region, where $\alpha < \alpha_{pel}$, but decay occurs due to radiation and surface wave effects. A mode that satisfies Eq. (2.27) but <u>not</u> Eq. (2.28) is referred to as a leaky mode. The leaky mode solutions, therefore, lie in the shaded region of Fig. 2.8. It is observed in Fig. 2.8 that only the fundamental ($m = 0$) mode can propagate down the microstrip structure when

$$2k_o\ell < \frac{\pi + \chi}{\sqrt{n^2 - \alpha^2}} \quad .$$

As an example, a line drawn from $2k_o\ell = 0.6$ at ① (see Fig. 2.8) to the point of intersection with the $m = o$ curve at ② yields an $\alpha \simeq 2.85$ at ③. Thus, for $2k_o\ell = 0.6$, the fundamental mode is the only mode available for propagation, and it propagates at the angle of incidence of $\phi = \sin^{-1}(2.85/\sqrt{10}) \simeq 65°$. Equations (2.21)

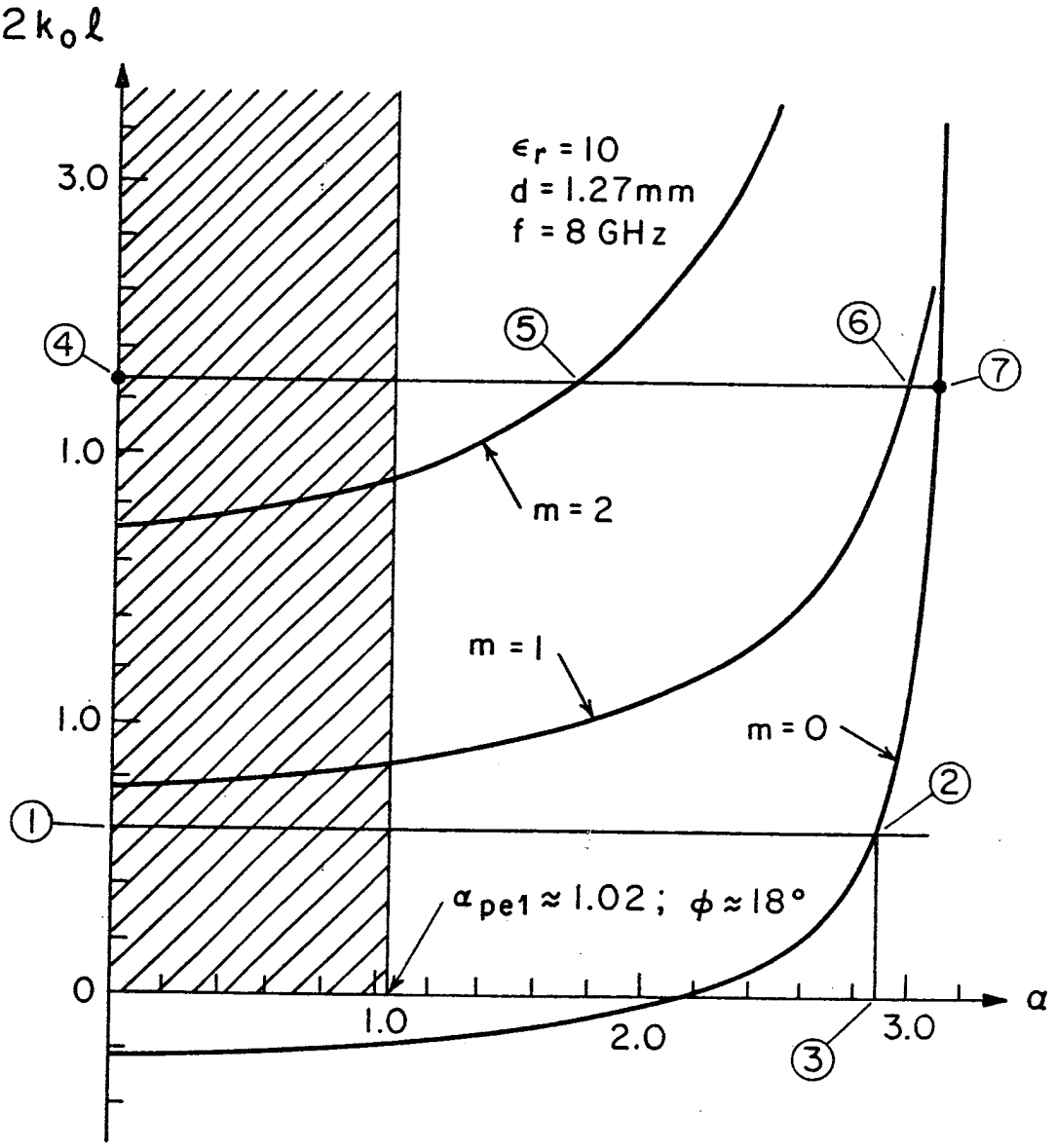
2k₀ℓ
3.0
1.0
1.0
0
1.0
2.0
3.0
α
εr = 10
d = 1.27mm
f = 8 GHz
m = 2
m = 1
m = 0
αpe1 ≈ 1.02 ; φ ≈ 18°
1
2
3
4
5
6
7

Fig. 2.8.

and (2.22), then, provide a basis for designing a microstrip line supporting only one mode. As $2k_o\ell$ increases, a line projected normal to the vertical axis intersects curves corresponding to modes other than the fundamental. This point is illustrated in Fig. 2.8, where a line is drawn from the $2k_o\ell = 2.25$ point at ④ to ⑦ on the $m = 0$ curve. The line also intersects the $m = 2$ and $m = 1$ curves at points ⑤ and ⑥, respectively, which means that it is possible for three modes to propagate. Thus, as the strip is made wider, higher modes are available to propagate in addition to the fundamental. Fig. 2.8 indicates that the fundamental mode propagates with an α value close to n, corresponding to nearly grazing incidence. The higher modes, on the other hand, begin to propagate when $\alpha > \alpha_{pel}$. In terms of Fig. 2.8, the higher modes begin to propagate with $\phi \simeq 18°$, which is not too far from normal incidence.

2.6. A Comparison of the Transverse Resonance Formulation with Two Other Approaches

For the case of the fundamental mode, Fig. 2.9 shows a comparison of the α^2 values generated from the transverse resonance condition (Eq. 2.21) with those of Kuester and Chang [1] and Nefedov and Fialkovski [6]. The α^2 values, produced by Eq. (2.21), have been solved for numerically by means of the program of Appendix B. The effective dielectric constant (α^2) is plotted as a function of frequency with $\ell/d = 2$, $\ell/d = 4$, $\varepsilon_r = 10$, and $d = 1.27$ mm. For $nk_o\ell \gtrsim 0.5$, the present approach (Eq. 2.21)

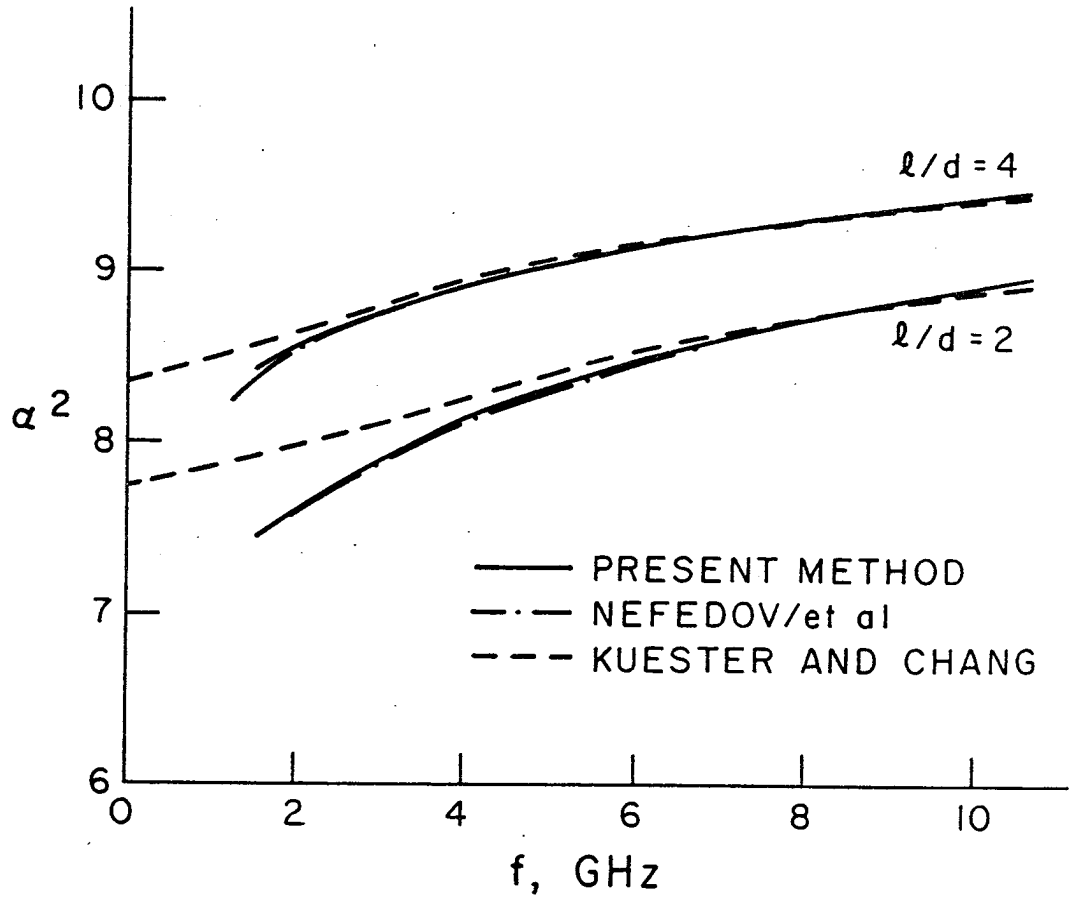
10
9
8
7
6
α 2
ℓ/d = 4
ℓ/d = 2
PRESENT METHOD
NEFEDOV/et al
KUESTER AND CHANG
0
2
4
6
8
10
f, GHz

Fig. 2.9.

closely agrees with the variational method of Kuester and Chang. Since Nefedov uses an approach which is either similar to or identical to the transverse resonance formulation, the curves produced by the two methods are virtually identical for all parameter values. As the frequency decreases, the electrical width of the top conductor also decreases, resulting in an increased coupling between the top conductor edges. Because of this coupling effect, the present method, along with that of Nefedov, break down at lower frequencies. Since the variational approach of Kuester and Chang is known to give good results for electrically narrow strips, the breakdown in the present method is seen to occur at $nk_o d \simeq 0.5$ in Fig. 2.9. For electrically wide strips, however, Eq. (2.21) should yield accurate results.

2.7. Approximate Expressions for α of the Fundamental Propagating Mode

At this point, it is convenient to present approximate formulas for the propagation constant α of the fundamental mode. From Eq. (2.21) with $m = 0$,

$$2k_o \ell \sqrt{n^2 - \alpha^2} = \chi \ . \tag{2.23}$$

Under typical operating conditions, the fundamental mode has an α that is fairly close to n. However, α usually has a value such that the ratio $\frac{k_o d\alpha}{\sqrt{n^2 - \alpha^2}}$ is still small, assuming, of course, that $(nk_o d) \ll 1$. This fact allows the arctangent term in Eq.

(2.20) to be replaced by its small argument expansion, which results in the following equation:

$$\chi \simeq \frac{2k_o d}{\pi}\left\{\frac{n^2}{\sqrt{n^2-\alpha^2}}\left[\left(1-\frac{1}{n^2}\right)\left(1-\gamma-\ln(k_o d\sqrt{\alpha^2-1})\right)+2Q_o\right]\right.$$

$$\left.-\sqrt{n^2-\alpha^2}\left[\ln\left(\frac{2\pi}{k_o d\sqrt{\alpha^2-1}}\right)+1-\gamma\right]\right\}. \qquad (2.24)$$

Applying (2.24) to (2.23) yields the following approximate expression for α:

$$\alpha \simeq n\left[\frac{1+\frac{d}{\pi\ell}\left[\frac{1}{n^2}\left(\ln\left(\frac{1}{k_o d\sqrt{n^2-1}}\right)+1-\gamma\right)+\ln 2\pi-2Q_o\right]}{1+\frac{d}{\pi\ell}\left[\ln\left(\frac{2\pi}{k_o d\sqrt{n^2-1}}\right)+\gamma-1\right]}\right]^{1/2} \qquad (2.25)$$

Since $\frac{d}{\pi\ell} << 1$ in the wide strip case, (2.25) can be further simplified to

$$\alpha \simeq n\left\{1-\frac{d}{2\pi\ell}\left[\left(1-\frac{1}{n^2}\right)\left(\ln\left(\frac{1}{k_o d\sqrt{n^2-1}}\right)+1-\gamma\right)\right]+2Q_o\right\}. \qquad (2.26)$$

Equations (2.25) and (2.26) reveal the functional dependence of the fundamental mode propagation constant on the slab thickness d, the aspect ratio ℓ/d, and the substrate dielectric constant ε_r. It is clear from these equations that as ℓ/d increases, the angle of incidence ϕ becomes more grazing. This is consistent with the discussion of the graphical approach. A comparison of Eqs. (2.25)

and (2.26) with numerical and experimental results is provided in Chapter V.

2.8. Electric Field and Surface Current Variations On an Infinitely Long Microstrip Line

The z-directed E field associated with a propagating mode can be written as [2]

$$E_{zm} = A_m \cos\left(\sqrt{n^2 - \alpha_m^2}\, y\right) e^{-jk_o \alpha_m x} \quad (m = 0, 2, 4, \ldots) \tag{2.27}$$

$$E_{zm} = A_m \sin\left(\sqrt{n^2 - \alpha_m^2}\, y\right) e^{-jk_o \alpha_m x} \quad (m = 1, 3, 5, \ldots) \tag{2.28}$$

In these equations, α_m is the solution of Eq. (2.27) for the mth mode, and A_m is the modal amplitude which depends on the microstrip line parameters as well as the method by which the line is excited. Eqs. (2.27) and (2.28) are valid in the region underneath the top conductor, away from the conductor edges. For m odd, the resulting E-field, due to the mth mode, is antisymmetrical with respect to the center of the top conductor. When m is even, a symmetrical field distribution occurs. Applying Eqs. (2.27) and (2.28) to Maxwell's curl relation and invoking the boundary condition, $\bar{J}_s = \bar{n} \times \bar{H}$, yields the following transverse ground plane and top conductor surface current proportionalities,

$$J_{sym} \propto \sin(\sqrt{n^2 - \alpha_m^2}\, y) \qquad m = 0, 2, 4, \ldots \tag{2.29}$$

$$J_{sym} \propto \cos(\sqrt{n^2 - \alpha_m^2}\, y) \qquad m = 1, 3, 5, \ldots \tag{2.30}$$

The range of y, for which these expressions are valid, is identical to that of Eqs. (2.27) and (2.28). Thus, with respect to the center of the top conductor, even modes have associated antisymmetrical transverse current distributions, and odd modes possess symmetrical field variations. The importance of the results of this section will become apparent in Chapter IV.

2.9. The Open-End Microstrip Line

Figs. 2.10 and 2.11a depict an open-end microstrip transmission line. The only difference between this configuration and the infinitely long line of Fig. 2.7 is the termination of the top conductor at $x = x_o$. It is also assumed that the line of Fig. 2.10 is electrically wide and supports only the fundamental ($m = 0$) mode. The incident mode is assumed to originate at $\chi = -\infty$ and has a propagation constant $k_o \alpha_o$, which can be determined from Eqs. (2.27). Once again, the fundamental mode is represented in Fig. 2.10 as a TEM wave bouncing back and forth at an angle ϕ with respect to a line normal to the top conductor edges. In terms of the geometry of Fig. 2.10, this wave strikes the edge at $x = x_o$ at an angle of incidence $\frac{\pi}{2} - \phi$, which, in terms of α_o, is $\sqrt{n^2 - \alpha_o^2}$. The open end discontinuity results in the partial reflection of the fundamental mode along with higher

order waveguide type modes that decay rapidly underneath the top conductor. As was the case in the canonical problem of Fig. 2.1, the open end also produces radiation and surface waves in the region external to the top conductor. In fact, with the assumption of an electrically wide top conductor, it appears that the reflection coefficient of Eq. (2.12) should accurately predict how much of the fundamental mode is reflected. Thus, at a sufficient distance from the open end, Eqs. (2.9) and (2.27) yield the following E-field underneath the top conductor (A_o is assumed to be 1):

$$E_{zo} = \cos(\sqrt{n^2-\alpha_o^2})e^{-jk_o\alpha_o(x-x_o)}\left[1+\hat{\Gamma}(\alpha=\sqrt{n^2-\alpha_o^2})e^{+j2k_o\alpha_o(x-x_o)}\right] \tag{2.31}$$

The open end, then, produces a standing wave field distribution underneath the top conductor. Utilizing conventional transmission line theory, a normalized end admittance is defined from the reflection coefficient of Eq. (2.31) as

$$\hat{y} = \frac{1 - \hat{\Gamma}(\alpha = \sqrt{n^2 - \alpha_o^2})}{1 + \hat{\Gamma}(\alpha = \sqrt{n^2 - \alpha_o^2})} \tag{2.32}$$

With $\hat{\Gamma}(\alpha = \sqrt{n^2 - \alpha_o^2}) = |\Gamma|e^{+j\chi}$, Eq. (2.32) is written as

$$\hat{y} = \frac{1 - |\Gamma|e^{+j\chi}}{1 + |\Gamma|e^{+j\chi}} = g + jb \quad . \tag{2.33}$$

The normalized admittance consists of a conductance term and a

capacitive susceptance. The conductance term accounts for the surface wave and radiation effects introduced by the open end, and the susceptance accounts for the reactive power stored in the fringe fields. It can be seen from Eq. (2.35) that the admittance depends on the line geometry, the frequency of operation, and the angle of incidence, $\pi/2 - \phi$, at the open end. Defining the end admittance in terms of the Wiener-Hopf reflection coefficient, therefore, results in a truly dynamic admittance. In general, the conductance and susceptance terms are nonlinear functions of frequency.

2.10. Approximate End Admittance Expressions

More knowledge about the nature of the end admittance can be gained by approximating the right side of Eq. (2.33). Assuming that the magnitude of the reflection coefficient of the open end is close to one, Eq. (2.33) yields the following expressions:

$$g \simeq \frac{1}{4}\,(1 - |\Gamma|^2)\sec^2\left(\frac{\chi}{2}\right)$$

$$b \simeq -\tan\left(\frac{\chi}{2}\right) \qquad (2.34)$$

If, in addition, $k_o d << 1$, Eq. (2.34) further simplifies to

$$g \simeq \frac{1 - |\Gamma|^2}{4}$$

$$b \simeq \frac{-\chi}{2} \qquad (2.35)$$

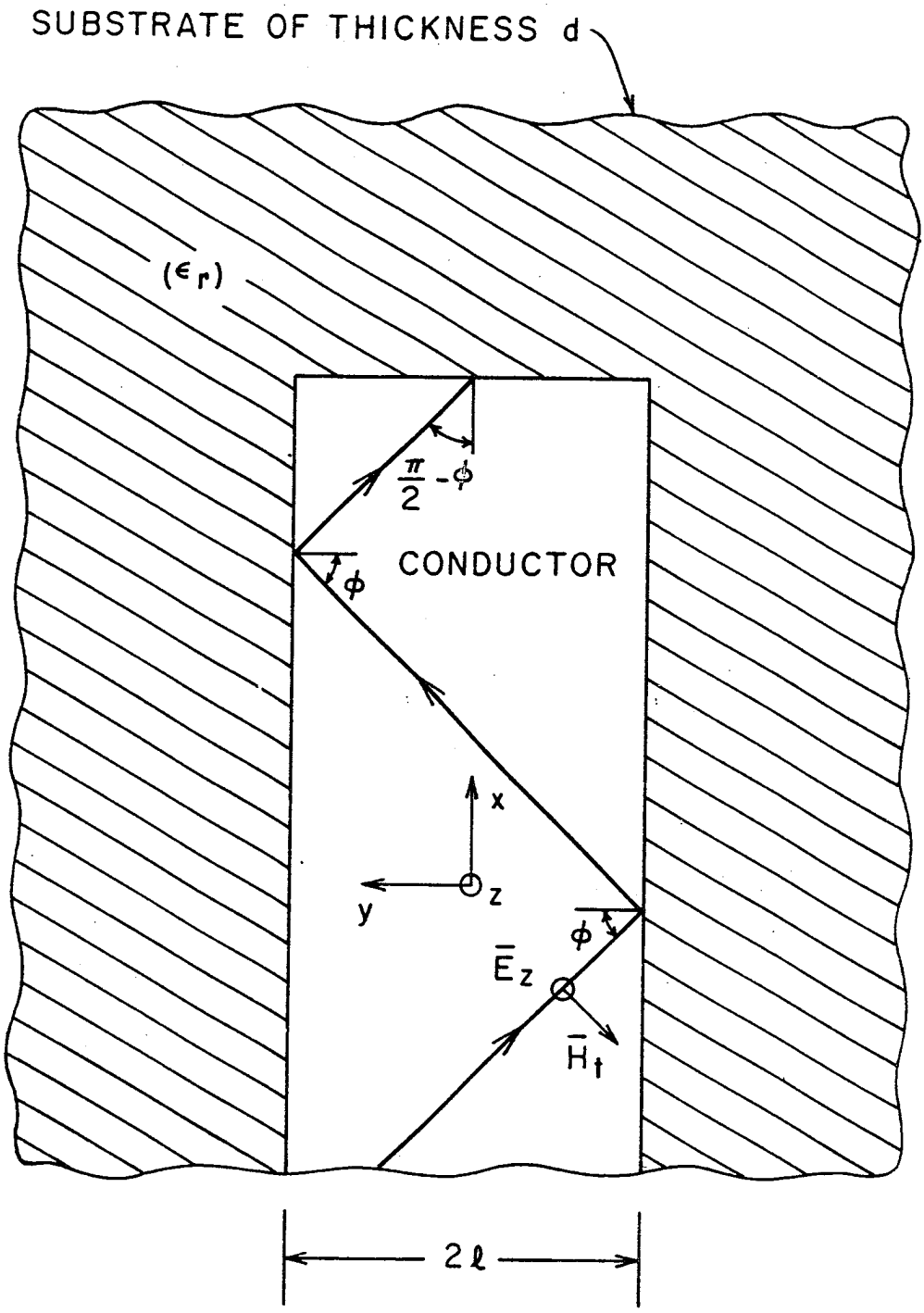
SUBSTRATE OF THICKNESS d
(ϵ_r)
$\frac{\pi}{2} - \phi$
CONDUCTOR
ϕ
x
z
y
ϕ
$\bar{E}_z$
$\bar{H}_t$
2ℓ

Fig. 2.10.

The approximations in Eq. (2.36) provide a decoupling of the reflection coefficient magnitude and phase in the admittance calculation. The significance of the decoupling will become apparent in Chapter V.

The approximate reflection coefficient relations can be applied to Eqs. (2.34) and (2.36) to yield analytical admittance expressions. Applying (2.24) to (2.34) (noting that $\sqrt{n^2 - \alpha_o^2} = \alpha$ and $0 \leq \alpha < 1$),

$$g \simeq \frac{1}{4}\left(1 - e^{\frac{-2k_o d(1-\alpha^2)}{n}}\right) \sec^2\left[\frac{k_o d}{\pi}\left\{\frac{n^2}{\sqrt{n^2-\alpha^2}}\left[\left(1 - \frac{1}{n^2}\right)\left(1 - \gamma - \ell n(k_o d\sqrt{1-\alpha^2})\right) + 2Q_o\right] - \sqrt{n^2-\alpha^2}\left[\ell n\left(\frac{2\pi}{k_o d\sqrt{1-\alpha^2}}\right) + 1 - \gamma\right]\right\}\right]$$

$$b \simeq \tan\left[\frac{k_o d}{\pi}\left\{\frac{n^2}{\sqrt{n^2-\alpha^2}}\left[\left(1 - \frac{1}{n^2}\right)\left(1 - \gamma - \ell n(k_o d\sqrt{1-\alpha^2})\right) + 2Q_o\right] - \sqrt{n^2-\alpha^2}\left[\ell n\left(\frac{2\pi}{k_o d\sqrt{1-\alpha^2}}\right) + 1 - \gamma\right]\right\}\right] \quad . \tag{2.36}$$

The expressions in Eq. (2.36) are complex functions of the microstrip line parameters, the value of α_o, and the frequency of operation of the line. The nonlinear nature of the end admittance is clearly evident. The end admittance, in fact, can be modeled as a dynamic resistance in parallel with a dynamic capacitance, as is shown in Fig. 2.11b. Assuming that $k_o d \ll 1$ and $\alpha = 0$, Eq. (2.36) can be simplified to

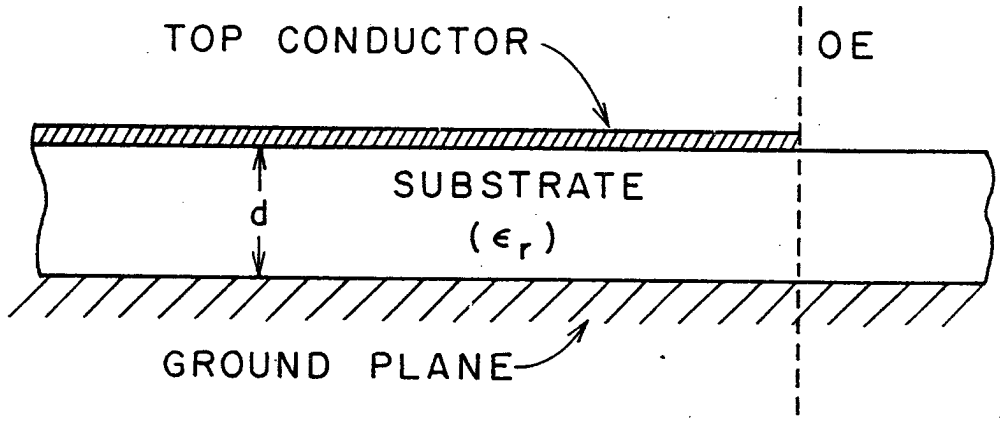
TOP CONDUCTOR
OE
SUBSTRATE
(ϵ_r)
d
GROUND PLANE

(a)

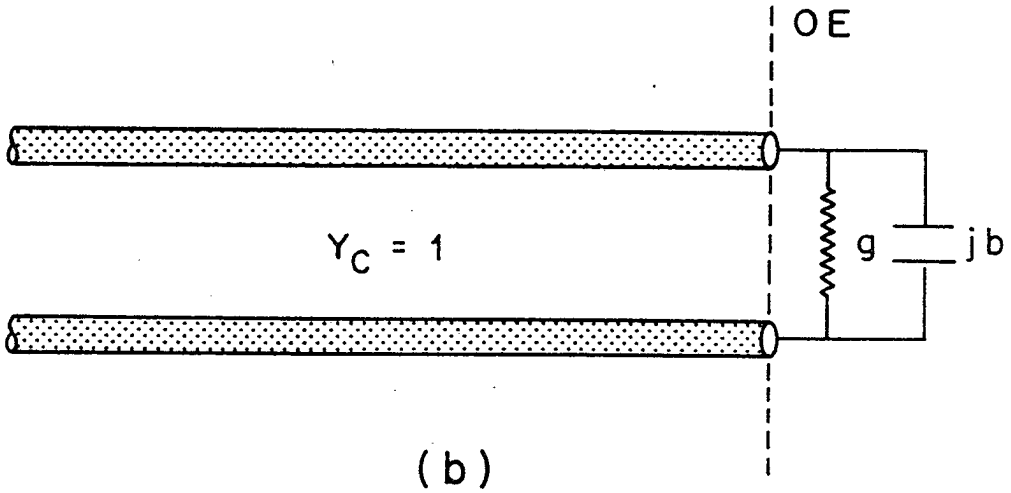
OE
Y_C = 1
g
jb

(b)

Fig. 2.11.

$$g \simeq \frac{k_o d}{2n}$$

$$b \simeq \frac{nk_o d}{\pi}\left[\frac{1}{n^2}(\ell n\, k_o d + \gamma - 1) - \ell n\, 2\pi + 2Q_o\right] . \tag{2.37}$$

In this case, the conductance varies linearly with $k_o d$, but the susceptance b is still nonlinear in $k_o d$.

2.11. The Concept of Equivalent Length

The open end results in an excess charge accumulation in the region around the discontinuity. This effect is accounted for by the capacitance of Fig. 2.11b. In order to develop an alternative representation of this effect, consider a transmission line that has a perfect open circuit, as is shown in Fig. 2.12a. A perfect open circuit has no charge accumulation associated with it, thus yielding no fringing fields in the region around it. Referring to Fig. 2.12b, the charge accumulation can be accounted for by defining the discontinuity to be at A and adding a section of transmission line of length Δh. The additional length of line contains the excess charge accumulation produced by the discontinuity. Thus, the additional length of line is equivalent to the capacitance and, therefore, the susceptance of Fig. 2.11b. Utilizing a result in Gupta [14], the equation relating b to Δh is given by

$$\frac{\Delta h}{d} = \frac{b}{nk_o d} . \tag{2.38}$$

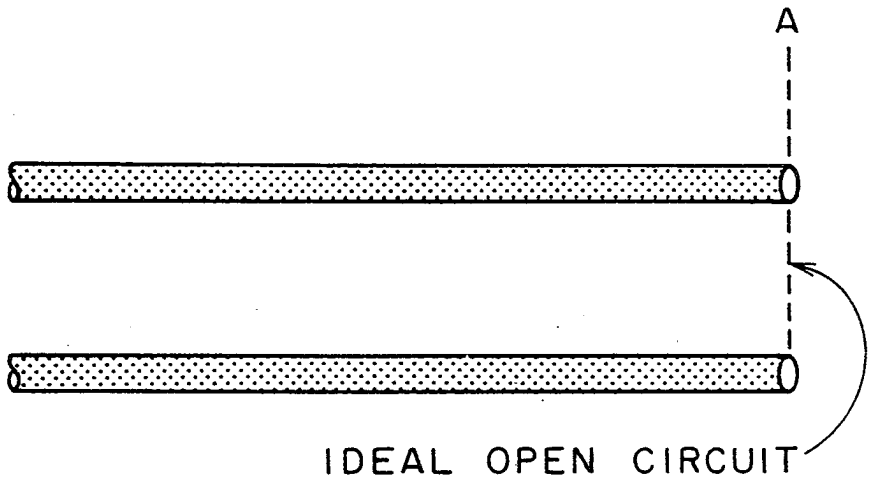
A
IDEAL OPEN CIRCUIT

(a)

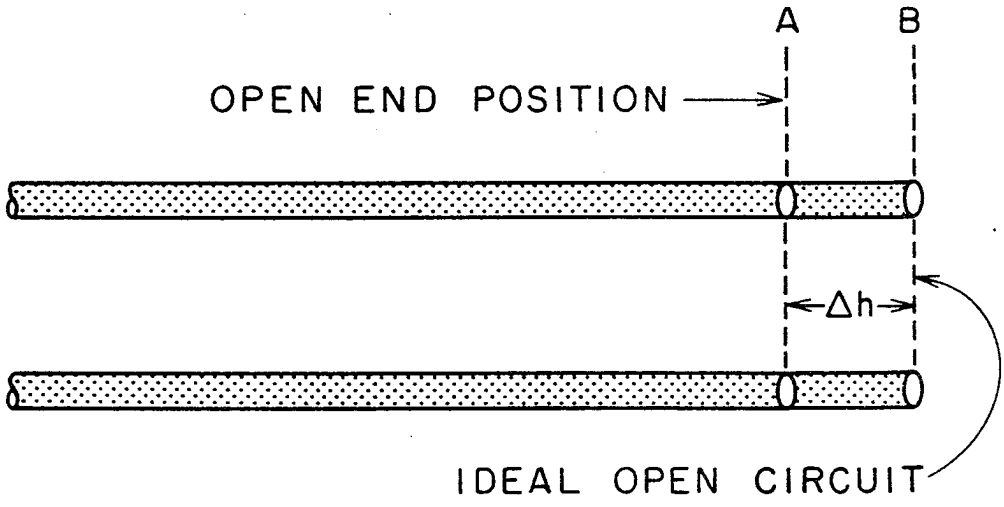
A
B
OPEN END POSITION
Δh
IDEAL OPEN CIRCUIT

(b)

Fig. 2.12.

If the susceptance varies linearly as a function of frequency, Eq. (2.38) indicates that $\Delta h/d$ must be constant. This is not surprising since a fixed equivalent length corresponds to a constant, nondynamic capacitance. The application of either (2.36) or (2.37) to (2.30) results in an equivalent length that varies with $k_o d$. The Wiener-Hopf solution, then, predicts the dynamic length extension Δh.

CHAPTER III

ADDITIONAL END ADMITTANCE FORMULATIONS

3.1. Introduction

In Chapter II, the Weiner-Hopf approach to the modeling of the open end admittance of an electrically wide microstrip transmission line, as developed by Chang and Kuester, was presented. This chapter, on the other hand, deals with several end admittance formulations by individuals other than Chang and Kuester. The second section of this chapter deals with the general features of a Wiener-Hopf solution as presented by Lewin [15]. Although his solution has not been applied directly to microstrip problems, it is of interest because it serves as a partial check of the Chapter II results, and it has been derived using the same mathematical approach as is employed in the solution of the canonical problem of Fig. 2.1. In order to gain insight into the significance of the Wiener-Hopf solution, it is necessary to provide a comparison with the more conventional technique of calculating the open end conductance and susceptance of a microstrip transmission line from two separate and unrelated approaches. Thus, the details of the conductance and susceptance calculations are presented in the last two sections of this chapter.

3.2. Lewin's Parallel-Plate Solution

The system of Fig. 3.1a consists of two perfectly conducting parallel plates of zero thickness separated by a distance $2d$. The plates are infinitely long in the y direction and are semi-infinite in extent along the negative z axis. The nonmagnetic medium, in which the two conductors are immersed, is assumed to be uniform with a relative permittivity ε_r. It is assumed that a pure TEM wave (with respect to the z-axis) is normally incident on the open end at $z = 0$. The dimension d is small enough so that only the TEM mode can propagate along the parallel-plate transmission line. From image theory, the problem of Fig. 3.1a is identical to that of Fig. 3.1b in which a semi-infinite conducting plate is located above a ground plane. In terms of the reflection coefficient of the TEM mode, the solutions corresponding to Figs. 3.1a and 3.1b are identical. Now, the effects of the open end in Fig. 3.1b are similar to those of Fig. 2.1, except that surface waves no longer occur on account of the uniform medium. In fact, with $\varepsilon_r = 1$, the problem of Fig. 3.1b is identical to that of Fig. 2.1 when $\alpha = 0$. Lewin [15] has solved the normally incident case of Fig. 3.1 using the Wiener-Hopf technique. Lewin's solution for the reflection coefficient of the TEM wave is given by ($\varepsilon_r = 1$)

$$\hat{\Gamma} = |\Gamma| e^{j\chi} \tag{3.1}$$

where

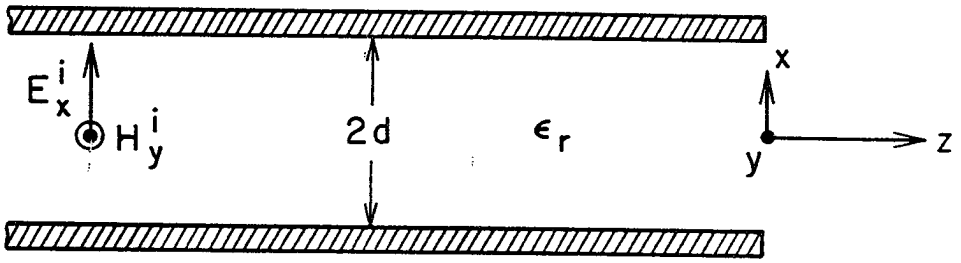

(a)

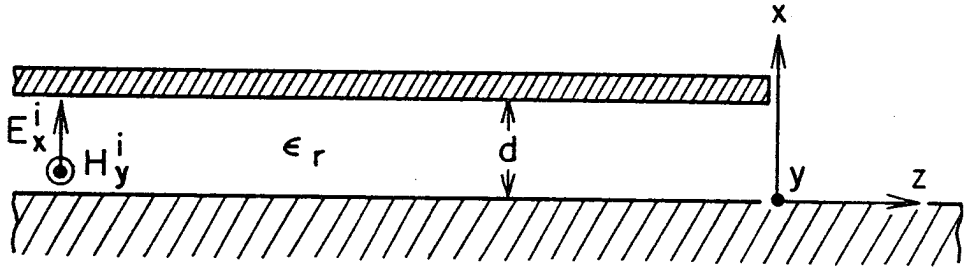

(b)

Fig. 3.1.

$$|\Gamma| = e^{-k_o d}$$

$$\chi = \frac{1}{\pi}\left\{2k_o d\ \ell n(2k_o d) - 2k_o d(\ell n\ 4\pi + 1 - \gamma) + 2\pi \sum_{m=1}^{\infty}\left[\sin^{-1}\left(\frac{k_o d}{m\pi}\right) - \frac{k_o d}{m\pi}\right]\right\}$$

When $k_o d << 1$, χ becomes

$$\frac{2k_o d}{\pi}\left\{\ell n\left(\frac{k_o d}{\pi}\right) + \gamma - 1\right\} \quad . \tag{3.2}$$

It can be seen that Lewin's solution corresponds to Eq. (2.19) with $\alpha = 0$ and $\varepsilon_r = 1$. This comes as no surprise since both problems have been solved by the same method. As is mentioned in Chapter II, Lewin's solution serves as a partial check of the oblique incidence case. Finally, it should be mentioned that Weinstein [16] has also solved the problem of Fig. 3.1 using the same approach with identical results.

3.3. A Slot Radiation Conductance Calculation

A radiation conductance calculation based on a method given in a paper by Derneryd [4] is now presented. From the previous discussion, a microstrip line terminated in an open circuit generates radiation in the region external to the top conductor. With the assumption of an electrically thin substrate, Derneryd attributes the radiation to the electric fields in the vicinity of the open end, external to the dielectric substrate. The flux

lines of these fields are shown in Fig. 3.2a, with vertical and horizontal components directed along the y and x axis, respectively. It is assumed that the E field component parallel to the x axis is constant at the substrate surface. The region of constant electric field is shown in Fig. 3.2b, with E_x constant in the region $-\ell \leq z \leq \ell$ and $-d/2 < x < d/2$. E_x is assumed to be zero elsewhere in the x-z plane. Thus, the substrate surface outside the dashed line of Fig. 3.2b can be replaced by a perfect electrical conductor. This transforms the problem into a slot, containing a constant E field radiating into the upper half space. The size of the slot has, of course, been somewhat arbitrarily selected. However, as well become apparent later, the conductance so obtained is actually independent of the slot width. The tangential E field in the slot can be replaced by a magnetic current density given by

$$\bar{a}_z J_m = 2\bar{a}_x E_x \times \bar{a}_y \quad . \tag{3.3}$$

The factor 2 in (3.5) accounts for the imaging effects of the ground plane. The problem, therefore, has been reduced to a magnetic current density radiating into the region $y > 0$. The equivalent problem is shown in Fig. 3.3 where

$$J = 2E_x \qquad |x| < \frac{d}{2} \; ; \; |z| < \ell$$

$$= 0 \qquad \text{elsewhere} \quad .$$

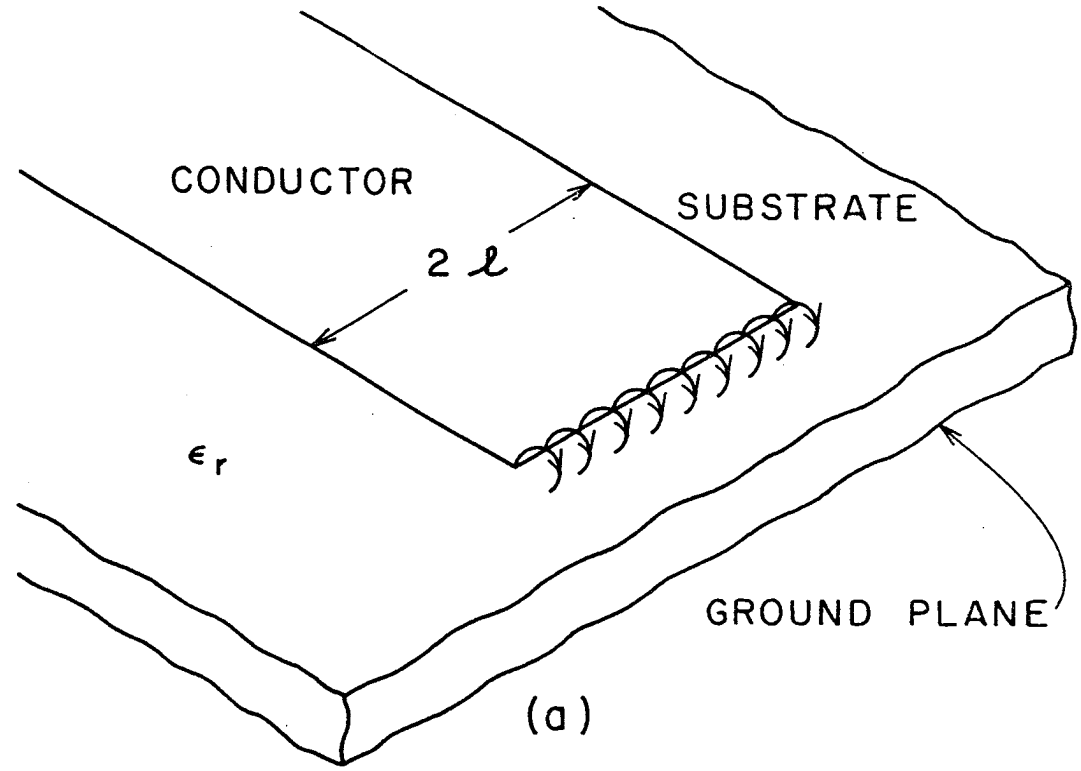
CONDUCTOR
SUBSTRATE
2 ℓ
ϵ_r
GROUND PLANE
(a)

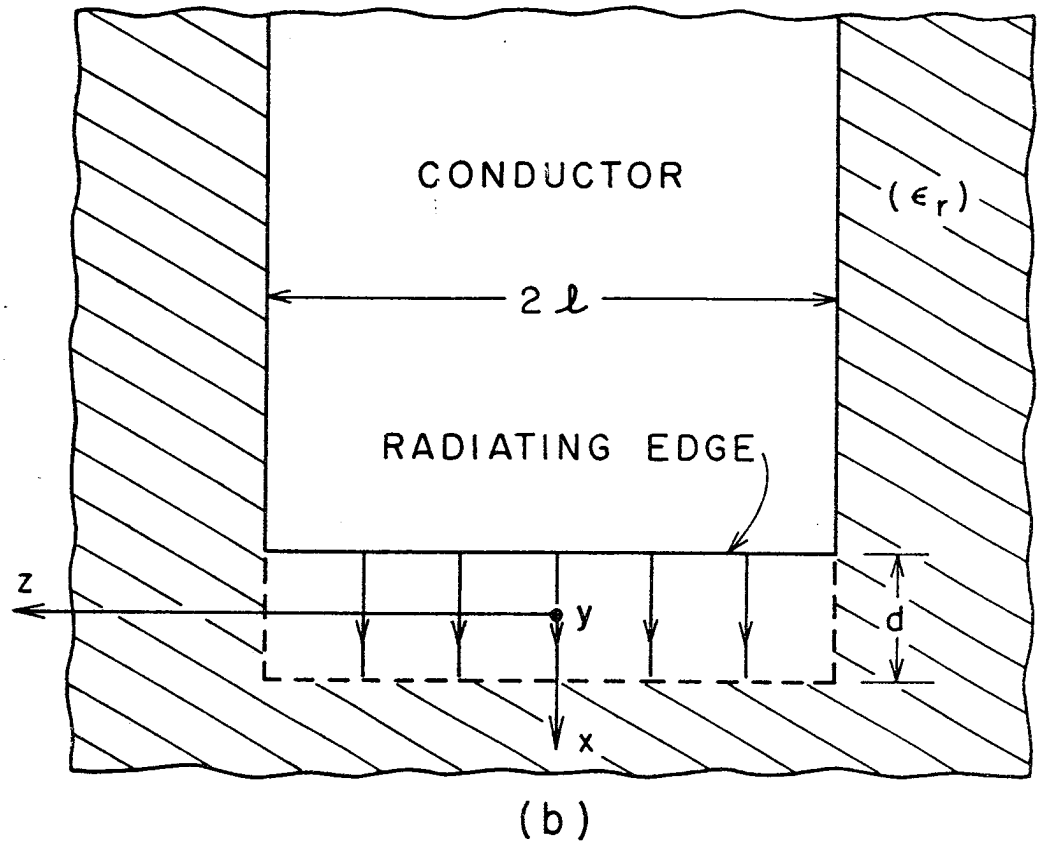
CONDUCTOR
(ϵ_r)
2 ℓ
RADIATING EDGE
z
y
d
x
(b)

Fig. 3.2.

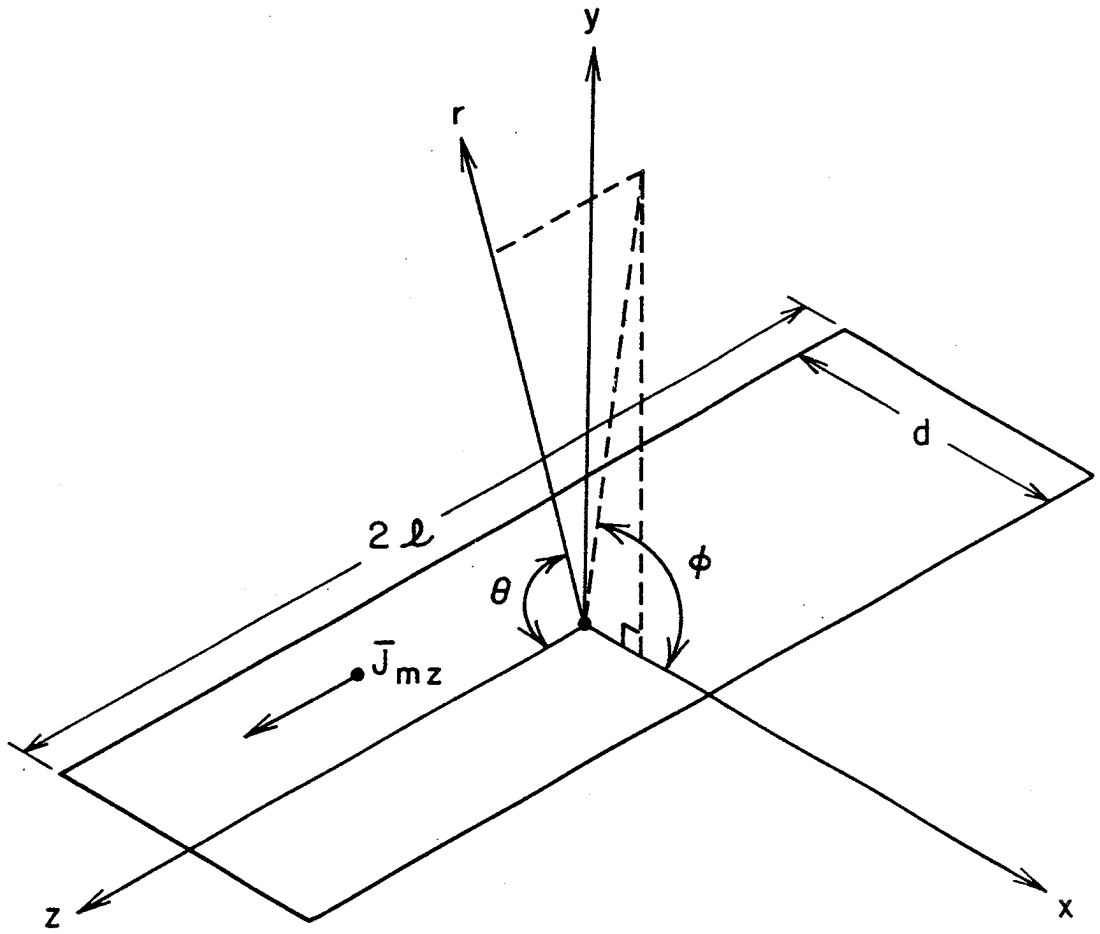

Fig. 3.3.

The vector potential function associated with this current density can be found by integrating over the magnetic current source as follows:

$$\bar{F} = \frac{\bar{a}_z e^{-jk_o r}}{4\pi r} \int_{-\ell}^{\ell} \int_{-\frac{d}{2}}^{\frac{d}{2}} 2E_x e^{jk_o(x' \sin\theta \cos\phi + y' \cos\theta)} \, dx' \, dz'$$

Performing the integration obtains

$$F_z = \frac{e^{-jk_o r}}{4\pi r} 2E_x \ell d \frac{\sin\left(\frac{k_o d}{2} \sin\theta \cos\phi\right) \sin\left(k_o \ell \cos\theta\right)}{\left(\frac{k_o d}{2} \sin\theta \cos\phi\right)\left(k_o \ell \cos\theta\right)} \tag{3.4}$$

For $k_o d << 1$, the sine function containing $k_o d$ becomes unity, so Eq. (3.7) can be rewritten as

$$F_z = \frac{e^{-jk_o r}}{k_o \pi r} (E_x d) \frac{\sin(k_o \ell \cos\theta)}{\cos\theta} \tag{3.5}$$

From Harrington [21], the farzone E field component is related to the potential F by the following equation:

$$E_\phi = -jk_o F_z \sin\theta \quad . \tag{3.6}$$

Applying Eq. (3.5) to Eq. (3.6) yields

$$E_\phi = -j \frac{(E_x d)}{\pi} \frac{e^{-jk_o r}}{r} \frac{\sin(k_o \ell \cos\theta)}{\cos\theta} \sin\theta \quad . \tag{3.7}$$

In the farzone, the H field is given by

$$H_\theta = \frac{-E_\phi}{\eta_o} \quad . \tag{3.8}$$

In order to determine a conductance, the radiated power must be evaluated in the farzone by means of a Poynting integration over a hemisphere of radius r. The required integral is

$$P_{rad} = \frac{1}{2} \int_s \mathrm{Re}[\hat{\bar{E}} \times \hat{\bar{H}}^*] \cdot d\bar{s} \tag{3.9}$$

Applying Eqs. (3.7) and (3.8) to (3.9) yields

$$P_{rad} = \frac{(E_x d)^2}{2\pi^2 \eta_o} \int_0^\pi \int_0^\pi \frac{\sin^2(k_o \ell \cos\theta)}{\cos^2\theta} \sin^3\theta \, d\theta \, d\phi \quad . \tag{3.10}$$

The voltage across the slot is

$$V_o = E_x d \quad . \tag{3.11}$$

Inserting Eq. (3.11) into (3.10) and integrating with respect to ϕ results in the following expression for power:

$$P_{rad} = \frac{V_o^2}{240\pi^2} \int_0^\pi \frac{\sin^2(k_o \ell \cos\theta)}{\cos^2\theta} \sin^3\theta \, d\theta \quad . \tag{3.12}$$

In terms of the slot voltage and the radiated power, the radiation conductance is given by

$$P_{rad} = \frac{V_o^2 G}{2} \quad . \tag{3.13}$$

Combining Eqs. (3.12) and (3.13) yields

$$G = \frac{I}{120\pi^2} \tag{3.14}$$

where I denotes the integral (omit the constant multiplier) portion of Eq. (3.12). The integral I can be easily evaluated by applying the transformation $x = \cos\theta$. The resulting expression contains trigonometric functions and a sine integral term. The limiting forms of Eq. (3.14) then become

$$G = \frac{k_o \ell}{120\pi} \quad (k_o\ell >> 1;\ k_o d << 1) \tag{3.15}$$

$$G = \frac{(k_o \ell)^2}{90\pi^2} \quad (k_o\ell << 1;\ k_o d << 1) \quad . \tag{3.16}$$

Eq. (3.15) indicates that the radiation conductance varies linearly as a function of $k_o\ell$ in the case of an electrically wide strip. From Eq. (3.16), a narrow strip results in a square law conductance variation. A comparison of the conductance of Eq. (3.16) and the Wiener-Hopf conductance is of interest since these are applicable to wide strips. For a wide microstrip line, the characteristic impedance is

$$z_o = \frac{120\pi}{n} \left(\frac{d}{2\ell}\right) \quad . \tag{3.17}$$

Combining Eqs. (3.17) and (3.15) yields the normalized conductance

$$g = \frac{k_o d}{2n} \quad (k_o \ell >> 1;\ k_o d << 1) \quad . \tag{3.18}$$

Eq. (3.18) agrees with the approximate formula (2.37), which comes as no surprise since the Wiener-Hopf approximations apply to electrically wide strips and electrically thin substrates. Because these conditions are met in many practical sitautions, Eq. (3.18) is widely used in design problems.

Referring to Fig. 3.2b, the x-directed E field on the surface of the substrate is assumed to extend a distance d from the edge of the conductor at the open end. The choice of d, as mentioned before, seems rather arbitrary. Inspection of Eq. (3.11) indicates that the choice of d affects the slot voltage, but it does not affect the shape of the farzone pattern since $k_o d << 1$. When the conductance is calculated from the radiated power, a cancallation of voltage terms occurs, resulting in an unnormalized conductance, independent of d. If, therefore, E_x were assumed to extend by the distance bd ($b \neq 1$; $bk_o d << 1$) beyond the open end, the resulting conductance would still be given by Eq. (3.15), due to the voltage cancellation. Thus, the choice of the E field extension is arbitrary as long as the electrical substrate thickness is much smaller than 1.

3.4. An Open-End Susceptance Calculated from Static Considerations

In the last section, the conductance is found by use of a slot radiation calculation. Since only the far fields are considered, no susceptance information can be obtained using this approach. One can, however, determine the aperture susceptance by an alternative formulation. A widely used approach is to assume a static charge distribution on the microstrip transmission system as is shown in Fig. 3.4a. The top conductor is at a constant potential ϕ_T with respect to the ground plane. On account of the open end, an excess charge accumulation occurs on the top conductor in the region near the discontinuity. The excess charge concentration can be characterized by the open-end capacitance C_{oc} of Fig. 3.4b. In terms of the capacitance, the open end susceptance is written as

$$bY_o = 2\pi f C_{oc} \quad .$$

The static formulation, then, results in a susceptance that is a linear function of frequency. The Wiener-Hopf susceptance of Chapter II, on the other hand, is a nonlinear function of frequency, characterized by a dynamic capacitance. Clearly, the static approach neglects the high frequency effects of the discontinuity. The significance of this will be discussed in Chapter V.

According to Gupta [14], there are four approaches used in the numerical computation of C_{oc}; these are the matrix inversion

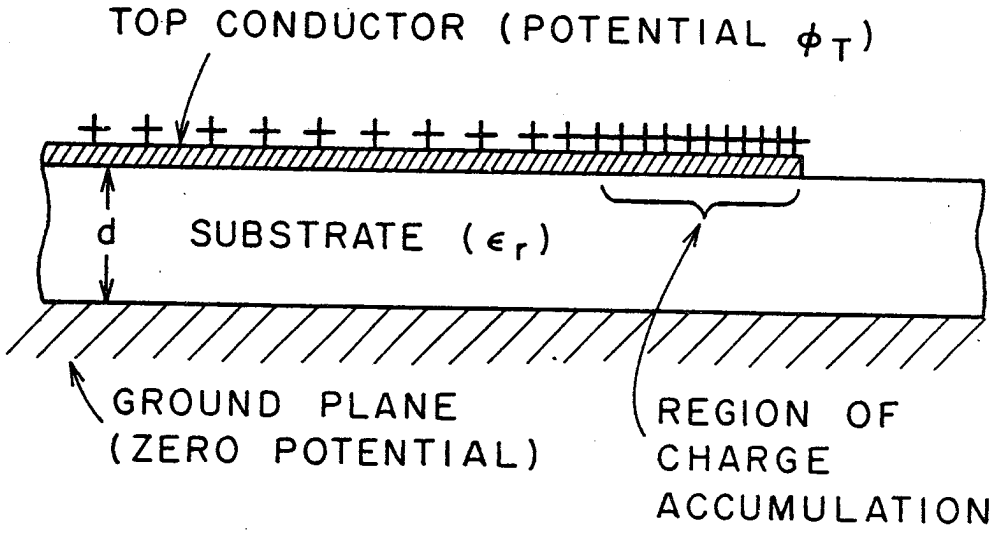
TOP CONDUCTOR (POTENTIAL ϕ_T)
d
SUBSTRATE (ϵ_r)
GROUND PLANE
(ZERO POTENTIAL)
REGION OF
CHARGE
ACCUMULATION

(a)

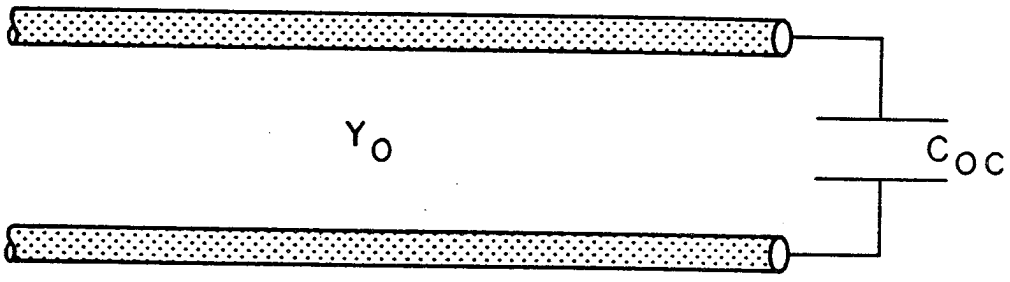
Y_O
C_{OC}

(b)

Fig. 3.4.

method, the variational method, Galerkin's method in the spectral domain, and the method of line sources with charge reversal. The first three utilize the configuration of Fig. 3.5a, a microstrip line of length H and width 2ℓ. The fringe capacitance is determined from the following limit:

$$C_{oc} = \frac{1}{2} \lim_{H \to \infty} [C_t(H) - C \times H]$$

in which C_t is the total capacitance of the finite length line of Fig. 3.5a, which includes the effect of fringing at both ends. In order to isolate the contribution due to the fringe field, the capacitance of a section of width 2ℓ and length H in an infinitely long microstrip line must be subtracted from $C_t(H)$. This term is $C \times H$ in Eq. (3.19), where C is the capacitance per unit length of an infinite line. As H becomes larger, the coupling effects between the two ends are reduced until, in the limit, Eq. (3.19) represents the fringing capacitance of a semi-infinite microstrip line terminated in an open circuit. To permit evaluating Eq. (3.22) numerically, H is increased in increments, and the difference

$$\frac{C_t(H) - C \times H}{2}$$

is computed at each H. Beyond a certain point in the iteration, the difference converges to C_{oc}. An accuracy problem arises, however, since $C_t(H)$ and $C \times H$ are two large and nearly equal

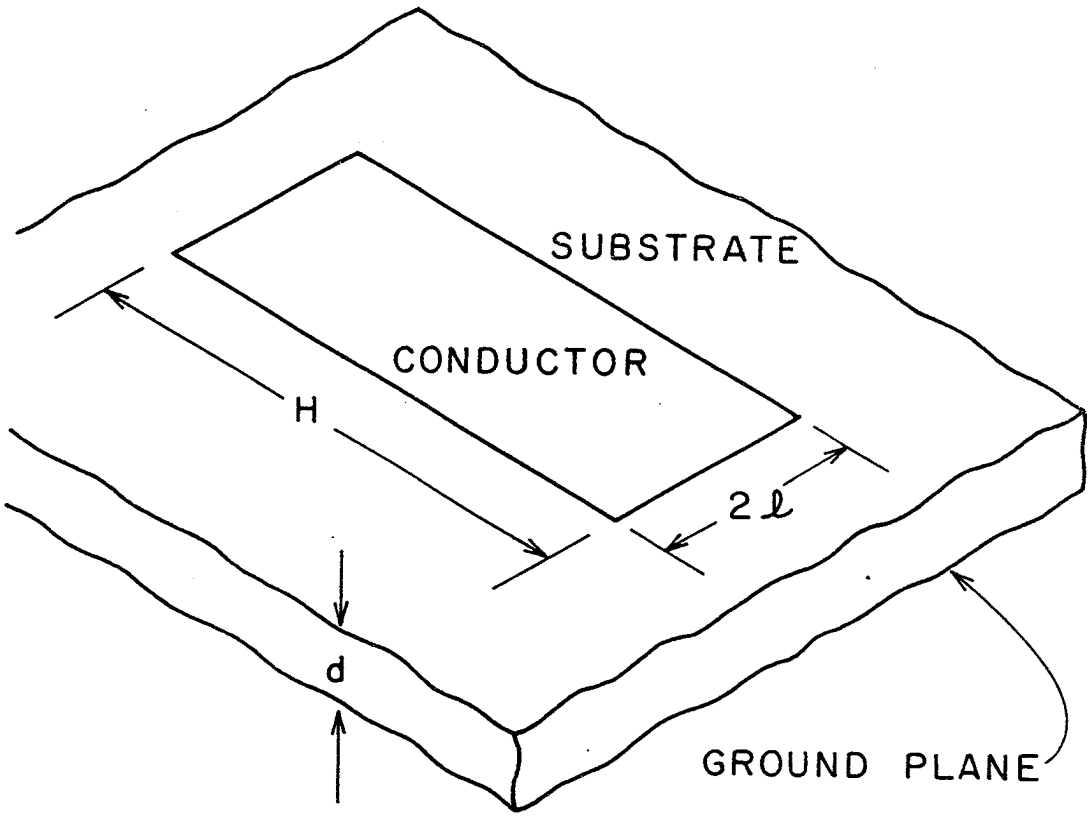

(a)

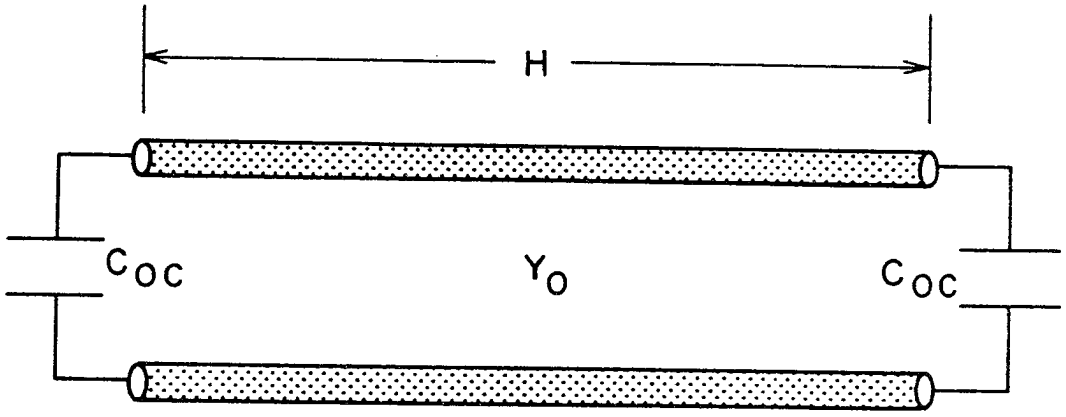

(b)

Fig. 3.5.

quantities. The first three methods, mentioned earlier, utilize Eq. (3.19) to calculate C_{oc}. Thus, because of this fact, they suffer from error accumulation during the computation process.

In order to circumvent the accuracy difficulty inherent in the first three approaches, Silvester and Benedek [3] have developed the method of line sources with charge reversla as a means for computing C_{oc}. Fig. 3.6 shows an infinitely long microstrip line of width 2ℓ supported by a substrate of thickness d and permittivity ε_r. Mathematically, the top conductor can be represented in terms of z-directed, infinitely long line sources. A single such line source is shown in Fig. 3.6. Referring to this figure, the functional form of a single line source component is written as

$$K \rho_s(y')\delta(x - d)\delta(y - y') \tag{3.20}$$

wherein K is a constant multiplier, and δ is the Dirac delta function, and the primed variables denote the location of the line source. It is observed in Eq. (3.20) that the charge density on the top conductor for an infinitely long line is a function of only the transverse variable y'. Consider now the line source of Fig. 3.7, supported by a substrate of thickness d and relative permittivity ε_r. Assuming that the charge density $+\rho$ of the line is uniform, the appropriate Green's function for this region is given by $G_e(x,y,z'y')$. The integral equation relating the charge density $\rho(y')$ on the top conductor (zero thickness) to

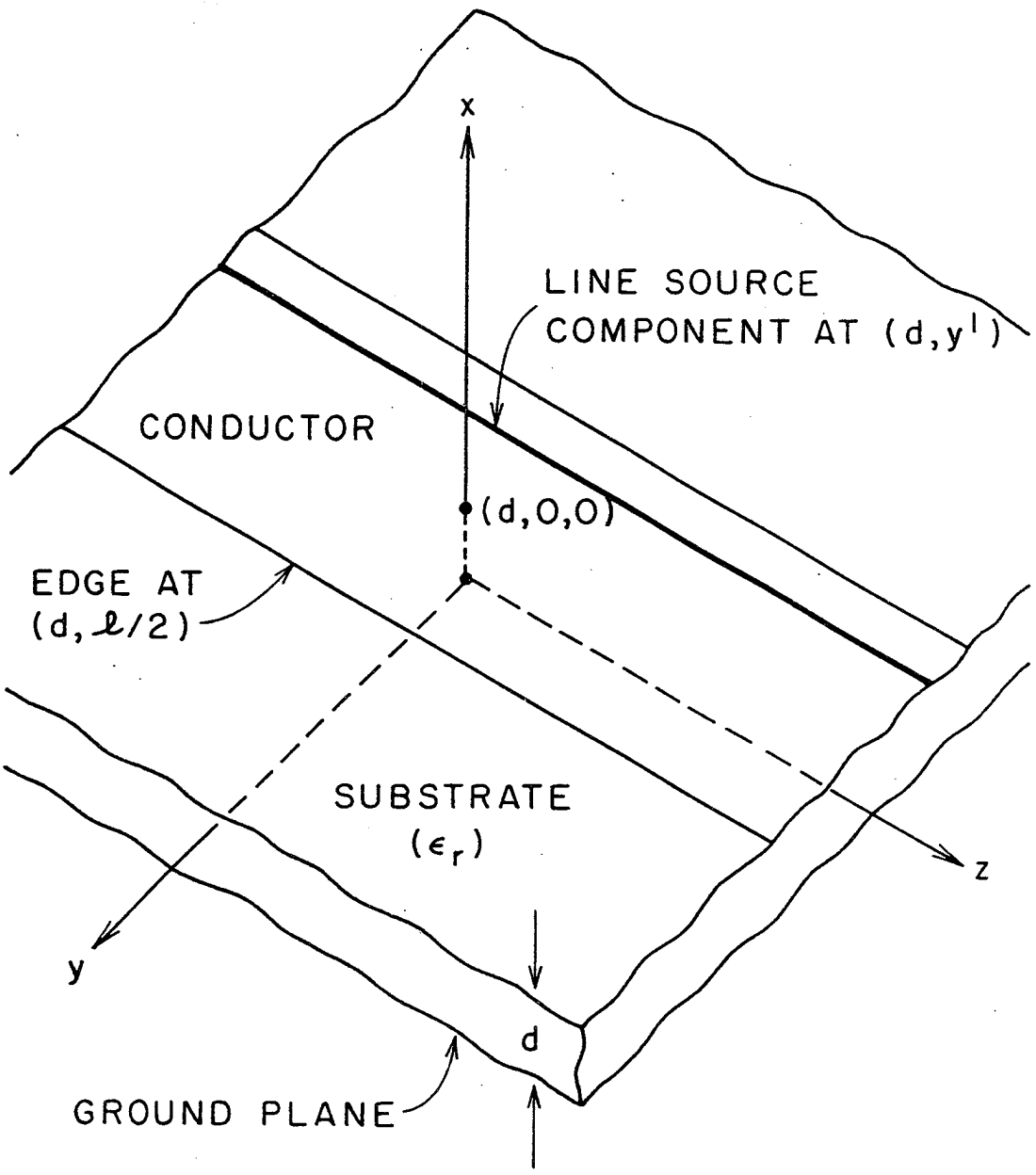
x
LINE SOURCE
COMPONENT AT (d,y')
CONDUCTOR
(d,0,0)
EDGE AT
(d, ℓ/2)
SUBSTRATE
(ε_r)
z
y
d
GROUND PLANE

Fig. 3.6.

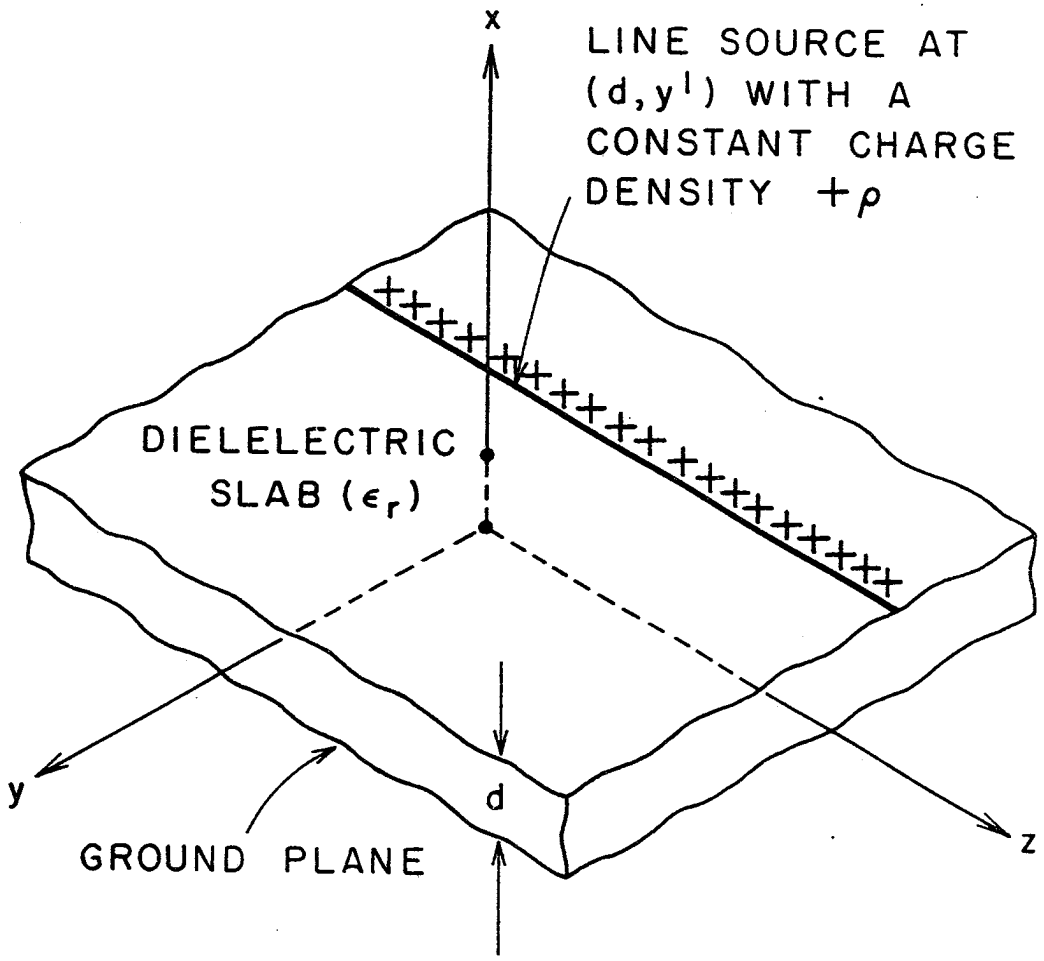
x
LINE SOURCE AT
(d, y') WITH A
CONSTANT CHARGE
DENSITY +ρ
DIELELECTRIC
SLAB (ε_r)
y
d
z
GROUND PLANE

Fig. 3.7.

the electrostatic potential for the infinitely long microstrip line of Fig. 3.6 is given by

$$\phi_e(x,y,) = \int_{-\ell}^{+\ell} \rho(y')G_e(x,y;y')dy' \quad . \tag{3.21}$$

Since the potential on the top conductor is constant, Eq. (3.21) can be solved for the charge density on the top conductor with solutions obtainable using numerical methods.

At this point, consider the open end microstrip line of Fig. 3.8. Assume that the charge density on the top conductor is $\rho(y')$, the same density that occurs on the infinite line. In order to formulate an integral equation of the form of Eq. (3.21), a Green's function for a semi-infinite line source must be found. The process by which the appropriate Green's function is determined is shown in Fig. 3.9. In the three parts of this figure, the line sources are associated with a substrate of thickness d and relative permittivity ε_r. The substrate, infinite in extent, rests on top of a perfectly conducting ground plane. The line source of Fig. 3.9a, with a uniform charge density $+\rho$ distributed along its length, has already been discussed. Fig. 3.9b shows a line source which has a constant charge density $+\rho$ for $z > 0$ and a constant but opposite charge density $-\rho$ for $z < 0$. This charge distribution cannot be synthesized physically, but it is mathematically valid. The Green's function, associated with this line source is $G_o(x,y,z;y')$. If the charge densities of parts a

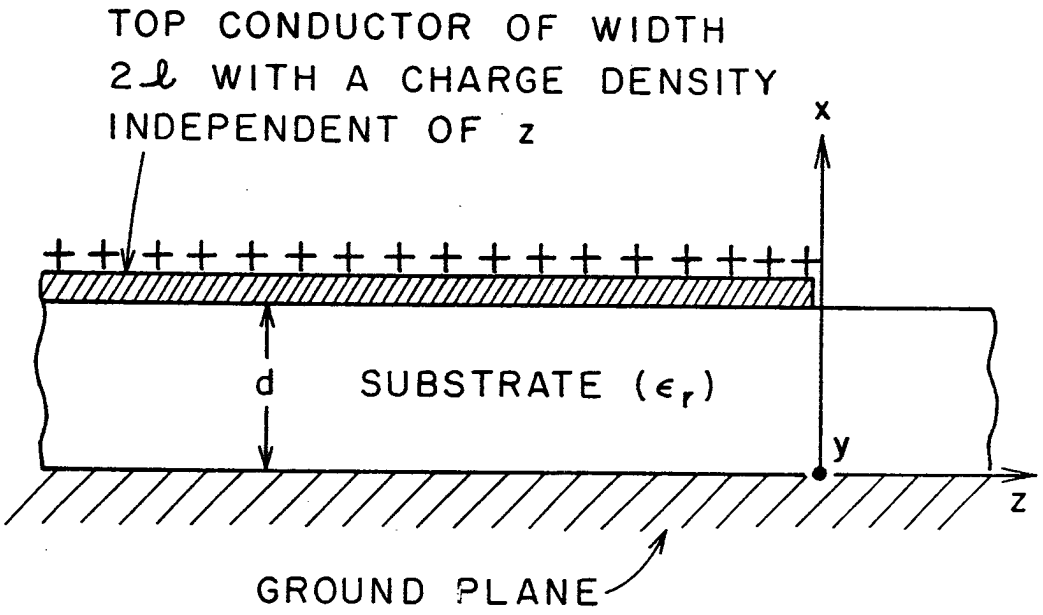
TOP CONDUCTOR OF WIDTH
2ℓ WITH A CHARGE DENSITY
INDEPENDENT OF z
x
d
SUBSTRATE (ε_r)
y
z
GROUND PLANE

Fig. 3.8.

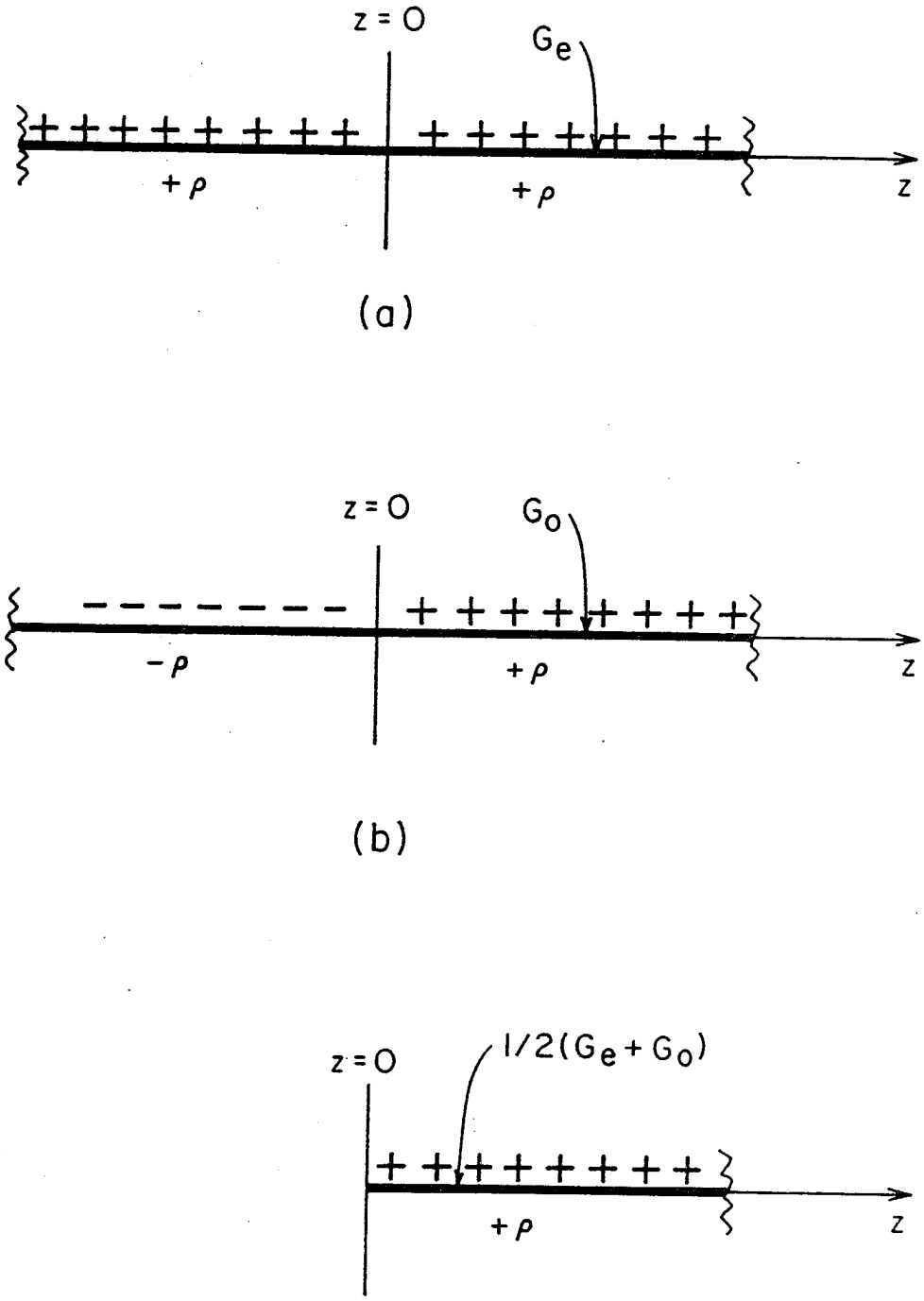

Fig. 3.9.

and b are superimposed, the resulting line source is semi-infinite with a constant charge density in the region $z > 0$ as is illustrated in Fig. 3.9c. Thus, the Green's function of this source can be found by combining the Green's functions of parts a and b (Fig. 3.9). The Green's function for the semi-infinite line source, then, is

$$G_{si}(x,y,z;y') = \frac{1}{2}\left[G_e(x,y,z;y') + G_o(x,y,z;y')\right] \qquad (3.22)$$

Therefore, the integral equation which applies to the semi-infinite microstrip of Fig. 3.8 is given by

$$\phi_{si}(x,y,z) = \int_{-\ell}^{+\ell} \rho(y')G_{si}(x,y,z;y')dy' \ . \qquad (3.23)$$

Assume now that ϕ_e and ϕ_{si} are the electrostatic potentials that exist on the top conductors of the infinite and the semi-infinite lines, respectively. Since $\rho(y')$ in Eq. (3.23) has no z' dependence, the potential ϕ_{si} is not constant on the top conductor. In order to satisfy the boundary conditions, the potential on the top conductor must be a constant. To force the potential to be the constant value ϕ_e, an excess charge must be added to the top conductor. This excess charge density, denoted by $\rho_e(y',z')$, has both a y' and z' dependence. The corresponding integral equation, from which the required excess charge is obtained, is given by

$$\phi_e - \phi_{si} = \int_0^{\infty} \int_{-\ell}^{\ell} \rho_e(y',z') G_{si}(x,y,z;y',z') dy' \, dz' \quad . \qquad (3.24)$$

Adding the potential defined by Eq. (3.24) to that of Eq. (3.23) results in the constant potential ϕ_e on the top conductor. Since ϕ_{si} can be determined from Eqs. (3.21) and (3.23) (ϕ_e is a known constant), the functions ϕ_{si} and G_{si} that appear in Eq. (3.26) may be regarded as being known. The equation (3.24), then, provides a suitable integral equation for determining the excess charge density directly. Once the excess charge density $\rho_e(y',z')$ is known, the open end capacitance is found by integrating the charge density over the top conductor as follows:

$$C_{oc} = \frac{1}{\phi} \int_0 \int_{-\ell}^{\ell} \rho_e(y',z') dy' \, dz' \quad . \qquad (3.25)$$

Silvester and Bendek [3] solve the integral equation (3.24) using numerical methods and thereby generate C_{oc} from Eq. (3.25). The computing strategy they use is not discussed here. The Green's functions associated with the line sources of Figs. 3.9a and 3.9b are derived in a paper by Silvester [22] using the method of partial images. The Green's functions used in the numerical solution are

$$G_o(d,y,z;y') = \frac{1 - k}{4\pi\varepsilon_o\varepsilon_r} \left[f(0) - (1 - 1) \sum_{m=1}^{\infty} K^{m-1} f(m) \right]$$

where

$$K = \frac{\varepsilon_o - \varepsilon_r \varepsilon_o}{\varepsilon_o + \varepsilon_r \varepsilon_o}$$

and

$$f(n) = \ell n \left[\frac{\sqrt{z^2 + 4n^2 d^2 + (y - y')^2} + z}{\sqrt{z^2 + 4n^2 d^2 + (y - y;)^2} - z} \right].$$

Also,

$$G_e(d,y;y') = \frac{1}{2\pi(\varepsilon_o + \varepsilon_r \varepsilon_o)} \sum_{m=1}^{\infty} K^{n-1}$$

$$\times \ell n \left[\frac{4n^2 + \left(\frac{y + y'}{d}\right)^2}{4(n - 1)^2 + \left(\frac{y - y'}{d}\right)^2} \right] .$$

Although the region of integration in Eq. (3.24) covers the semi-infinite strip, the integral equation can be effectively solved using numerical methods since $\phi_e - \phi_{si}$ and $\rho_e(y',z')$ decay rapidly away from the discontinuity. Thus, at a sufficient distance away from the open end (two or three substrate thicknesses) $\phi_e - \phi_{si}$ and $\rho_e(y',z')$ are assumed to be zero for computational purposes. Solving for the excess charge directly provides for the efficient computation of C_{oc} without the problem of error accumulation. The Silvester-Bendek approach, therefore, results in an accurate static capacitance C_{oe}.

Silvester and Bendek provide an extensive tabulation of $C_{oc}/2\ell$ as a function of $2\ell/d$ and the substrate relative

permittivity ε_r. Their results are shown in Fig. 3.10. Since the curves for $C_{oc}/2\ell$ vary so smoothly, an empirical formula for the discontinuity capacitance, derived by Silvester [3] using polynomial curve fitting, is given by

$$\frac{C_{oc}}{2\ell} = 10^{-12} \exp\left[\ell n\ 10 \sum_{i=1}^{5} C_i(\varepsilon_r) \left(\log_{10}\left(\frac{2\ell}{h}\right)\right)^{i-1}\right] \qquad (3.26)$$

The coefficients $C_i(\varepsilon_r)$ are listed in the following table.

Table 3.1

i \ ε_r	1.0	2.5	4.2	9.6	16.0	51.0
1	1.110	1.295	1.443	1.738	1.938	2.403
2	-0.2892	-0.2817	-0.2535	-0.2538	-0.2233	-0.2220
3	0.1815	0.1367	0.1062	0.1308	0.1317	0.2170
4	-0.0033	-0.0133	-0.0260	-0.0087	-0.0267	-0.0240
5	-0.0540	-0.0267	-0.0073	-0.0113	-0.0147	-0.0840

Eq. (3.26) provides a simple method with which to calculate C_{oc}. However, the use of Eq. (3.26) is restricted to values listed in Table 3.1. In order to obtain a more versatile relation, Hammerstad [11] simplifies Eq. (3.26) and expresses the result in terms of the equivalent length as defined by Eq. (2.28). Hammerstad's result is given by

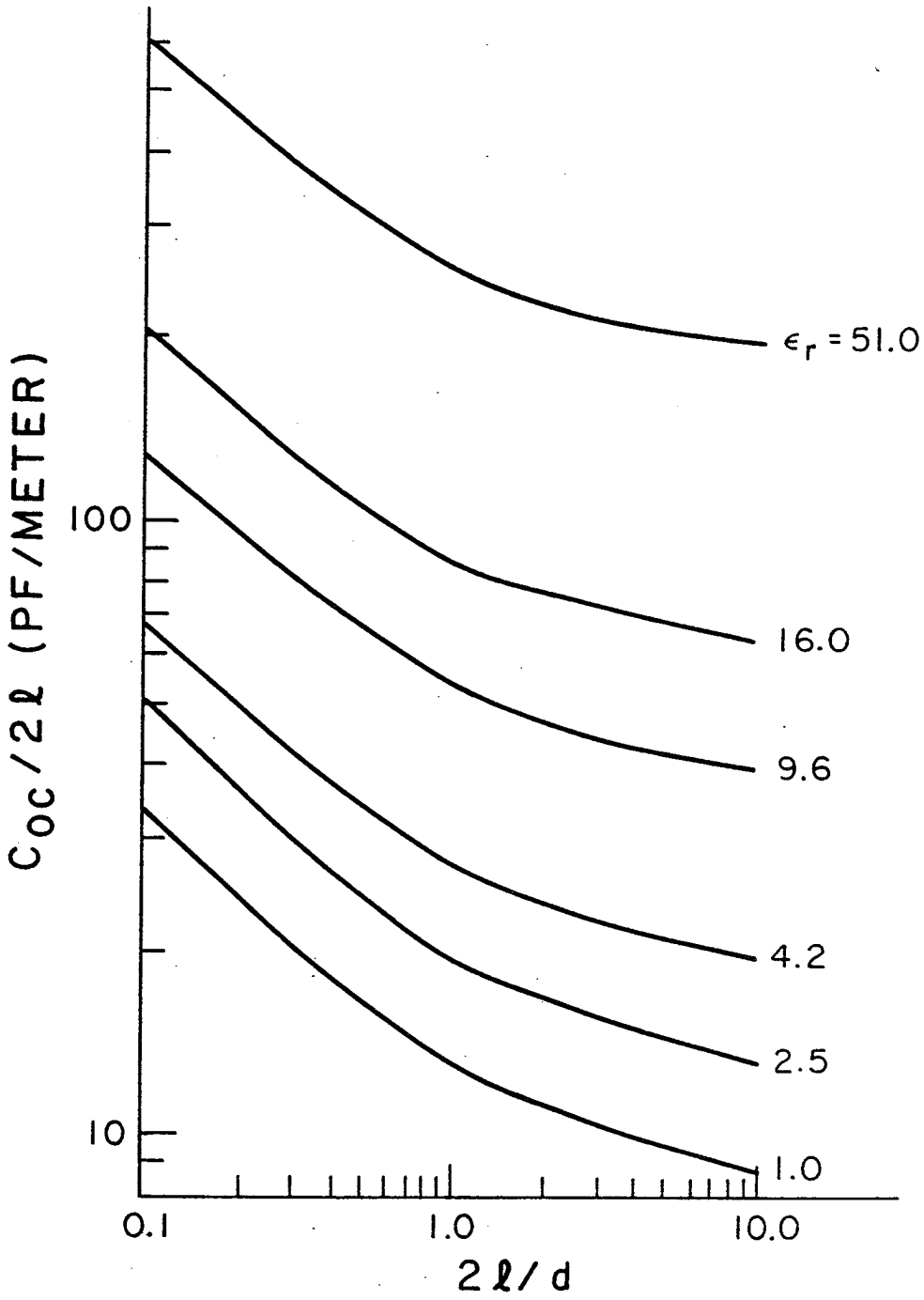

Fig. 3.10 (from [3]).

$$\frac{\Delta h}{d} = 0.412 \frac{(\varepsilon_{re} + 0.3)(2\ell/d + 0.264)}{(\varepsilon_{re} - 0.258)(2\ell/d + 0.8)} \quad . \tag{3.27}$$

In Eq. (3.27), ε_{re} is the effective dielectric constant for the microstrip line. From Gupta [13], simple and accurate formulas for the effective dielectric constant are

$$\varepsilon_{re} = \frac{\varepsilon_r + 1}{2} + \frac{\varepsilon_r - 1}{2} \left(\frac{1}{\sqrt{1 + 6d/\ell}}\right) \quad \left(\frac{2\ell}{d} \geq 1\right) \tag{3.28}$$

$$\varepsilon_{re} = \frac{\varepsilon_r + 1}{2} + \frac{\varepsilon_r - 1}{2} \left(\frac{1}{\sqrt{1 + 6d/\ell}} + 0.04 \left(1 - \frac{2\ell}{d}\right)^2\right)$$

$$\left(\frac{2\ell}{d} \leq 1\right)$$

Eqs. (3.27) has the advantage of being able to generate $\Delta h/d$ and, therefore, C_{oc} for any ε_r. It is found that Eq. (3.27) has no more than a 4% error relative to Eq. (3.26) for $\ell/h \geq 0.1$ and $2 \leq \varepsilon_e \leq 50$.

A comparison of the static susceptance values with the Wiener-Hopf and experimental results is presented in Chapter V.

CHAPTER IV

THE SLOTTED GROUND PLANE SYSTEM AND THE EXPERIMENTAL PROCEDURE

4.1. Introduction

In Chapter II, the reflection coefficient for the fundamental quasi-TEM mode is evaluated for an open end microstrip line. The reflection coefficient, evaluated using the Wiener-Hopf technique, is used to define a normalized end admittance. Since the admittance takes into account the line dispersion as well as the operating frequency, it is truly dynamic in nature. A fundamental question arises, however, as to the validity of applying the solution of the canonical problem of Fig. 2.1 to the truncated structure of Fig. 2.10. Since this approach ignores the coupling between the two edges of the top conductor and the corner effects at the open end, the question that arises is: How accurately does the Wiener-Hopf approach model the open-end admittance? One of the objectives of this chapter is to provide a basis from which the accuracy question can be dealt with.

Sections 3 and 4 of Chapter III provide an alternative characterization of the open-end admittance. The conductance is determined from a conventional slot radiation calculation, while the susceptance is found using an electrostatic solution. It is

clear that this approach lacks the unity of the Wiener-Hopf method because the admittance terms are calculated from two unrelated techniques. The conductance found from the slot calculation agrees completely with the Wiener-Hopf conductance for an electrically thin substrate ($k_o d << 1$) and normal incidence ($\alpha = 0$). The slot conductance calculation, which is not a function of the angle of incidence, does not account at all for the microstrip line dispersion. The Wiener-Hopf susceptance, on the other hand, is found to be in major disagreement with the static formulation. Discrepancies of greater than 25% (relative error) are typical. The next question that naturally arises is: Which of the two approaches more accurately models the open end? In order to answer this question and the previous one, an experiment has to be devised in order to determine the open end admittance. With experimental results, more insight can be gained into the problem of modeling the end admittance.

4.2. Slot Design Considerations

At this point, the problem that must be addressed is how one can experimentally obtain end admittance values. In Chapter II, the E field for the fundamental mode underneath the top conductor of an electrically wide microstrip is given by Eq. (2.31). For convenience, Eq. (2.31) is written here:

$$E_{zo} = A_o \cos(\sqrt{n^2 - \alpha_o^2})e^{-jk_o\alpha_o(x-x_o)}\left[1 + \hat{\Gamma}(\alpha = \sqrt{n^2 - \alpha_o^2})e^{+j2k_o\alpha_o(x-x_o)}\right] .$$

It is apparent from this equation that if a detailed knowledge of the fundamental mode electric field can be gained, then the reflection coefficient $\hat{\Gamma}$ and, therefore, the normalized end admittance can be determined. A requirement of the experiment, then, is to somehow probe the z-directed E field underneath the top conductor of the microstrip line in the region where Eq. (2.34) is valid. As has been mentioned earlier, this region must be located away from the open end and the top conductor edges so that only the fundamental mode field component is present. To allow the higher order modes that are generated at the edges to decay, this distance should be three or four substrate thicknesses.

There are two main considerations in selecting a probing technique. First, the probing arrangement should provide a minimum disturbance of the microstrip fields. Second, the method by which the electric field is probed should be as simple as possible to implement, while at the same time, producing accurate results. In the case of rectangular waveguides and coaxial transmission lines, an approach that fulfills the above criteria is to probe the electric fields by use of a slotted line section in which an E field probe is introduced through a slot. Sketches of waveguide and coaxial slotted lines are shown in Figs. 4.1a and 4.1b. By analogy with these systems, it seems that an appropriate slotted section for a microstrip transmission line should involve a probe through a slot cut in the ground plane as is shown in Figs. 4.2a and 4.2b. In this configuration, the slot, which is cut parallel to the edges of the top conductor, is symmetrically

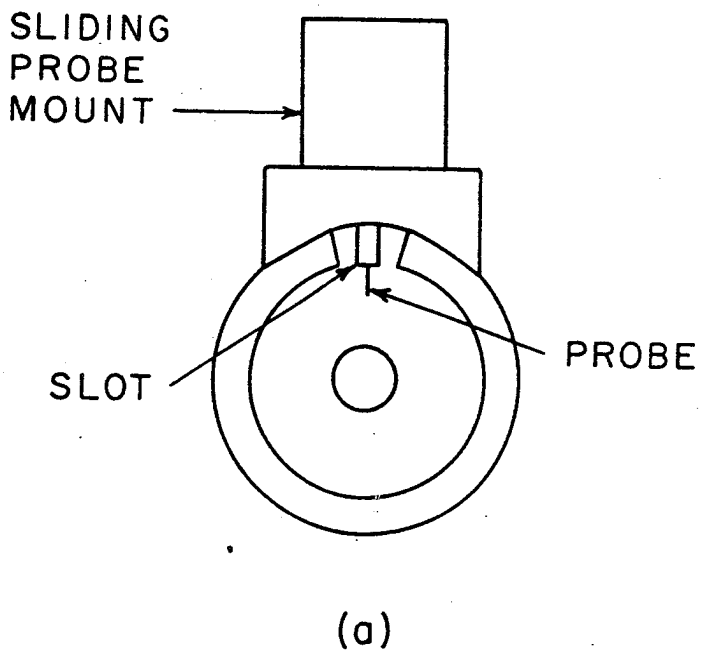
SLIDING
PROBE
MOUNT
SLOT
PROBE

(a)

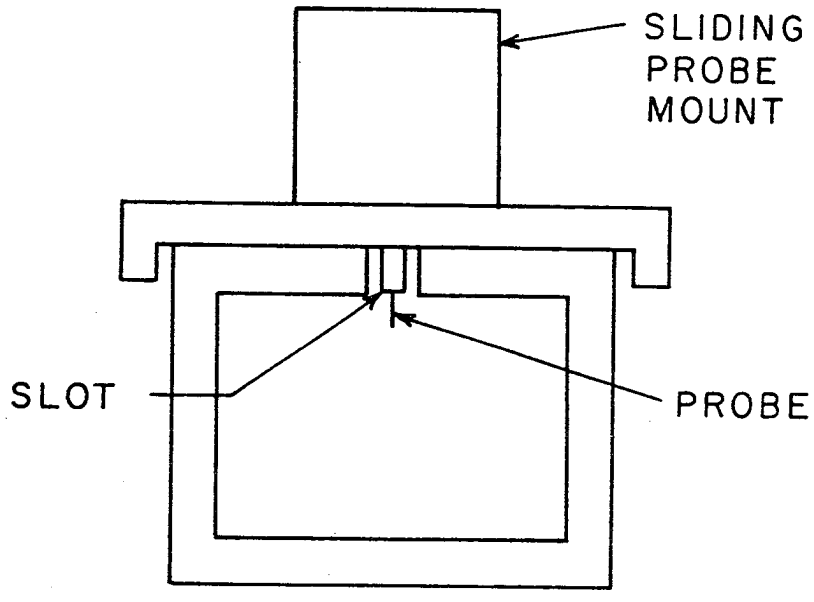
SLIDING
PROBE
MOUNT
SLOT
PROBE

(b)

Fig. 4.1.

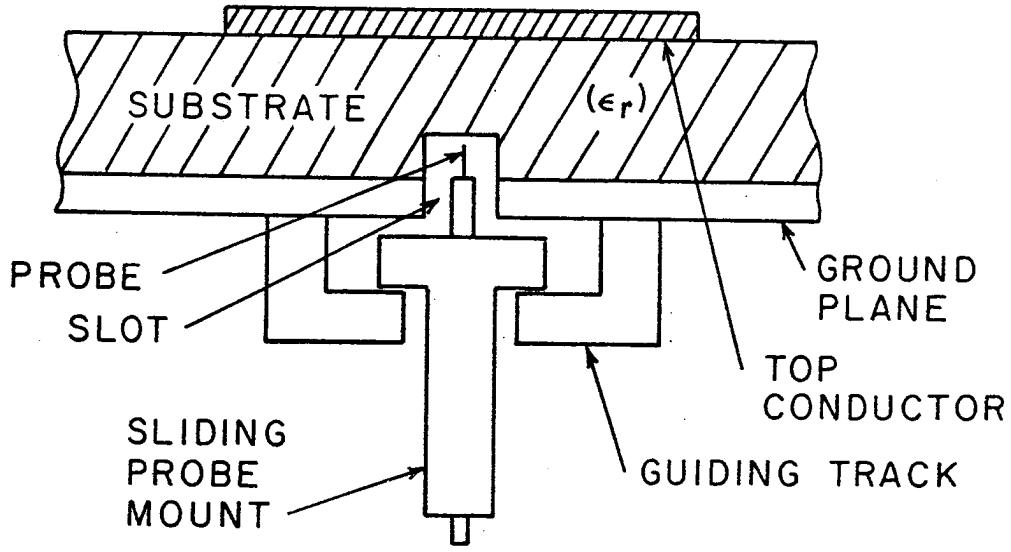
SUBSTRATE
(ϵ_r)
PROBE
SLOT
GROUND PLANE
TOP CONDUCTOR
SLIDING PROBE MOUNT
GUIDING TRACK

(a)

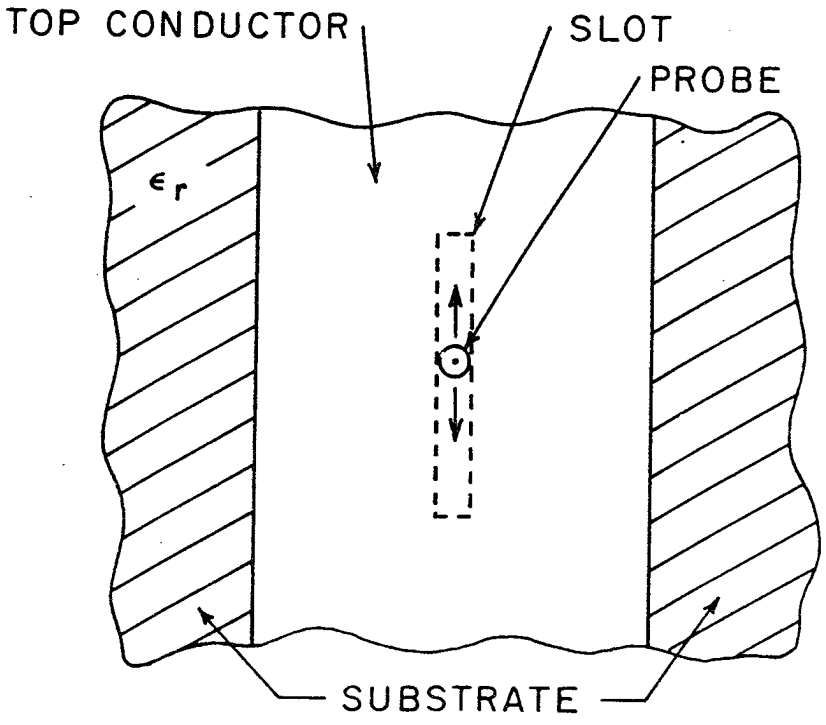
TOP CONDUCTOR
SLOT
PROBE
ϵ_r
SUBSTRATE

(b)

Fig. 4.2.

displaced with respect to the top conductor.

In order to justify more rigorously the slot location, consider the currents which are produced on the ground plane surface by the fundamental mode. From Eqs. (2.29) and (2.30), the form of the ground plane current densities underneath the top conductor are

$$J_{sxo} \propto \cos(\sqrt{n^2 - \alpha_o^2}\, y)$$

$$J_{syo} \propto \sin(\sqrt{n^2 - \alpha_o^2}\, y) \quad .$$

To minimize the field distortion, the slot should be oriented such that the flow of surface currents is not interrupted. From Eq. (2.29), one component of the surface current flows in the x direction. Clearly, since the slot is also oriented in the x direction, only a minimal disturbance of the surface currents of this component occurs. The transverse surface current, which flows in the y-direction, however, appears to be interrupted by the slot. Inspection of Eq. (2.30), however, reveals that the transverse current density is zero at $y = 0$. Thus, the placement of the slot at the $y = 0$ position, as in Fig. 4.2, produces a minimal amount of field distortion. If the slot is not symmetrically displaced, it is evident from Eq. (2.30) that transverse ground plane currents will be interrupted. When this occurs, the microstrip fields will be perturbed from the original configuration, and energy will be radiated from the slot to the region underneath the ground plane. It is important, therefore, to maintain the

position of the slot underneath the center of the top conductor so that accurate information regarding the microstrip electric fields can be obtained. It is also apparent from these considerations that the field distortion effect is reduced as the slot is made narrower. The width of the slot, then, should be made as small as practical considerations allow. Referring once again to Fig. 4.2, an E-field probe extends through the slot by only a short distance into the dielectric substrate. The probe removes a small amount of the power flowing in the microstrip line, and it thereby permits the exploration of the electric field. The penetration of the probe above the ground plane should be kept at the minimum which permits accurate measurements. This minimal penetration is enhanced by making use of a high gain amplifier at the detector output.

4.3. Feed Design Considerations

Up to this point in the discussion relating to the open-end microstrip line, it has been assumed that the incident fundamental mode originates at a point infinitely far away from the discontinuity. This assumption leaves the question unanswered as to how one can practically excite the fundamental mode. One, then, must consider techniques by which the propagating mode can be launched from an external source located at a reasonable distance down the line. There are a number of ways of feeding energy into a microstrip line, but only the coaxial feed is to be considered.

The coaxial feed is shown in Fig. 4.3 in which energy from a source generator is introduced to the microstrip structure by means of a coaxial transmission line. The outer conductor is attached to the bottom of the ground plane so that good electrical contact is made. The center conductor extends vertically through a hole in the ground plane until it makes electrical contact with the top conductor of the microstrip line. In order to ensure strong excitation, the hole in the ground plane should be cut to a diameter of at least four or five times that of the coax inner conductor.

Assuming that the width 2ℓ is such that only the fundamental quasi-TEM mode can propagate, the coax feed introduces this propagating mode as well as higher order evanescent modes. In the region near the feed, higher order waveguide type modes are excited, but these are evanescent, and rapid decay occurs. Thus, this effect is localized to the region immediately around the feed point. The coax feed also introduces a spectrum of TEM waves with z-directed E-fields that propagate radially away from the feed in all directions. The arrows of Fig. 4.4 denote the directions of propagation of some of the TEM waves produced by the coax feed. Since the microstrip structure supports only the fundamental mode, only the plane wave component that is launched at the specific angle ϕ_o will continue to bounce back and forth between the top conductor edges and thereby propagate down the line. The plane waves that are launched at angles other than ϕ_o also are reflected from the top conductor edges, but these decay on account

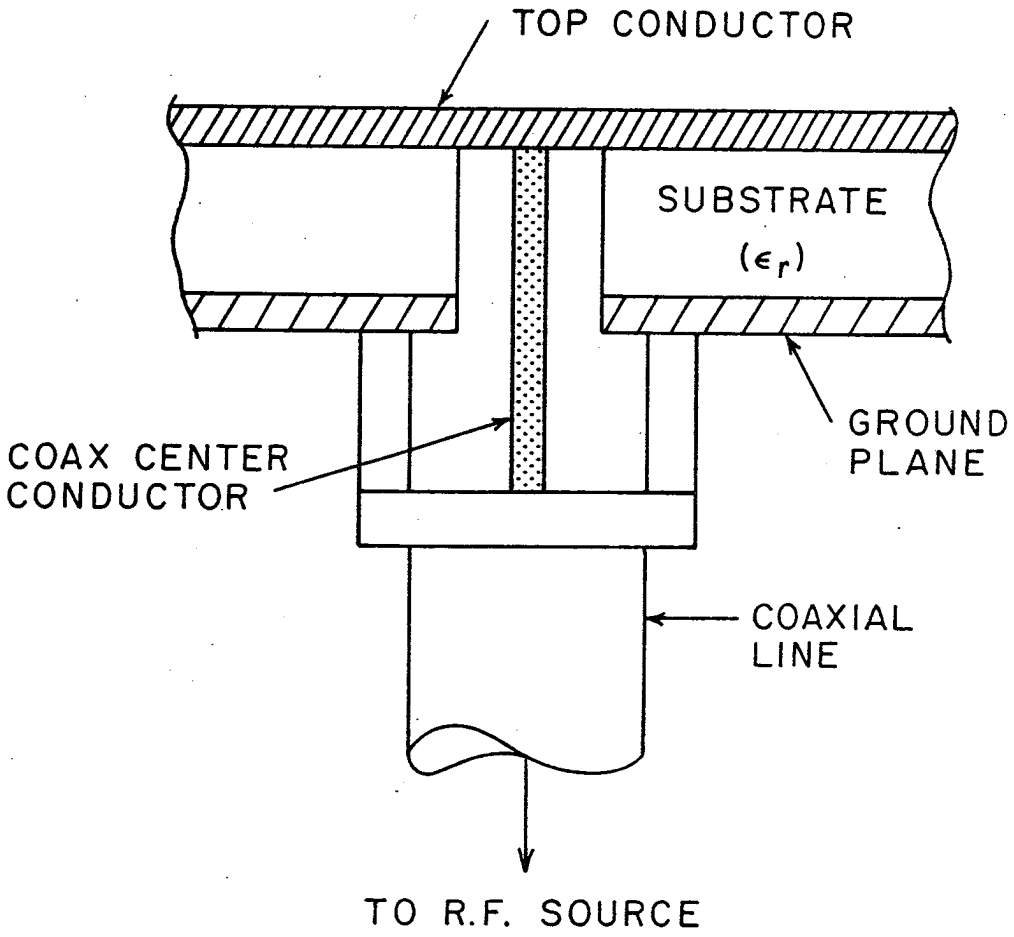
TOP CONDUCTOR
SUBSTRATE
(ϵ_r)
GROUND
PLANE
COAX CENTER
CONDUCTOR
COAXIAL
LINE
TO R.F. SOURCE

Fig. 4.3.

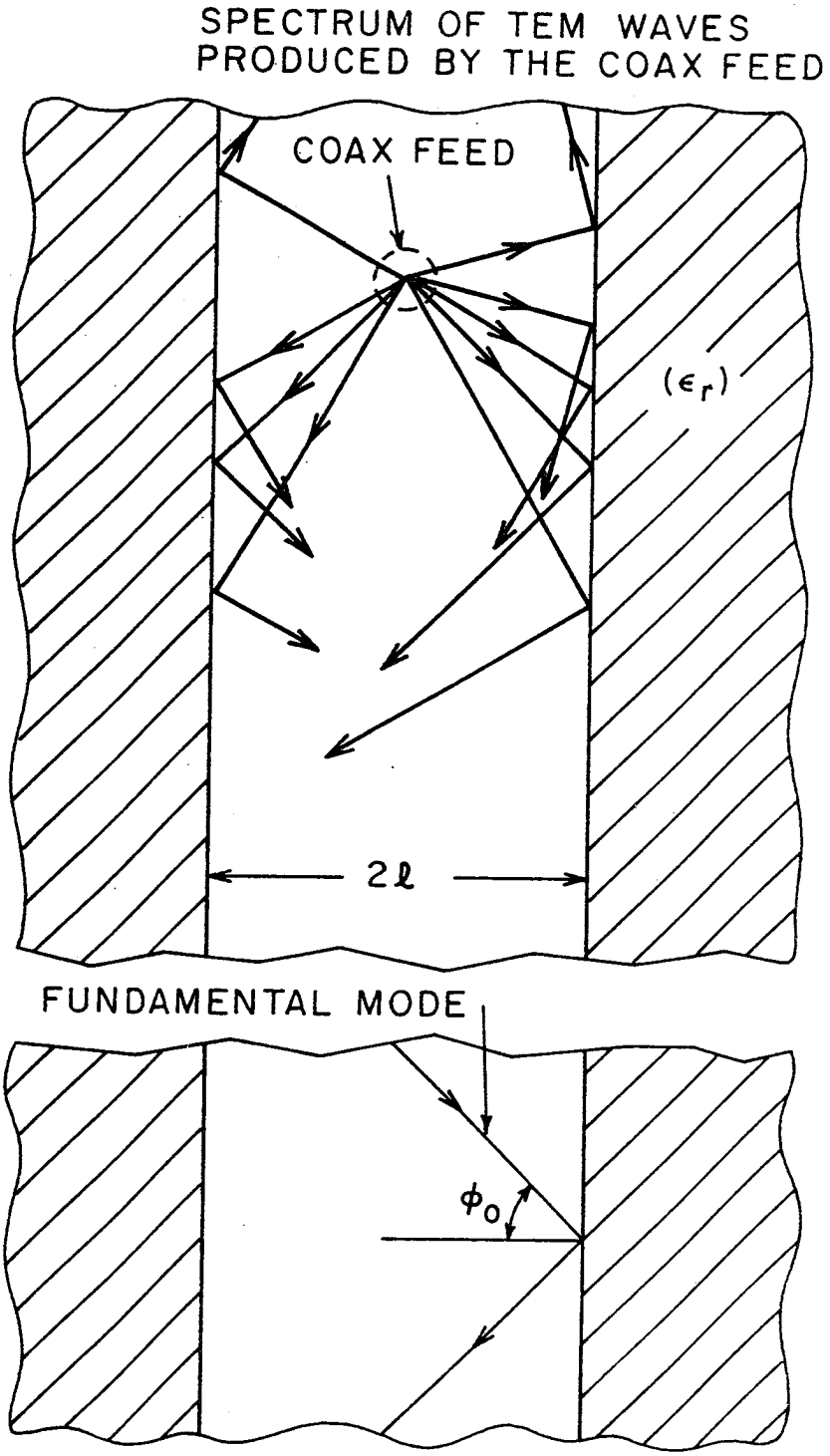
SPECTRUM OF TEM WAVES
PRODUCED BY THE COAX FEED
COAX FEED
(ϵ_r)
2ℓ
FUNDAMENTAL MODE
ϕ_0

Fig. 4.4.

of destructive interference or energy loss produced by radiation and surface wave effects. As the distance from the feed point increases, the modes which are produced by plane waves striking the conductor edges at angles other than ϕ_o will decay until only the fundamental mode is present.

In Fig. 4.3, the coax feed is symmetrically located with respect to the top conductor with the center conductor of the coaxial line protruding vertically from the ground plane. In order to understand reasons for these details, the factors affecting the modal amplitudes should be discussed. From Eqs. (2.27) and (2.28), the fields produced by the fundamental mode and the next higher mode are given by

$$E_{zo} = A_o \cos(\sqrt{n^2 - \alpha_o^2}\, y) e^{-jk_o \alpha_o x} \tag{4.1}$$

$$E_{z1} = A_1 \sin(\sqrt{n^2 - \alpha_1^2}\, y) e^{-jk_o \alpha_1 x} \quad . \tag{4.2}$$

In terms of the experimental setup, which is introduced later in this chapter, the two lowest modes have the most significance. Instead of placing the feed point directly under the center of the top conductor as in Fig. 4.3, assume that the feed is displaced to $x = x'$ and $y = y'$ as is shown in Fig. 4.5a. It is assumed that the coax feed remains underneath the top conductor in the region where Eq. (2.31) is still valid. If the center conductor of the coax feed is assumed to be thin, and the diameter of the hole in the ground plane is assumed to be small, the section protruding

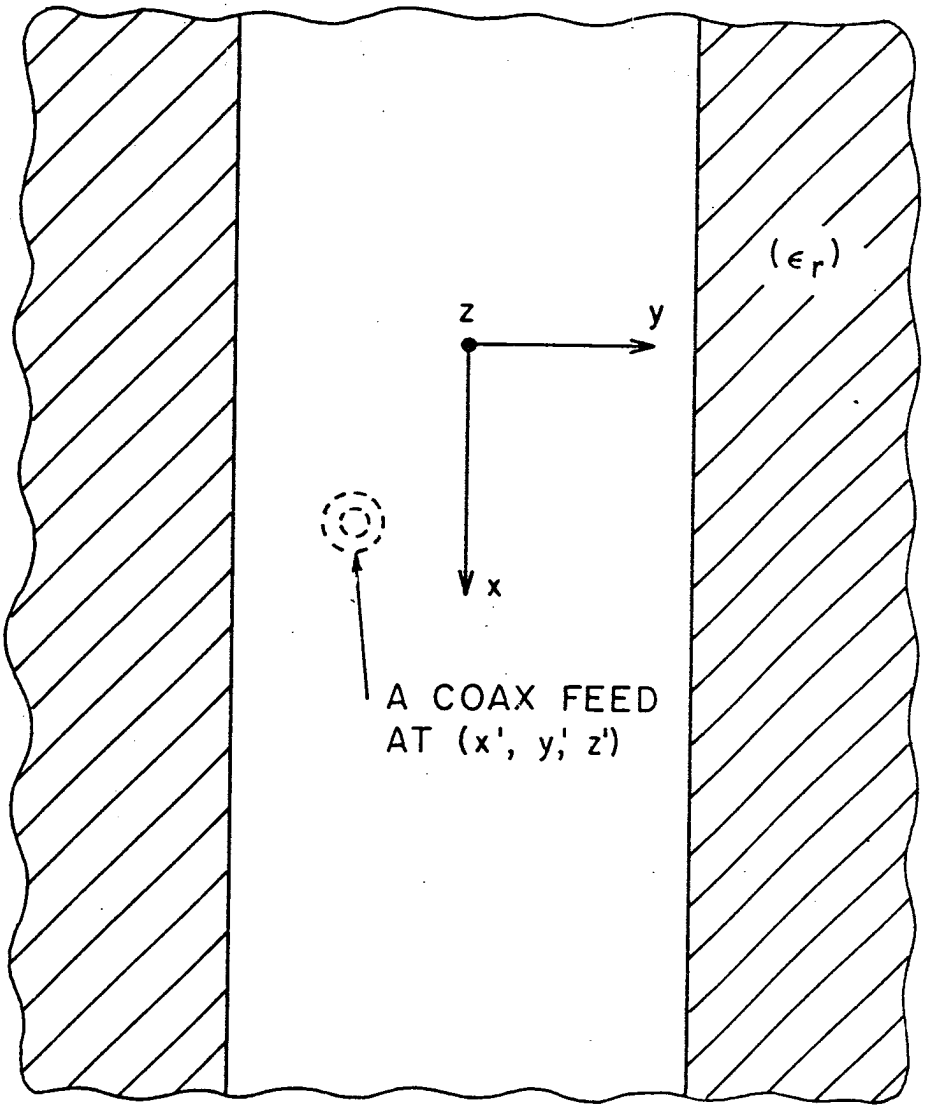

Fig. 4.5a.

above the ground plane can be modeled as a z-directed electric current filament. Since the substrate is electrically thin, the current density of the current filament has no variations in the z-direction. The filament current can be written as

$$\bar{J} = \bar{a}_z[C\delta(y - y')\delta(x - x')] \qquad 0 < z < d \tag{4.3}$$

$$= 0 \qquad \text{elsewhere} .$$

Here, C denotes the constant value of the current density, and δ is the Dirac delta function. Applying the modes as defined by Eqs. (2.27) and (2.28) to a result given by Harrington [21] yields the following proportionality:

$$A_m \propto \int\int\int \bar{J} \cdot \bar{a}_z(E_{zm})dv' \quad . \tag{4.4}$$

In this relation, $\bar{J}$ is the electric current density of the feed point, dv' denoting the volume integration over the feed point. In the case of the equivalent current density of Eq. (4.3), Eq. (4.4) becomes

$$A_m \propto \int_0^d \bar{J} \cdot \bar{a}_m(E_{zm})dz' \quad . \tag{4.5}$$

Eq. (4.5) is maximized when the currnet density $\bar{J}$ is oriented in the z-direction. Thus, the center conductor of the coaxial feed should protrude vertically above the ground plane in order to achieve the maximum amount of excitation. When the current density (4.3) is substituted into Eq. (4.5), proportionalities for

the modal amplitudes of the microstrip modes are generated, becoming

$$|A_m| \propto \cos(\sqrt{n^2 - \alpha_m^2}\, y') \qquad m = 0, 2, 4, \ldots \tag{4.6}$$

$$|A_m| \propto \sin(\sqrt{n^2 - \alpha_m^2}\, y') \qquad m = 1, 3, 5, \ldots \tag{4.7}$$

Eq. (4.6) indicates that the placement of the center conductor of the coax feed at $y = y' = 0$ results in the maximum excitation of the fundamental mode. Also, from Eq. (4.7), it is clear that the next higher ($m = 1$) mode will not be exicted with $y' = 0$, even if the electrical width $k_o \ell$ is large enough to allow the $m = 1$ mode to propagate. In fact, with $y' = 0$, the fundamental mode will be the only propagating mode until $k_o \ell$ increases to the point where the $m = 2$ (even) mode is allowed to propagate. Thus, when the feed point is placed at $y' = 0$, the microstrip line can become electrically wider before higher modes appear than if $y' \neq 0$.

4.4. General Features of the Microstrip Slotted Line System

Having considered the placement of the slot and the coax feed, the general features of the system of Fig. 4.5, on which the measurements are to be performed, are now discussed. The configuration of Fig. 4.5 differs from the ones previously dealt with in that the top conductor, the ground plane, and the substrate possess finite dimensions. The top conductor has a length $2h$

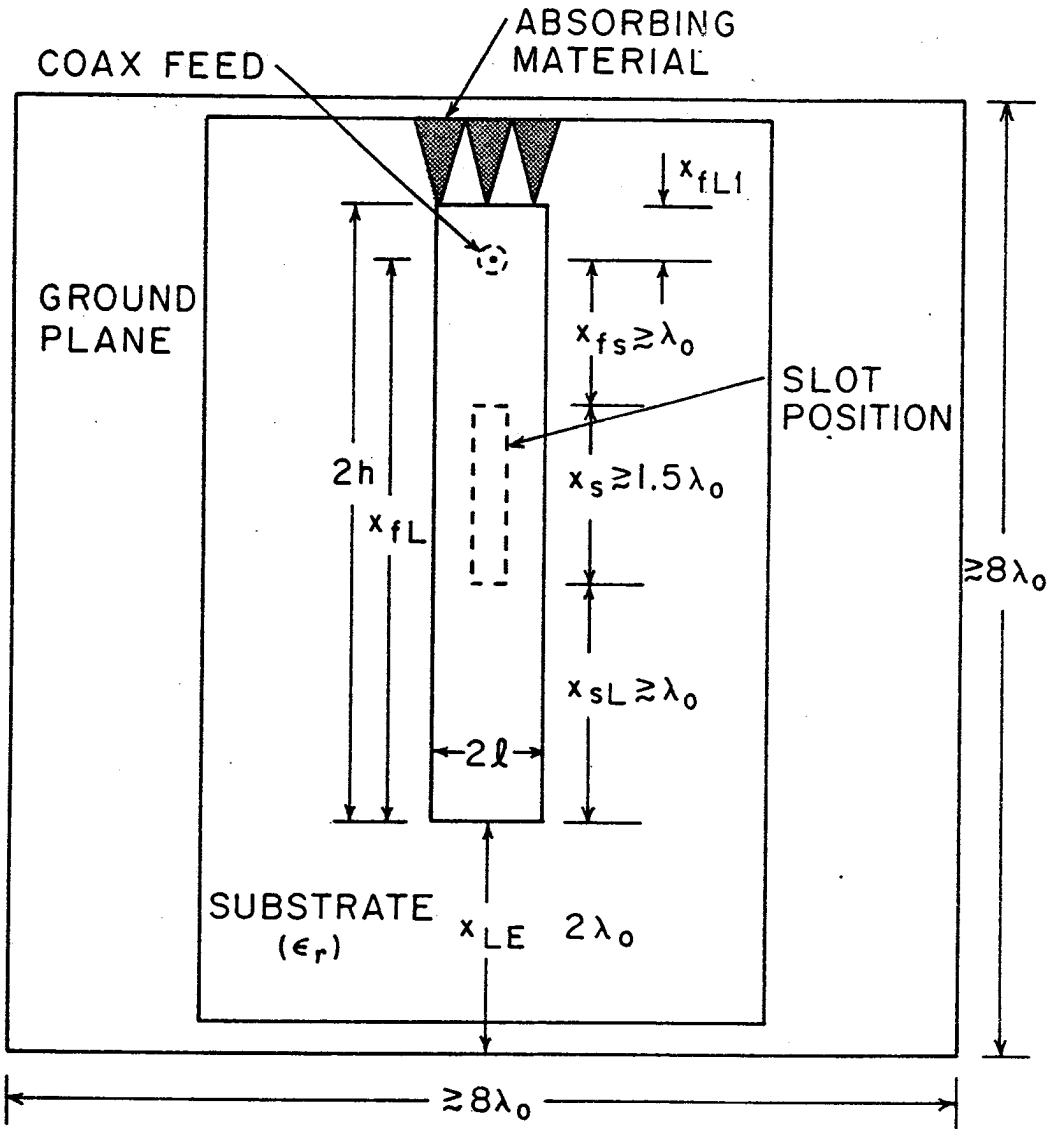
COAX FEED
ABSORBING MATERIAL
GROUND PLANE
x_{fL1}
$x_{fs} \gtrsim \lambda_o$
SLOT POSITION
2h
x_{fL}
$x_s \gtrsim 1.5\lambda_o$
$\gtrsim 8\lambda_o$
$x_{sL} \gtrsim \lambda_o$
2ℓ
SUBSTRATE (ϵ_r)
x_{LE}
$2\lambda_o$
$\gtrsim 8\lambda_o$

Fig. 4.5.

and a width 2ℓ. The width of the microstrip line is chosen so that only the fundamental mode propagates. The placement of the feed point and the slot are also indicated in this figure. It is seen that the distance x_{fs} between the feed and the slot is selected to be of the order of λ_o, the free space wavelength at the lowest operating frequency of the system. The distance $x_{fs} \gtrsim \lambda_o$ is chosen to allow the higher modes, produced by the feed, to decay, leaving only the fundamental mode to be measured in the slotted section. Similarly, the distance x from the open end to the slot is also $\gtrsim \lambda_o$ to ensure that the slotted region contains only the fundamental mode. For reasons which will be given later, the length of the slot has been chosen as $x_s \simeq 1.5\ \lambda_o$. Unlike any of the previous configurations, the microstrip line of Fig. 4.5 has a second open end at a distance x_{fL1} from the feed point. Since no measurements are to be made in this section of line, x_{fL1} can be made smaller. Thus, $x_{fL1} \gtrsim 0.5\ \lambda_o$. As seen in Fig. 4.5, this open end is loaded with absorbing material which has been included in order to reduce the amount of reflection. However, as will be explained, the absorbing material is not in principle necessary, but its use improves the performance of the measurement system. Up to this point, the ground plane length and width have been assumed to be infinite. Thus, the ground plane in the experiment should be made as large as possible in order to minimize the effects due to the ground plane edges. It is assumed that a ground plane length and width of approximately $8\lambda_o$ should be sufficiently large. Ideally, the substrate should cover the

entire ground plane in order to reduce field distortion produced by truncation. As will be seen, this may not be possible due to practical limitations. Finally, the distance x_{LE} between the unloaded open end and the ground plane edge is set at $x_{LE} \gtrsim 2\lambda_o$. Since the fields of a microstrip line are mainly confined to the region underneath the top conductor, the above choice of x_{LE} is assumed to be sufficient to avoid measurable edge effects.

4.5. The Transmission Line Representation Of the Slotted Ground Plane System

The system of Fig. 4.5 can be viewed as a coaxial line feeding two sections of microstrip line. One section is of length x_{fL1}, terminated by a load consisting of absorbing material. The other section of length x_{fL} is terminated by an open end. The fundamental modes that propagate both have the form of Eq. (2.31), although the reflection coefficient due to the end with the absorbing material differs from that of the open end. The microstrip line sections are, in general, dispersive; but at a single frequency, the field variation along the x axis is identical in form to the voltage variations along a conventional TEM transmission line. Until now, the analogy between the propagation of the fundamental mode down a microstrip line and the propagation of a voltage wave down a conventional TEM transmission line have not been precisely defined. Since E_{zo} is probed directly underneath the top conductor of the microstrip line, $E_{xo}|_{y=0}$ is assumed to be equivalent to a voltage wave V on a two-conductor TEM

transmission line. In terms of the geometry of Fig. 4.5 and Eq. (2.31), the electric field variation in each microstrip line section can be written as (the open end is at $x = 0$)

$$E_{zo}|_{y=0} = C_1 e^{jk_o\alpha_o x}\left(1 + \hat{\Gamma} e^{+j2k_o\alpha_o x}\right) \quad (-x_{fL} < x < 0) \tag{4.8}$$

$$= C_2 e^{jk_o\alpha_o x}\left(1 + \hat{\Gamma}_a e^{-j2k_o\alpha_o (x+x_{fL1}+x_{fL})}\right)$$

with

$$-(x_{fL1} + x_{fL}) < x < -x_{fL1} \quad .$$

In these equations, C_1 and C_2 are complex constants that depend on the modal excitation. Also $\hat{\Gamma}$ is the open end reflection coefficient. Since the absorbing material alters the fundamental mode reflection coefficient, $\hat{\Gamma}_A$ is introduced in the second equation to account for this effect. As will be seen, it is not necessary for this experiment to evaluate $\hat{\Gamma}_A$. Defining C_1' and C_2' as analogs of C_1 and C_2, the corresponding voltage equations for the system of Fig. 4.5 are

$$V = C_1' e^{-jk_o\alpha_o x}\left(1 + \hat{\Gamma} e^{j2k_o\alpha_o x}\right) \quad (-x_{fL} < x < 0) \tag{4.9}$$

$$= C_2' e^{jk_o\alpha_o (x+x_{fL}+x_{fL1})}\left(1 + \hat{\Gamma}_A e^{-j2k_o\alpha_o (x+x_{fL1}+x_{fL})}\right)$$

with

$$-(x_{fL1} + x_{fL}) < x < -x_{fL} \quad .$$

Based on Eq. (4.9), the system of Fig. 4.5 can be represented by the equivalent transmission line representation of Fig. 4.6a. In this figure, the characteristic impedances of the transmission line sections are assumed to be unity while the source and load impedances are normalized. The impedance $\hat{z}$ represents the impedance of the open end, and it is defined in terms of the reflection coefficient as

$$\hat{z} = \frac{1}{\hat{y}} = \frac{1 + \hat{\Gamma}}{1 - \hat{\Gamma}} \quad .$$

It is $\hat{z}$ or equivalently $\hat{y}$ that is to be calculated from the field measurements. The impedance $\hat{z}$ is connected to the source through a transmission line section of length x_{fL}. In terms of the actual system, this line represents the section of microstrip between the feed point and the open end. The source and the coaxial feed are represented by the voltage generator $\hat{V}_g$ and the normalized impedance $\hat{z}_g$. $\hat{z}_A$ is the normalized impedance of the end that is loaded with absorbing material. Now, $\hat{z}_A$ is connected to the feed through a section of length x_{fL1} of transmission line. Physically this represents the section of microstrip line that is terminated with absorbing material. Since it is not desired to perform measurements in this section of line, the impedance $\hat{z}_A$ can be transformed to the load by means of the conventional transmission line equations, as is shown in Fig. 4.6b. The wave number of the fundamental mode is $k_o \alpha_o$, so the transformed impedance for a lossless line is given by [20]

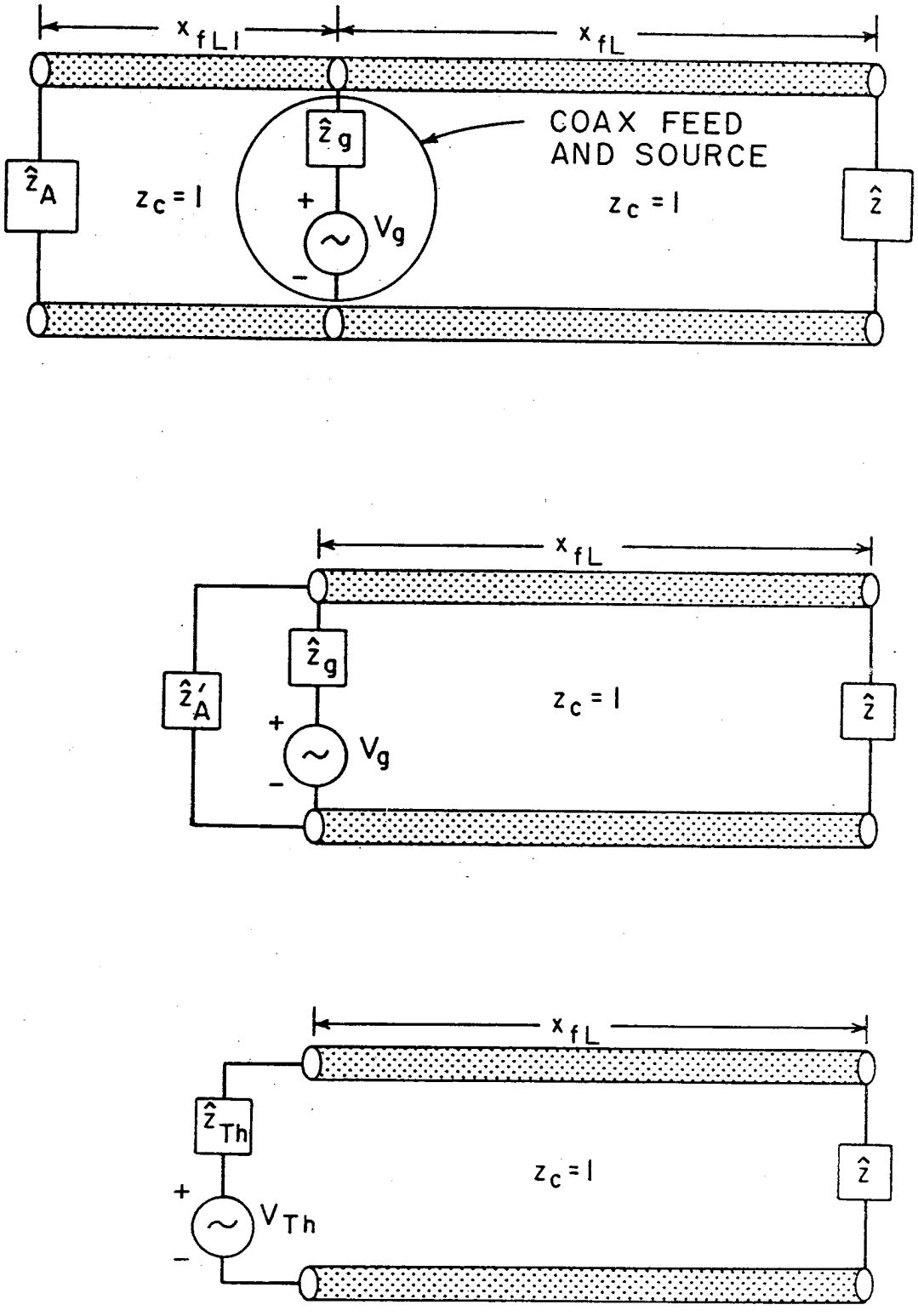
x_{fL1}
x_{fL}
$\hat{z}_g$
COAX FEED
AND SOURCE
$\hat{z}_A$
$z_c = 1$
+
V_g
−
$z_c = 1$
$\hat{z}$
x_{fL}
$\hat{z}_g$
$\hat{z}'_A$
$z_c = 1$
$\hat{z}$
+
V_g
−
x_{fL}
$\hat{z}_{Th}$
$z_c = 1$
$\hat{z}$
+
V_{Th}
−

Fig. 4.6.

$$z'_A = \frac{\hat{z}_A + j \tan k_o \alpha_o x_{fL1}}{1 - j\hat{z}_A \tan k_o \alpha_o x_{fL1}} \quad .$$

Utilizing a result from network theory [19], the combination of z'_A in parallel with the source can be simplified to the configuration of Fig. 4.6c by means of Thévenin's theorem. The relationship between the voltages and impedances of Fig. 4.6c are

$$z_{Th} = \frac{\hat{z}'_A \, \hat{z}_g}{z_A + z_g} \tag{4.10}$$

$$V_{Th} = \frac{\hat{V}_g \, z'_A}{\hat{z}_g + \hat{z}_A} \quad . \tag{4.11}$$

Thus, the microstrip section of Fig. 4.5 can be represented in terms of the transmission line configuration of Fig. 4.6c. This is significant because the method of determining an unknown load impedance using slotted line measurements on the configuration of Fig. 4.6c is well known and straightforward. The details of the actual process by which the open end impedance (or admittance) is calculated from slotted line measurements is deferred until a later section.

It should be noted that $\hat{z}_a$ governs the values of V_{Th} and $\hat{z}_{Th}$ as an inspection of Eqs. (4.10) and (4.11) reveals. Referring to Fig. 4.6c, it is well known that the transmission line termination $\hat{z}$ (or $\hat{y}$) determines the form of the transmission line fields, and V_{Th} and $\hat{z}_{Th}$ affect how strongly the transmission line fields are excited. In terms of the actual physical system,

the form of the field due to the fundamental mode is governed only by the nature of the open end. Thus, the location of the coaxial feed along with the configuration of the line section that is loaded with the absorbing material determine only how strongly the fundamental mode is excited in the slotted section.

Thus, the measurement procedure is, in principle, independent of V_{Th} and $\hat{z}_{Th}$ and, therefore, also independent of the feed location and the section of microstrip line with the absorbing material load. However, because of noise limitations inherent in the measurement system, $\hat{V}_{Th}$ and $\hat{z}_{Th}$ should have values that result in a strong field excitation of the microstrip line section that contains the slot. It was observed experimentally that the use of absorbing materials produced strong microstrip fields over a broad range of frequencies. Without the absorber, strong signals were produced at only a few specific frequencies. Thus, the use of an absorbing load produces a better match ($\hat{z}_A$ is closer to 1), and a more desirable frequency characteristic results. Without the absorbing material present, one can alternatively view the microstrip line of Fig. 4.5 as being a high-Q resonant cavity in which strong signals appear at the resonant frequencies and weak signals occur at the remaining frequencies on account of destructive interference. The addition of the absorber, therefore, makes the system of Fig. 4.5 behave more like a semi-infinite transmission line, which has a smooth broadband frequency behavior. Since the generator impedance along with the effects of the absorbing material are not precisely known, no further analysis

regarding these quantities is carried out. Also, for the purposes of the experiment, no further analysis is necessary.

4.6. The Slotted Ground Plane Construction

This section deals with the implementation of the slotted ground plane system of Fig. 4.5 along with the associated substrates and top conductors. Of fundamental concern in the system design is how accurately it enables one to determine the admittance of the microstrip open end. The system accuracy, in turn, is determined by the frequency of operation along with the mechanical tolerances and distance measurement limitations. In designing the actual ground plane system, it was decided that being able to resolve distances on the order of 1/1000 wavelength would be sufficient to obtain accurate end admittance information. A 10^{-3} wavelength resolution should allow the phase of the open end reflection coefficient to be measured to within 1° ($\varepsilon_r = 1$) if the effects of the slot and the probe are not considered. What does this resolution mean in terms of an operating frequency? If, for instance, the operating frequency is chosen to be 10 GHz, the distance resolution as well as the tolerance on the slotted section must be on the order of 0.03 mm (less than 1/1000"). This requirement, in terms of available machining facilities and distance measurement techniques is quite difficult to meet. On the other hand, a frequency of 1 GHz produces a 0.3 mm tolerance requirement, which is much more easily met. Thus, as the operating frequency decreases, the tolerance requirements become

less stringent. However, since the system dimensions are based on free space wavelength at the lowest operating frequency, the overall dimensional requirements must increase as the operating frequency decreases. An operating frequency that is too low requires a large and cumbersome ground plane arrangement. Even if the system could be made very large in size, the measurement accuracy would improve only marginally since there are errors introduced by factors other than the distance measurement accuracy and the mechanical tolerances.

On the basis of these considerations as well as the availability of equipment, the ground plane system was designed to operate at a minimum frequency of 1 GHz, which corresponds to a free space wavelength of 33 cm (≃ 1'). It was concluded that operation in the 1 GHz range would result in a relatively simple construction of the slotted ground plane while providing sufficient accuracy to investigate the behavior of the end admittance. The critical dimensions of the actual ground plane that was constructed are based on those of Fig. 4.5 with λ_o = 33 cm (1').

The ground plane constructed for the experiment is shown in Fig. 4.7. As can be seen from this figure, the ground plane, with overall dimensions of 8' × 8' consists of two 8' × 4' × $\frac{1}{8}$" aluminum sheets and an 18" × 8½" slotted center piece. The three piece arrangement is necessary for two main reasons. First, the largest available width in the desired grade of aluminum is only 4', so two of these sheets are required. Finally, the section that contains the slot requires a precision which can be

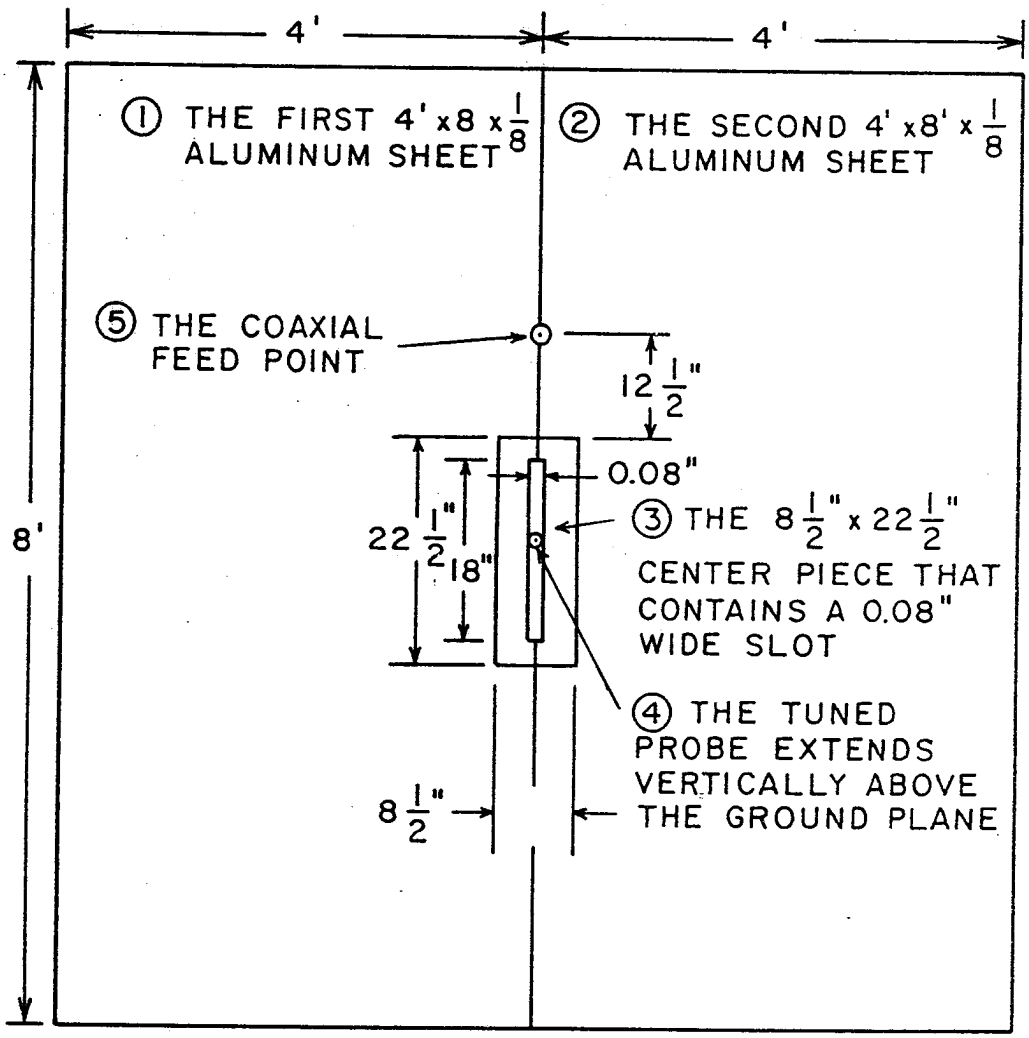
4'
4'
8'
① THE FIRST 4' x 8' x 1/8 ALUMINUM SHEET
② THE SECOND 4' x 8' x 1/8 ALUMINUM SHEET
⑤ THE COAXIAL FEED POINT
12 1/2"
0.08"
22 1/2"
18"
③ THE 8 1/2" x 22 1/2" CENTER PIECE THAT CONTAINS A 0.08" WIDE SLOT
④ THE TUNED PROBE EXTENDS VERTICALLY ABOVE THE GROUND PLANE
8 1/2"

Fig. 4.7.

accomplished only on a smaller, separate section of metal stock, considerably smaller than 4' × 8'. The slotted section, therefore, has overall dimensions of 18" × 10". In order to provide a smooth and level surface, the two large aluminum sheets are fastened to two 8' × 4' × $\frac{3"}{4}$ pieces of particle board by means of flush-mounted wood screws. The entire ground plane, in turn, rests on top of a 15' × 9' platform. Access to the center piece as well as the coax feed was gained from underneath the platform. The three-piece construction of the ground plane resulted in small gaps along the lines where the three pieces fit together. In order to avoid field distortion due to the interruption of the surface current flow, the gaps were bridged by a thin, aluminum conducting tape permitting currents to flow through its adhesive surface. A photograph of the top of the ground plane is shown in Fig. 4.8.

A top view of the center piece is shown in Fig. 4.9. The top of the center piece consists of two 5" × 24" × ¼" aluminum sheets with a precision machined 0.08" (2 mm) slot cut along the axis where the two plates fit together. This two-piece construction allows the slot to be more accurately cut. The slotted section is fastened to the ground plane by means of flush-mounted screws and the step arrangement of Fig. 4.10. The step construction allows the center piece to be removed from below the ground plane to simplify the required periodic adjustments and cleaning. A photograph of the center piece, as viewed from underneath the ground plane is shown in Fig. 4.11. Referring to this photograph, the assembly with coaxial cable extending out from it is a tunable

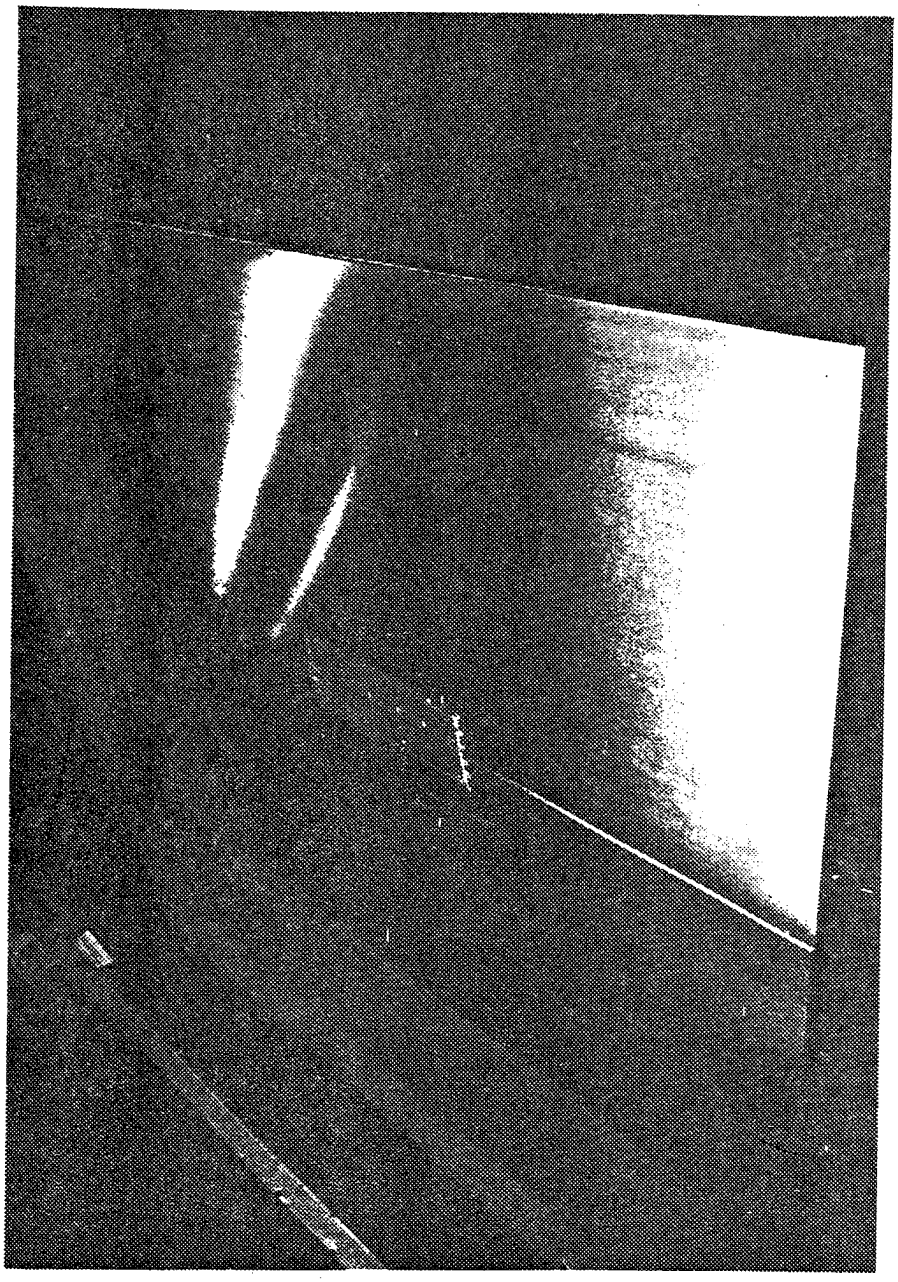

Fig. 4.8.

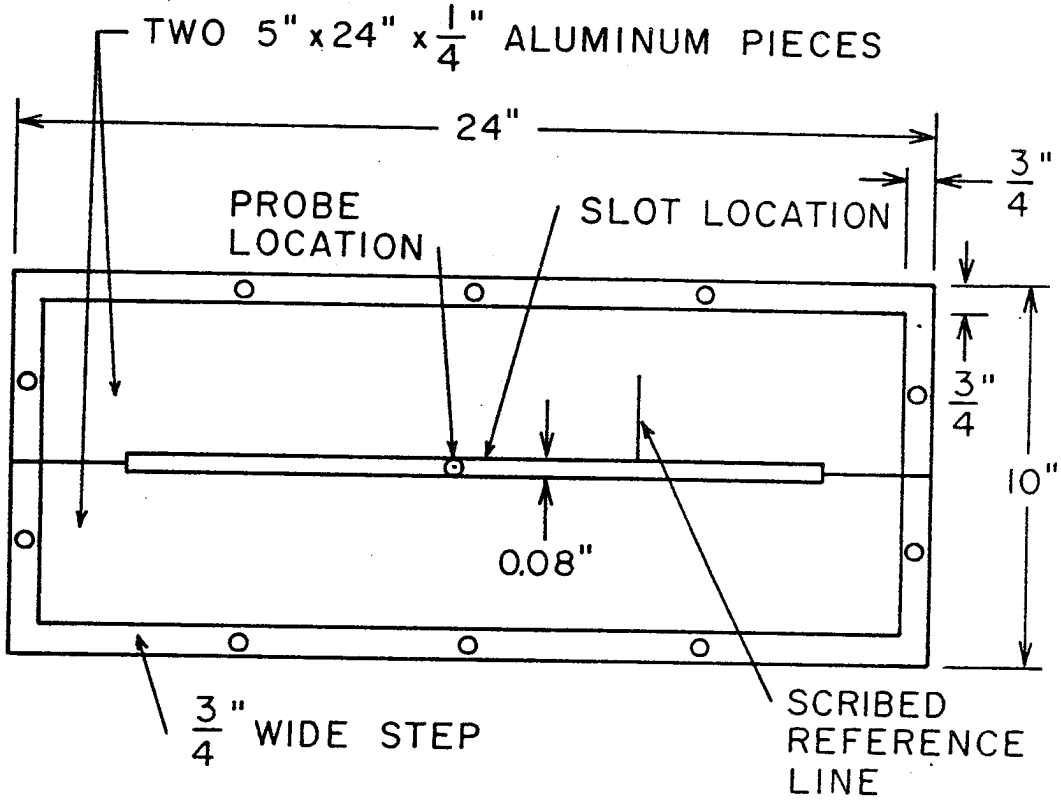
TWO 5" x 24" x 1/4" ALUMINUM PIECES
24"
3/4"
PROBE LOCATION
SLOT LOCATION
3/4"
10"
0.08"
3/4" WIDE STEP
SCRIBED REFERENCE LINE

Fig. 4.9.

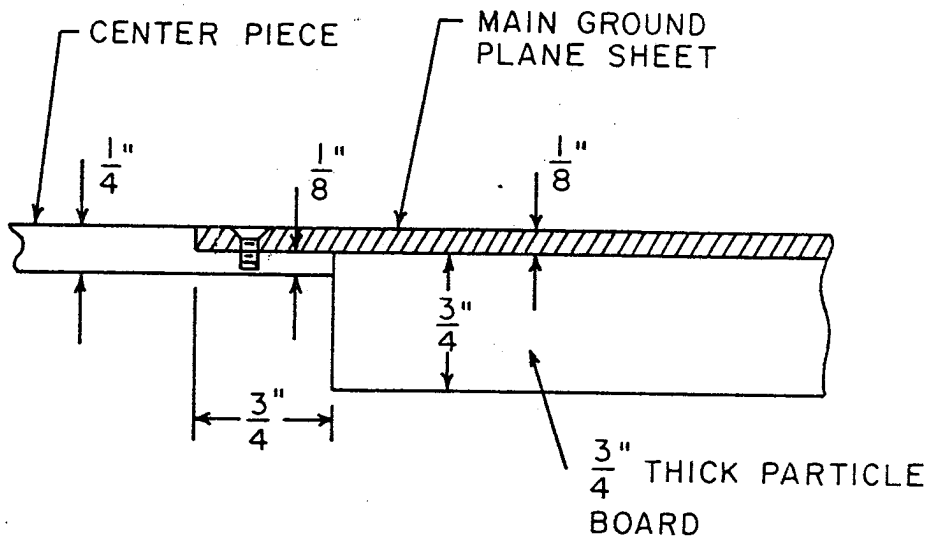
CENTER PIECE
MAIN GROUND PLANE SHEET
1/4"
1/8"
1/8"
3/4"
3/4"
3/4" THICK PARTICLE BOARD

Fig. 4.10.

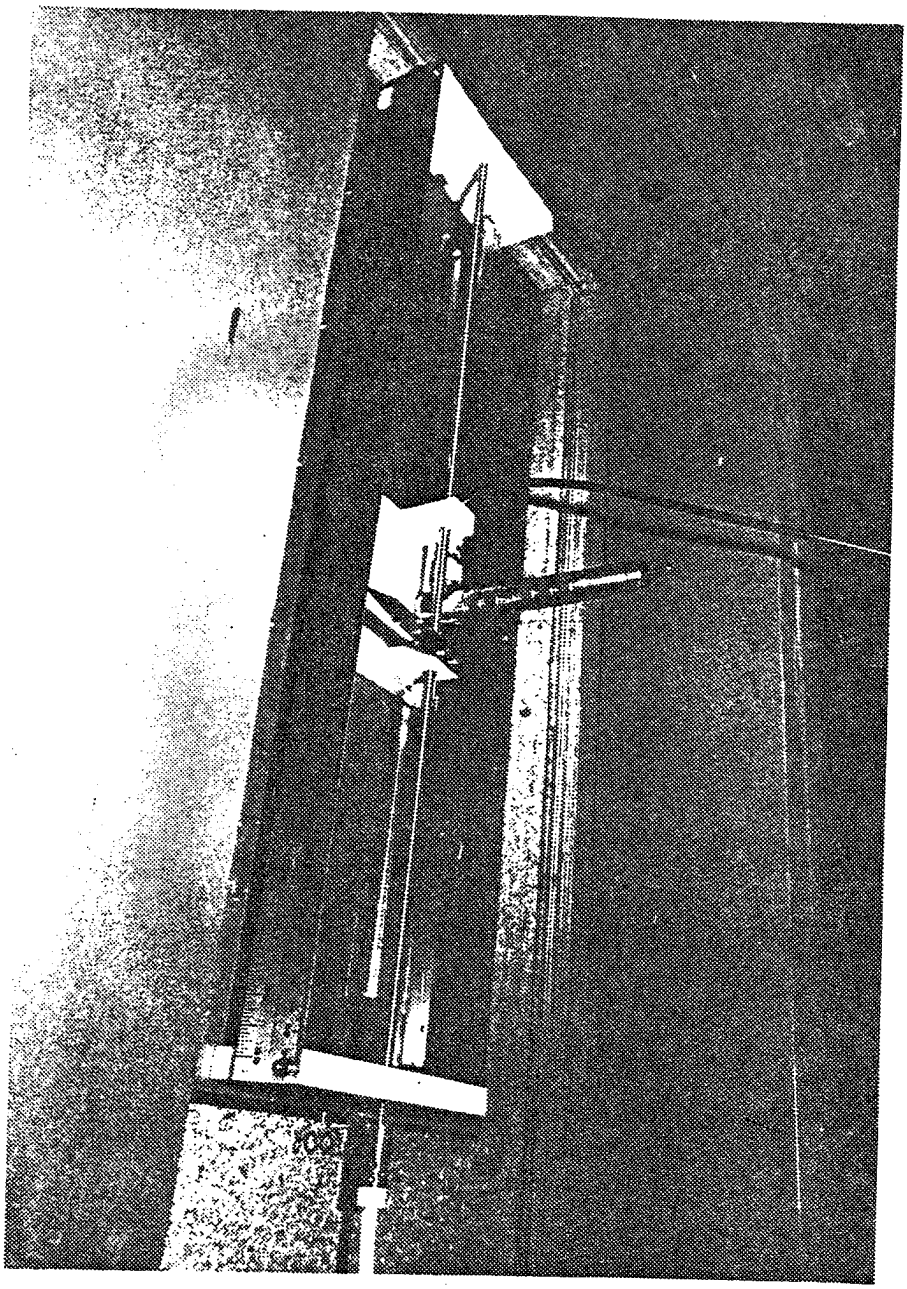

Fig. 4.11.

E-field probe, which, in turn, is mounted to a movable teflon carriage. The probe carriage is guided by two aluminum tracks, and it is attached to a rotatable threaded shaft by means of two teflon blocks with threaded holes. The teflon shaft bearings, located at both ends of the center piece bottom also hold the two 5" × 24" × ¼" aluminum plates together. More details of the probe mount assembly are shown in Fig. 4.12. The threaded shaft is turned by means of simple hand crank assembly (see Fig. 4.11), one shaft revolution resulting in 1.5 mm of probe carriage travel. Displacements of the probe along the length of the slot are measured using a pointer in conjunction with a metric scale that allows distances to be resolved to the nearest 0.2 mm. Thus, the probe mount and drive make it possible to place the probe precisely at a desired position along the slot. Referring to Fig. 4.9 once again, a reference line has been scribed on the top surface of the center piece perpendicular to the slot axis. When the probe wire is aligned with the reference line, the indicator scale reading, denoted by S_{ref}, must be noted. As is discussed in the next section, S_{ref} along with the distance from the reference line to the open end of the microstrip line must be known in order to calculate the open end admittance from slot measurements.

4.7. Substrate Preparation

In order to obtain a sufficient amount of admittance data, a number of different substrate and top conductor combinations were employed. The most extensive data were obtained using substrates

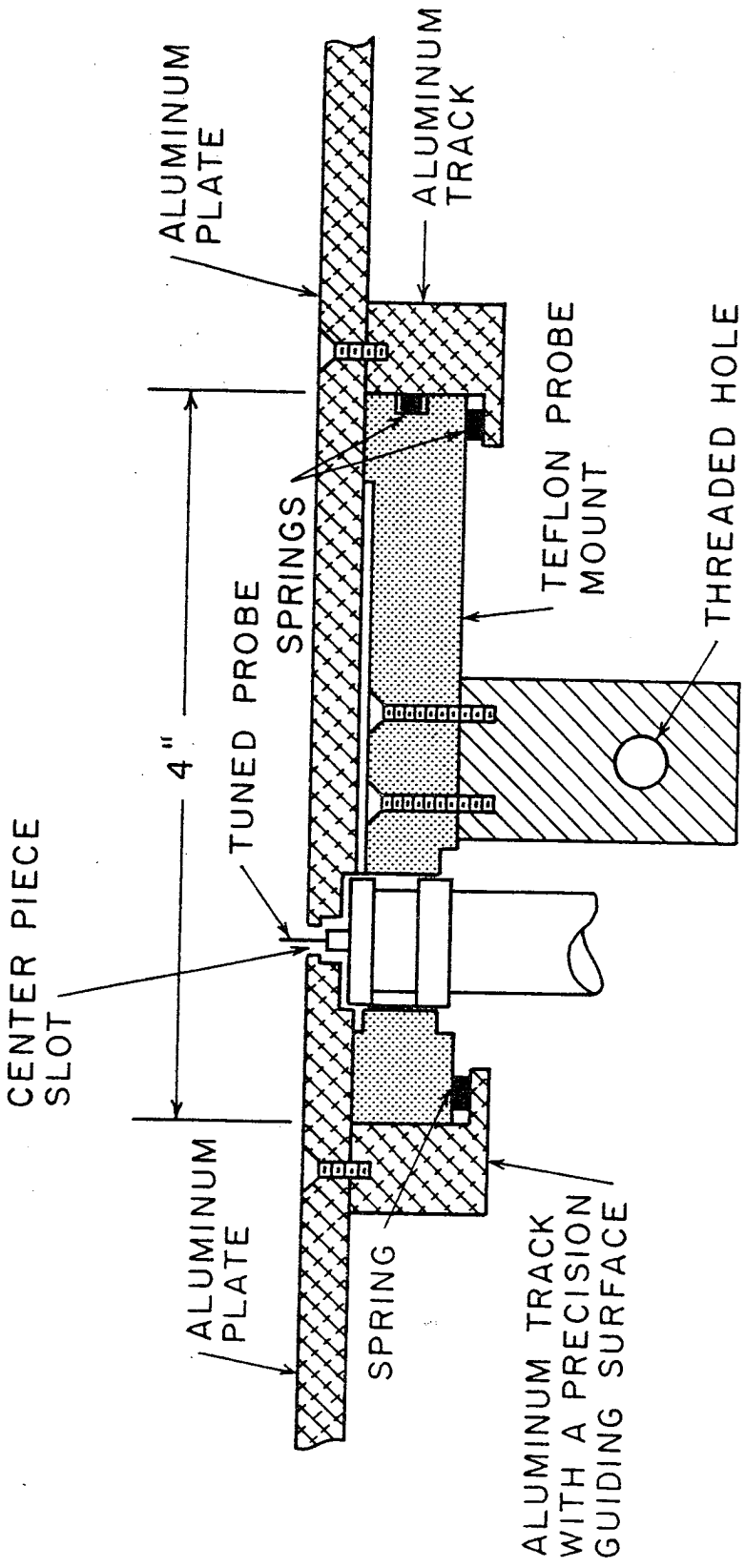
ALUMINUM PLATE
ALUMINUM TRACK
TEFLON PROBE MOUNT
THREADED HOLE
SPRINGS
4"
TUNED PROBE
CENTER PIECE SLOT
ALUMINUM PLATE
SPRING
ALUMINUM TRACK WITH A PRECISION GUIDING SURFACE

Fig. 4.12.

of foamed dielectric material which possesses a dielectric constant close to that of air. Two different foamed dielectric materials were used: beadboard (foamed polystyrene) and ethylfoam (foamed polyethylene). Both of these materials have dielectric constants in the range $1.01 \leq \varepsilon_r \leq 1.03$. The foamed substrates were used to support the copper top conductor 0.02" (0.5 mm) thick. Two different foamed dielectric support configurations were employed. The first consisted of a solid 2' × 6' sheet of beadboard 9 mm thick to support the top conductor. A narrow slot was cut in the bottom of the beadboard to accommodate the probe. Two small holes were drilled in the material for the purposes of aligning the top conductor with respect to the slot and providing visual access to the reference line on the center piece surface. A photograph of the solid beadboard substrate with a 6" wide top conductor is shown in Fig. 4.13. The second support configuration is shown in Fig. 4.14 and Fig. 4.15. Instead of using a solid substrate, a bridge-type support arrangement was employed with substrate thicknesses of 6.5 mm and 9 mm. Top conductors (0.5 mm thick) with widths of 3" (76.8 mm), 4.5" (115.2 mm), and 6" (153.6 mm) were used in the foamed dielectric substrate case. The length of each of these conductors was 60" (1.54 m).

Another series of measurements was performed on a 2' × 6' polycarbonate substrate 9.2 mm thick. The electrical characteristics of polycarbonate are dealt with in the next section; but for now, it is sufficient to note that the dielectric constant of this material is 2.82 in the 1 GHz frequency range. Polycarbonate

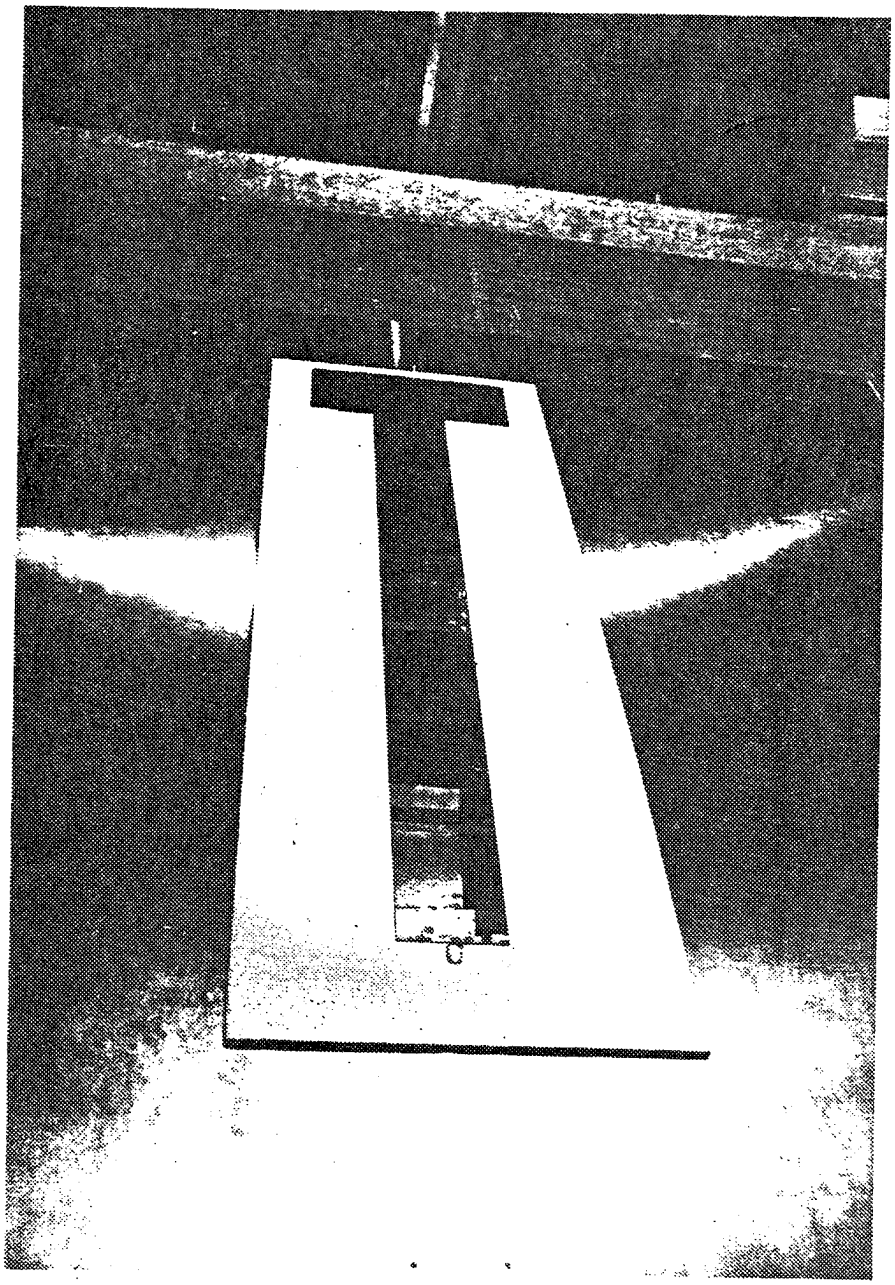

Fig. 4.13.

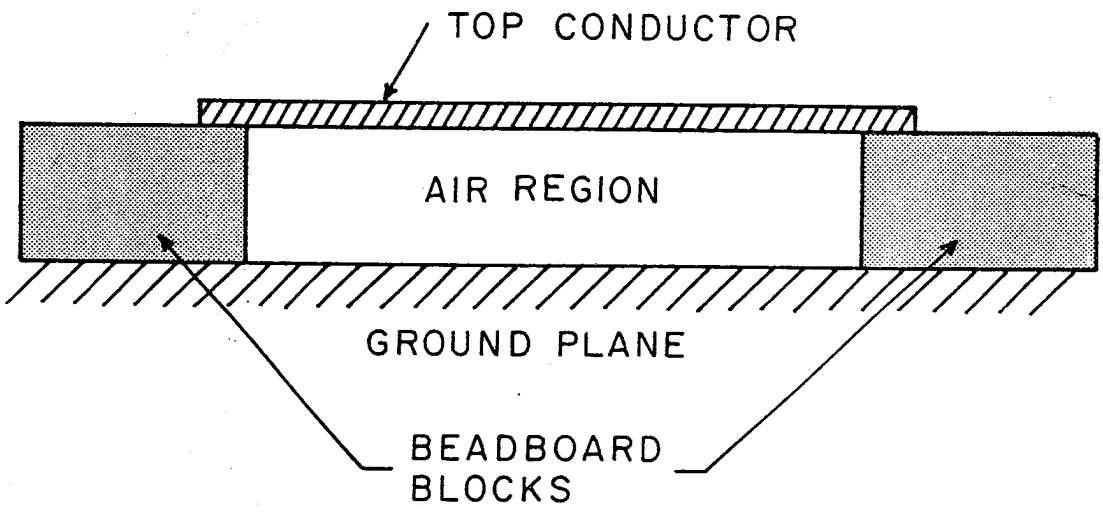

Fig. 4.14.

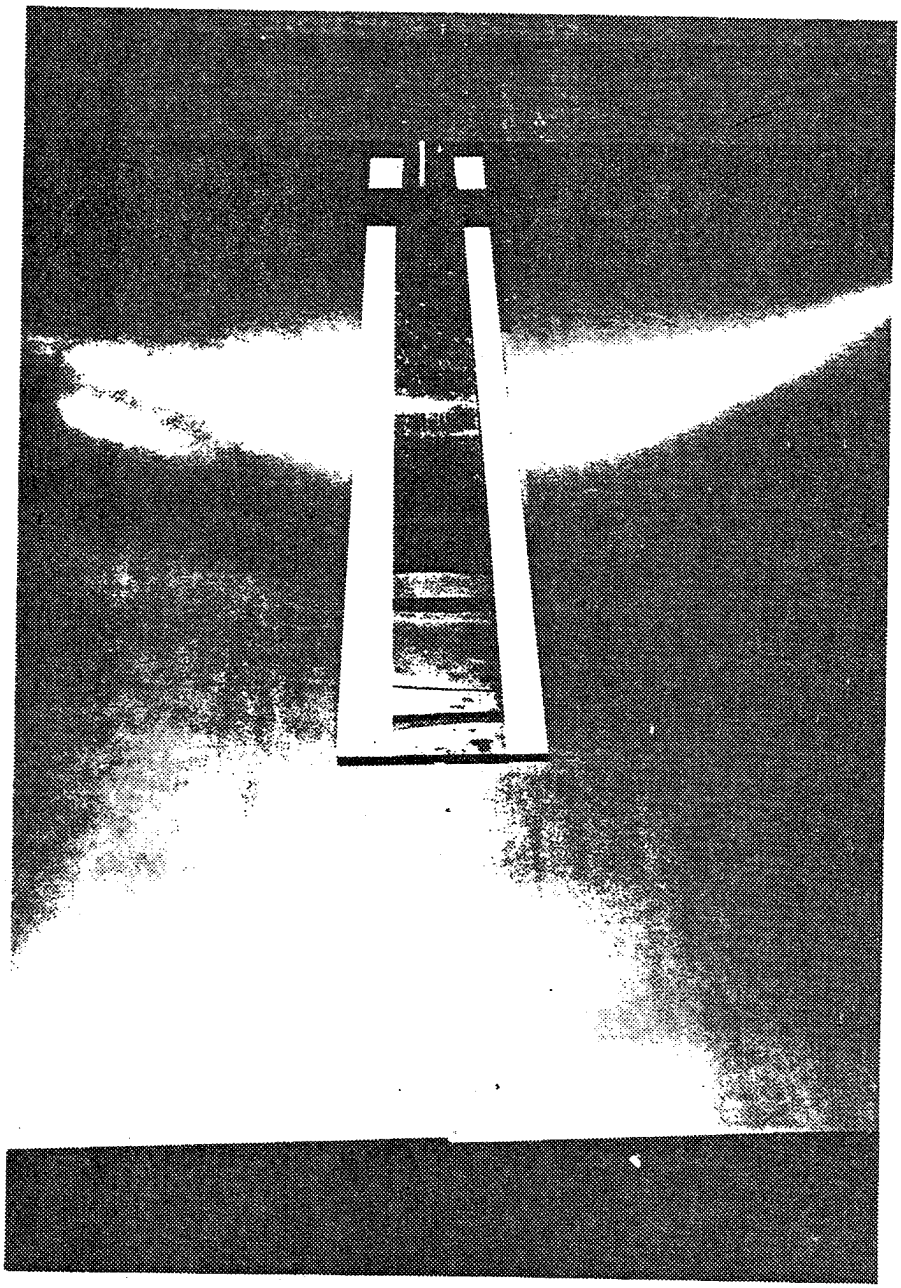

Fig. 4.15.

is a rigid and tough material, so in order to allow for probe penetration into this material, a 0.08" (2 mm) × 18' slot, to permit a 1.5 mm probe penetration, was milled into the bottom of the substrate material, as is shown in Fig. 4.16. The top conductor consisted of a 4' long section of 2" (52.6 mm) wide aluminum adhesive tape approximately 0.1 mm thick. Because of its mechanical properties, the polycarbonate substrate did not rest perfectly flat on the ground plane surface, which resulted in air pockets of roughly 0.1 to 0.3 mm thickness between the dielectric and the ground plane. Being an electrically dense material, it was found that these air pockets resulted in inconsistent susceptance (phase) data that did not vary in any definite manner as a function of frequency. To alleviate this problem, an 8½" wide portion of the substrate bottom was covered with the same 2" wide adhesive aluminum tape that was used for the top conductor. The taped region is shown in Fig. 4.16. The tape was applied in four strips running parallel to the slot, and small gaps were left between each of these strips. One-half inch wide aluminum tape, which has a conducting path through its adhesive, was applied along the entire length of these gaps to form a conducting strip 8½" wide. As will be seen in the next chapter, the taping of the substrate bottom produces susceptance data that vary fairly smoothly as a function of frequency. A photograph of the taped polycarbonate substrate is shown in Fig. 4.17.

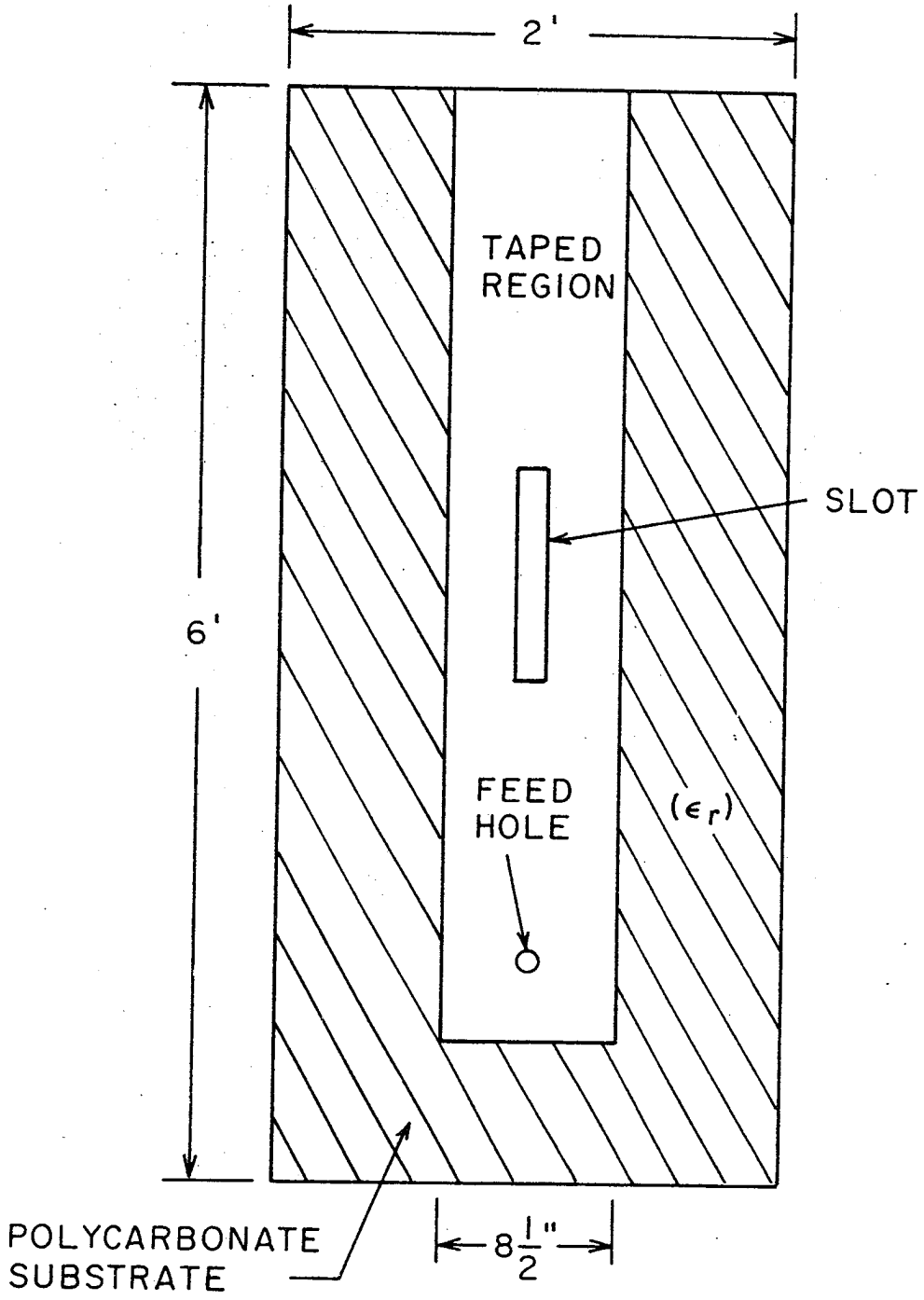
2'
TAPED
REGION
SLOT
6'
FEED
HOLE
(ϵ_r)
POLYCARBONATE
SUBSTRATE
$8\frac{1}{2}$"

Fig. 4.16.

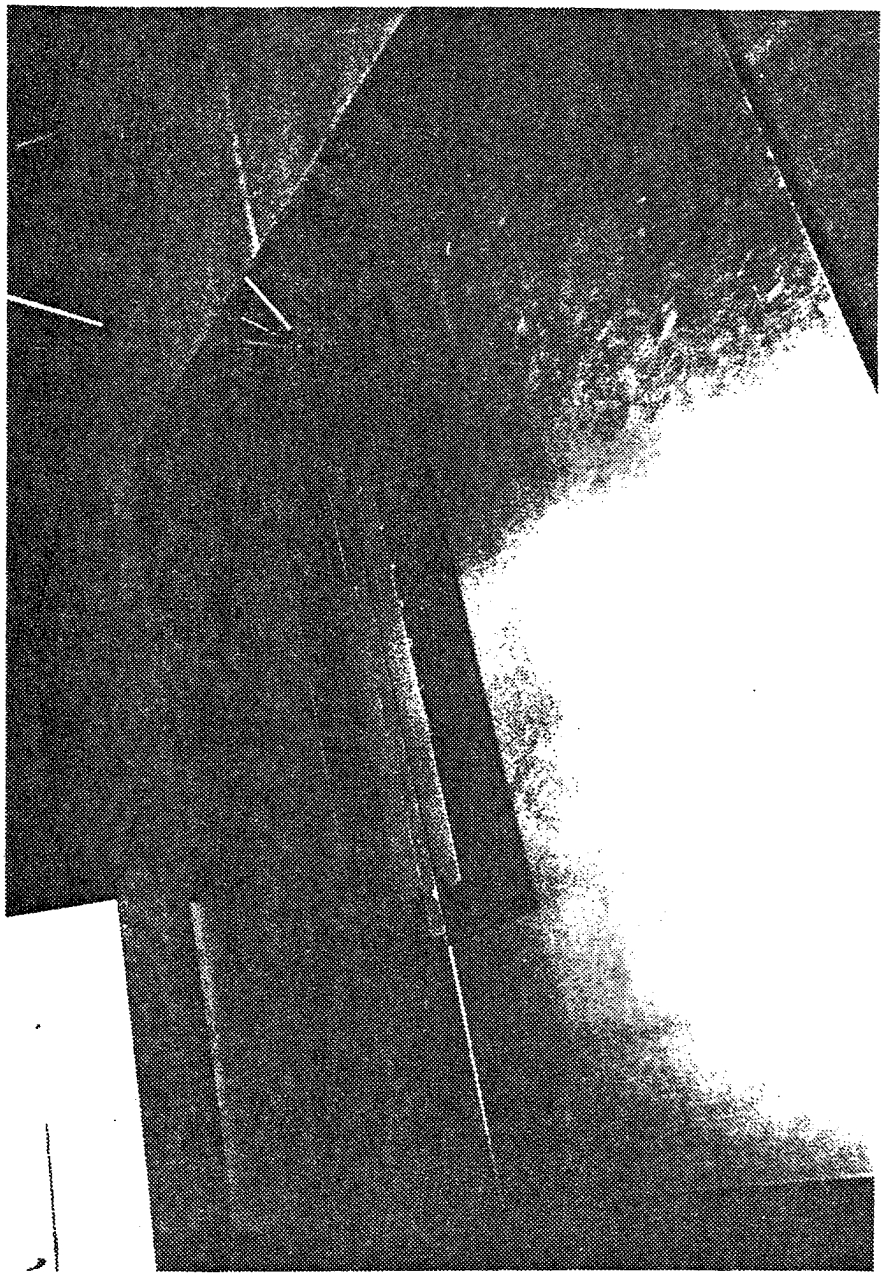

Fig. 4.17.

4.8. Coax Feed Construction

In order to launch energy into the microstrip line, the coaxial feed of Fig. 4.18 was used. Basically, the feed consisted of a coaxial connector, a spacer, and a short section of $\frac{1}{16}$" bronze rod. The connector was attached to the ground plane by means of the spacer and the associated flush-mounted screws. The spacer was a 1" × 1" × 1" aluminum block with a $\frac{5}{8}$" hole drilled through its center to accommodate the coaxial connector. Four smaller holes were drilled through the spacer in order to accept the four flush-mounted screws. The center conductor of the coax feed made contact with the top conductor by means of a short section of $\frac{1}{16}$" diameter bronze rod that protrudes through a $\frac{1}{4}$" diameter hole in the ground plane and a $\frac{5}{64}$" diameter hole in the microstrip top conductor. Good contact between the bronze rod and the top conductor was ensured by means of a piece of conducting tape, placed as in Fig. 4.18.

4.9. Instrumentation

A photograph of the instrumentation associated with the microstrip slotted line system is located in Fig. 4.19. The components associated with the feed system are shown in the block diagram of Fig. 4.20a. The RF energy was produced by a General Radio unit oscillator which utilizes a loop-coupled cavity. The type 1216A was used in the 0.9-2.1 GHz frequency range, and the type 1209 was used to cover the 800-900 MHz range. The rated

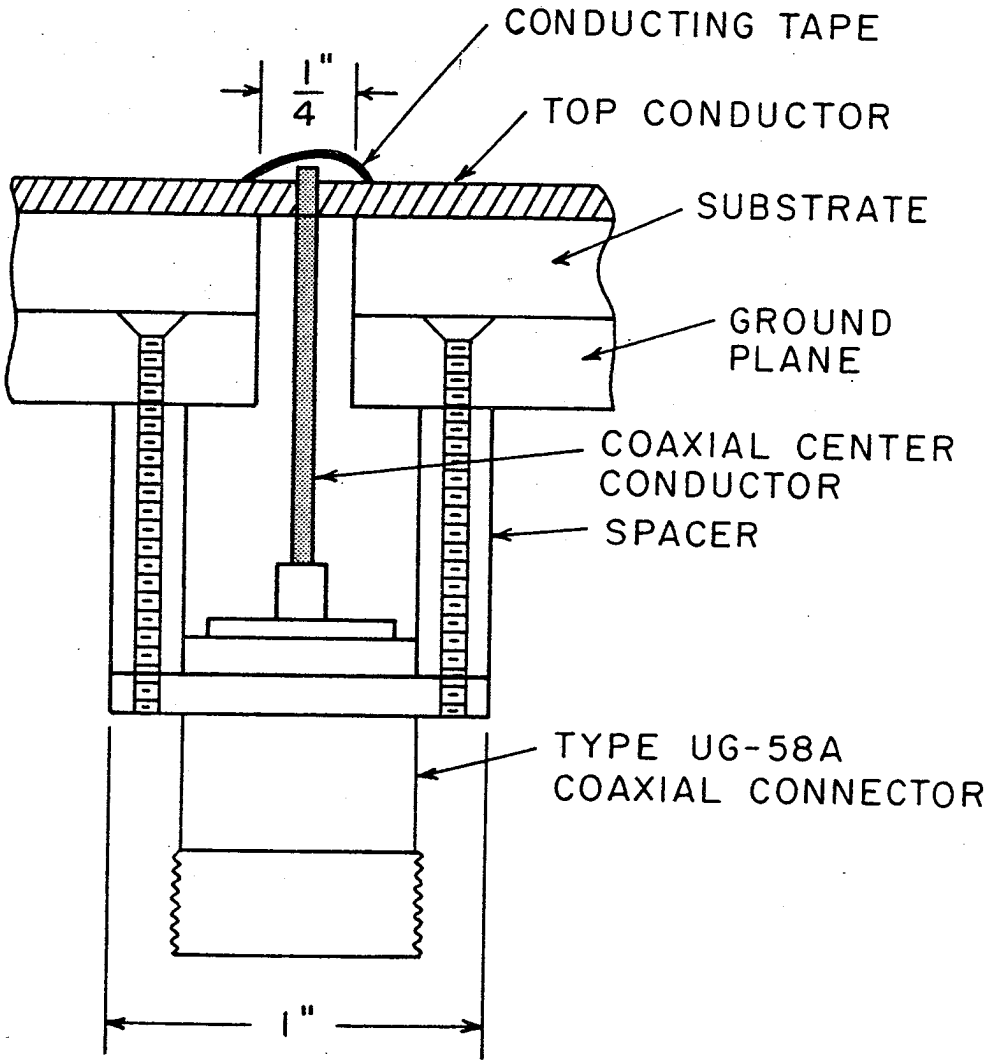
CONDUCTING TAPE
1"
4
TOP CONDUCTOR
SUBSTRATE
GROUND
PLANE
COAXIAL CENTER
CONDUCTOR
SPACER
TYPE UG-58A
COAXIAL CONNECTOR
1"

Fig. 4.18.

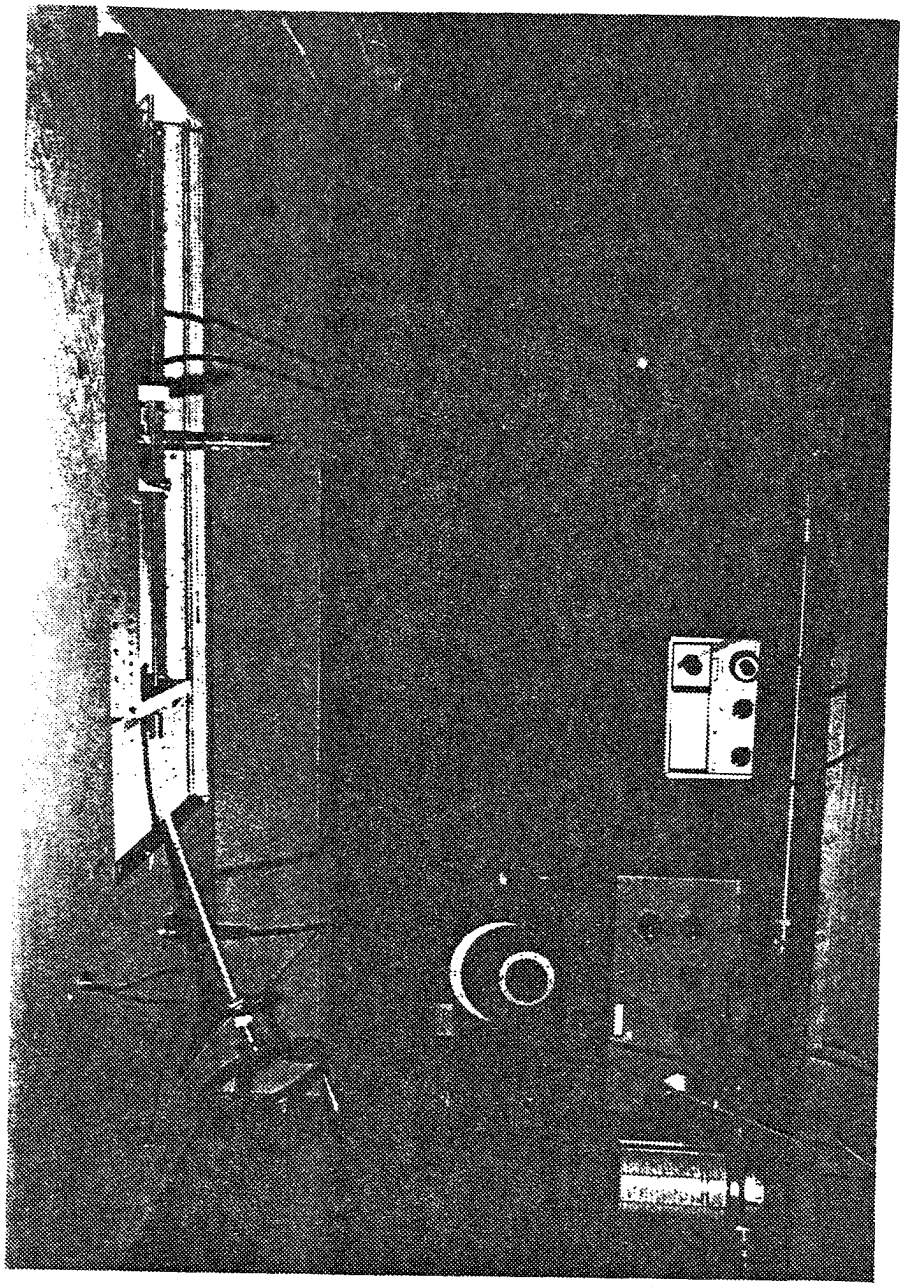

Fig. 4.19.

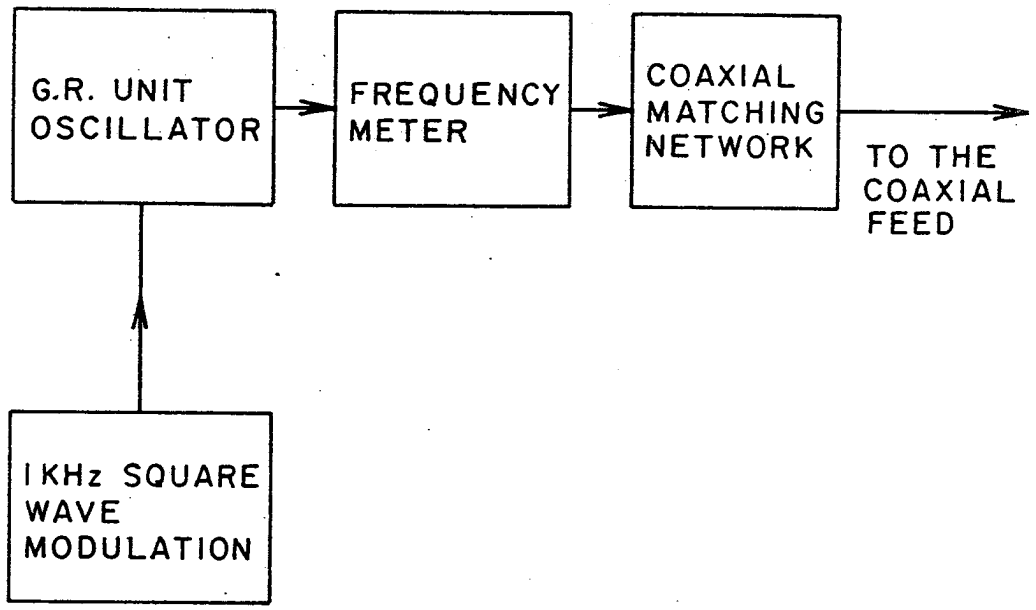
G.R. UNIT OSCILLATOR
FREQUENCY METER
COAXIAL MATCHING NETWORK
TO THE COAXIAL FEED
1KHz SQUARE WAVE MODULATION

(a)

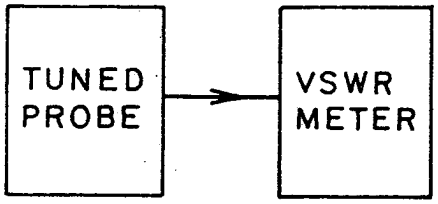
TUNED PROBE
VSWR METER

(b)

Fig. 4.20.

outputs of these generators is anywhere from 150 mW to 400 mW, depending on which frequency is selected. For the purpose of signal detection, the source was modulated by a 1 kHz square wave, which was produced by an HP-211A square wave generator. The output frequency of the source was monitored by either an HP-5342A frequency counter with a resolution of 1 Hz or an HP-536A frequency cavity with a 1 MHz resolution. In order to couple sufficient power into the microstrip line, the signal generator was connected into a matching network consisting of a variable length coaxial air line and a shunt connected sliding short. It was found necessary to adjust the matching network for each source frequency until a signal of sufficient strength to permit measurements appeared. The output of the matching network, in turn, was connected to the coaxial feed.

A block diagram of the probing arrangement employed is illustrated in Fig. 4.20b. The microstrip electric field was explored by means of a PRD-250 tuned probe which was mounted in the probe carriage. It was found necessary to use a tuned probe in order to provide measurable signal levels. The lowest operating frequency of the probe was found to be 800 MHz, which prevented any investigation below this frequency. The PRD-250 probe assembly contains a type 1N23 crystal detector that demodulates the square-wave modulated signal picked up by the E-field probe. The detector output was fed into an HP-415E standing wave meter, which is merely an audio-frequency A.C. voltmeter, calibrated to read SWR values. Assuming that the crystal detector characteristic obeys a square-

law relation, the HP-415E SWR scale permits the direct reading of relative electric field amplitudes. This, of course, is contingent on the crystal input power being at a low enough level to ensure that the crystal does, in fact, operate in the square-law region.

Now the input circuit of the HP-415E SWR indicator contains a variable gain amplifier that can be controlled in 10 dB steps from 0 dB to 60 dB. With the gain switch set at 40 dB and the gain vernier control adjusted to nearly a maximum, it was found that the SWR scale permitted a direct reading of relative electric field strengths. This range was selected because the signals which appeared were still well above the noise; and, as will be seen, the incident power on the crystal was still low enough to ensure a square-law characteristic. If a signal appeared that was too large to be read in this meter range, the probe was detuned until the signal was reduced to the appropriate level. For all of the experimental measurements, the gain setting of 40 dB was maintained.

In order to prove that the crystal was, in fact, operating in the square-law region on the 40 dB setting, an HP-413b power meter and a variable coaxial attenuator were added to the feed network as is shown in Fig. 4.21. The coaxial attenuator was a General Radio type GR-74A which allowed the power to the feed to be varied continuously over a large range. The HP-431b power meter utilizes a thermistor as a sensing element, and it was attached to the feed network by means of a 20 dB directional coupler. At frequencies of $f = 0.9, 1.1, 1.3, 1.5, 1.7$, and

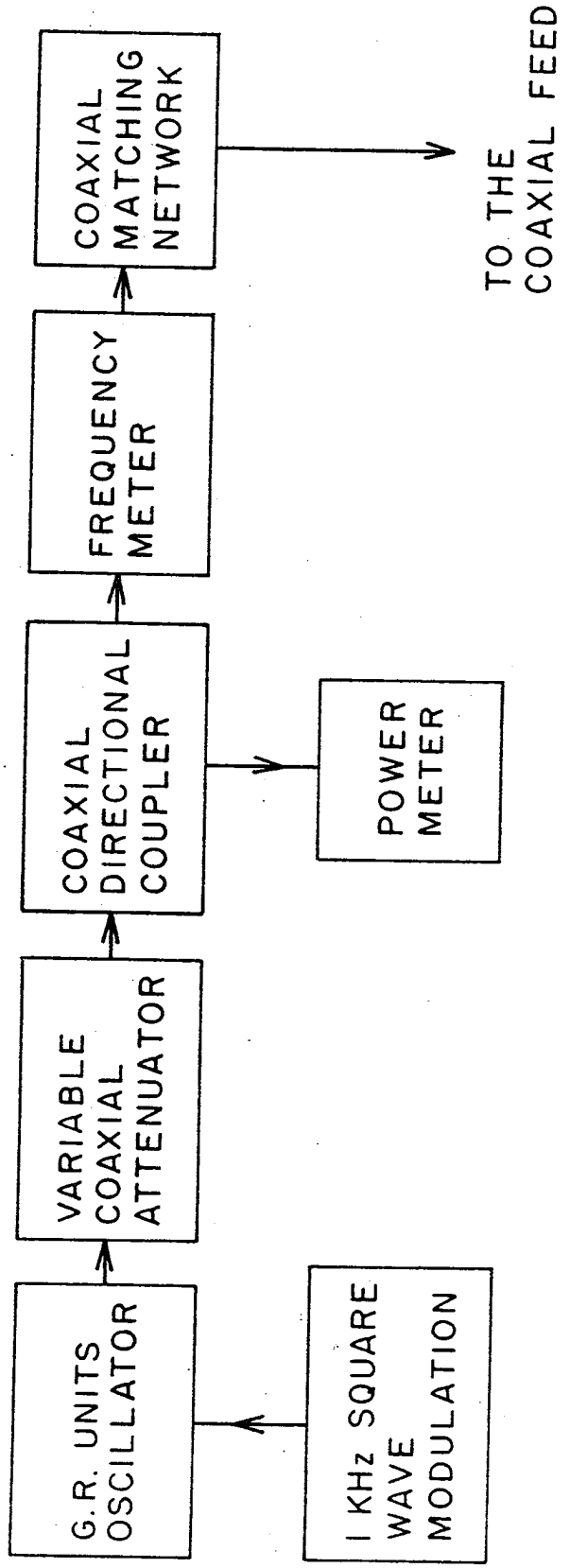
G.R. UNITS OSCILLATOR
1 KHz SQUARE WAVE MODULATION
VARIABLE COAXIAL ATTENUATOR
COAXIAL DIRECTIONAL COUPLER
POWER METER
FREQUENCY METER
COAXIAL MATCHING NETWORK
TO THE COAXIAL FEED

Fig. 4.21.

1.9 GHz, it was found that when the input power to the feed network was varied over a 2:1 range (according to power meter readings), the SWR indicator showed very close to a 1.4:1 electric field amplitude variation. Thus, on the basis of these measurements, it was concluded that the crystal was exhibiting square-law behavior in the 40 dB meter range. It should be moted that when a ratio of powers is measured, all of the errors associated with the power measurement which are not a function of the power level are eliminated.

4.10. Measurement Procedure for the Lossless Case

In this section, the method by which the end admittance was determined by means of the system of Fig. 4.5 with a low loss substrate is presented. Now the previously discussed probing system is capable of measuring relative values of $|E_{zo}|$, so only information regarding the field magnitude is available. Assuming that the microstrip line contains no measurable losses, Eq. (4.8) indicates that the fundamental mode field in the slotted section of Fig. 4.5 possesses a standing wave characteristic. For convenience, Eq. (4.8) is restated here:

$$E_{zo}|_{y=0} = Ce^{-jk_o\alpha_o x}\left(1 + \hat{\Gamma}e^{j2k_o\alpha z}\right)$$

with

$$[-x_{fL} < x < 0] \quad .$$

The magnitude of Eq. (4.8) is plotted in Fig. 4.22 where the

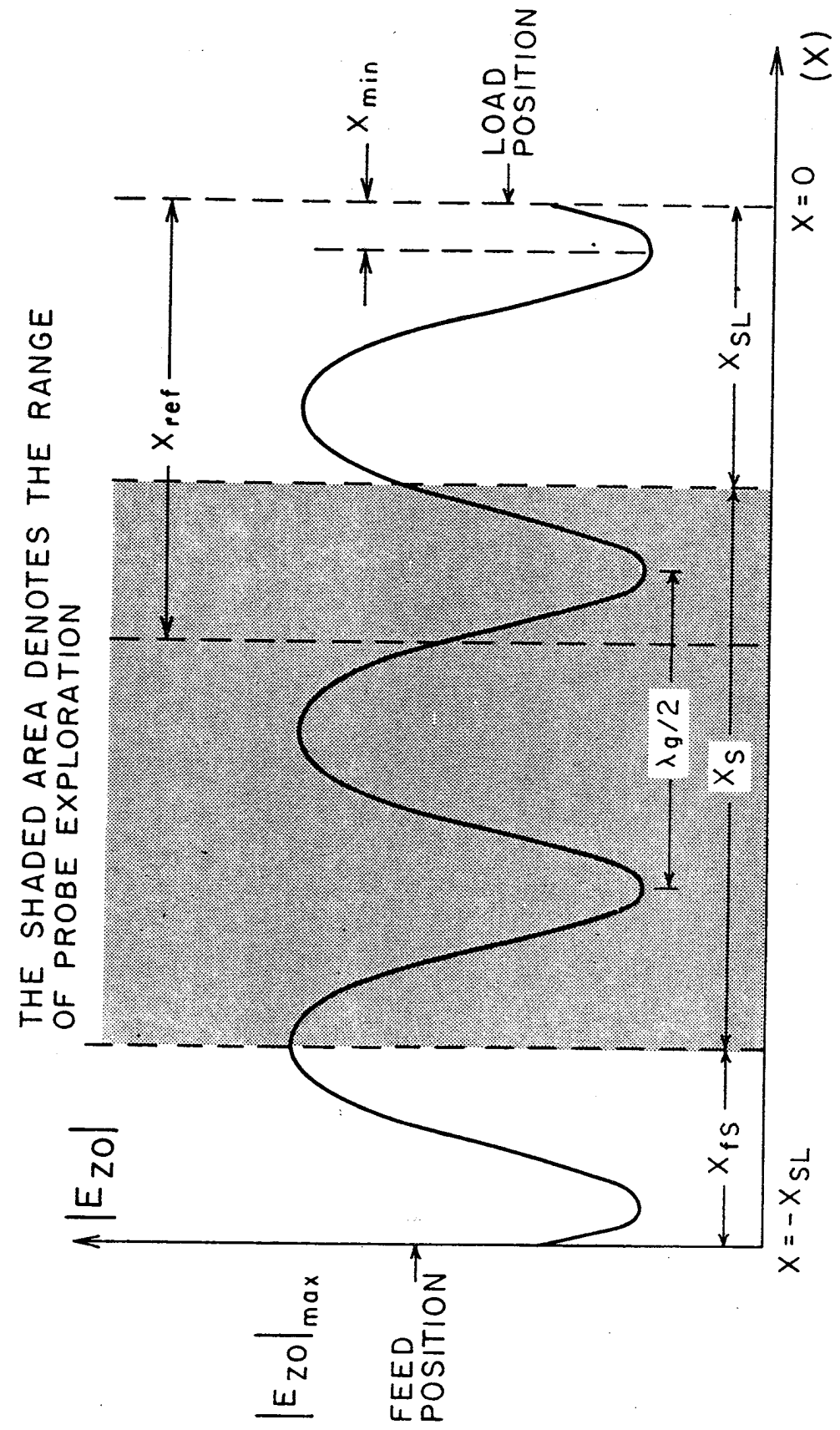
THE SHADED AREA DENOTES THE RANGE OF PROBE EXPLORATION
X_{ref}
X_{min}
LOAD POSITION
X_{SL}
X = 0
(X)
$\lambda g/2$
X_S
X_{fS}
$X = -X_{SL}$
$|E_{ZO}|$
$|E_{ZO}|_{max}$
FEED POSITION

Fig. 4.22.

standing wave behavior is readily apparent. $|E_{zo}|$ is periodic in x with a period of $\frac{\lambda_g}{2}$, where λ_g is the wavelength of the fundamental mode. In terms of the Chapter II development, λ_g is given by

$$\lambda_g = \frac{2\pi}{k_o \alpha_o} \quad . \tag{4.12}$$

As can be seen in Fig. 4.22, the maximum and minimum values of the standing wave pattern are $|E_{zo}|_{max}$ and $|E_{zo}|_{min}$, respectively. The standing wave ratio on the microstrip line is given by

$$SWR = \frac{|E_{zo}|_{max}}{|E_{zo}|_{min}} \quad .$$

Applying Eq. (4.8) to this definition yields

$$|\Gamma| = \frac{SWR - 1}{SWR + 1} \quad . \tag{4.13}$$

Thus, the standing wave ratio, which is readily calculated from slotted line measurements, determines the magnitude of the open end reflection coefficient. x_{min}, shown in Fig. 4.22, is the distance from the first minimum to the open end at $x = 0$. From Eq. (4.8), a minimum occurs at $x = -x_{min}$ when $|1 + \hat{\Gamma} e^{+j2k_o \alpha_o (-x_{min})}|$ is minimized. Since $\hat{\Gamma} = |\Gamma| e^{j\chi}$, the electric field magnitude is a minimum when

$$\chi - 2k_o \alpha_o x_{min} = -\pi$$

Rearranging this equation and applying Eq. (4.12) to this result yields

$$\chi = \frac{4\pi}{\lambda_g} x_{min} - \pi \quad . \tag{4.14}$$

Although the choice of sign associated with π makes no difference in the solution for χ, it is more convenient to use $-\pi$. Details have not yet been given as to how to determine the SWR, x_{min}, and λ_g, but Eqs. (4.13) and (4.14) form the basis from which to calculate $\hat{\Gamma}$ and, therefore, $\hat{y}$ using slotted line measurements.

In order to calculate the SWR, the double minimum technique, as presented in Ginzton [17], was employed. This approach involved accurate measurements of the probe carriage displacement about an electric field minimum as is shown in Fig. 4.23. The first step in this procedure, then, was to move the probe carriage along the slot until a minimum in the electric field was encountered. With the probe at the minimum, the probe tuning was adjusted until the SWR meter indicated an SWR of 2. The probe carriage was then moved a small distance to one side of the minimum until the meter indicated an SWR of $\sqrt{2}$. Clearly, an SWR reading of $\sqrt{2}$ corresponds to a field magnitude of $\sqrt{2}\,|E_{zo}|_{min}$. Having measured the distance from the null position, the probe was then moved through the null position until the meter indicated an SWR of $\sqrt{2}$ once again. Denoting the distance between the $\sqrt{2}\,|E_{zo}|_{min}$ as Δx, the SWR was calculated from the relation

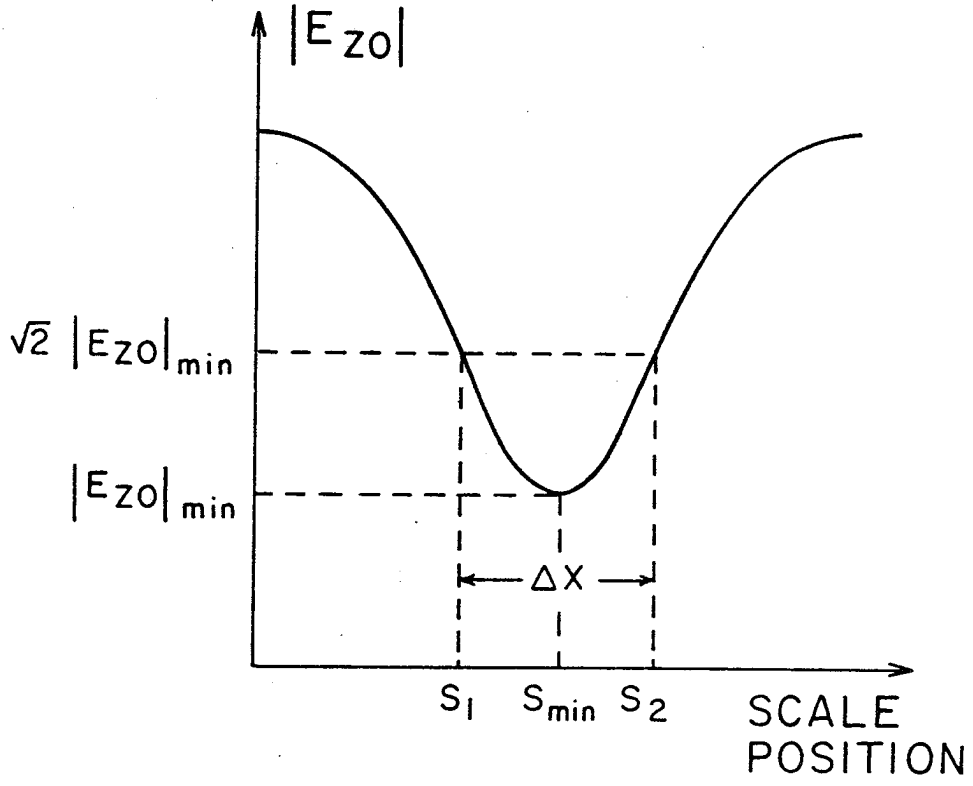

Fig. 4.23.

$$SWR = \sqrt{\frac{2}{1 - \cos \theta_o} + 1} \tag{4.15}$$

where

$$\theta_o = \frac{2\pi\Delta x}{\lambda_g} \quad .$$

Thus, in order to obtain a value for the standing wave ratio, the displacement Δx and the microstrip line wavelength λ_g are the values which need to be measured. According to Ginzton [17], the only assumption in Eq. (4.15) is a square-law response in the crystal detector. The square-law response was verified using the previously discussed calibration procedure.

Because an accurately calibrated coaxial attenuator was not available, the use of the double minimum technique was necessary because the ratio of power between the maxima and minima was found to be greater than 36:1. Over such a large range of power levels, the crystal detector does not maintain a square-law characteristic, which ruled out a direct reading on the SWR meter. Since the measurements are performed around a minimum in the standing wave pattern, the double minimum approach possesses the advantages of ensuring a constant crystal detector characteristic as well as reducing the standing wave pattern distortion due to power being coupled into the probe. The loading effects of the probe are not dealt with here, but they are discussed in detail in Ginzton [17] and Montgomery [18].

Since rapid field variations occur about the minima in the standing wave pattern, the knowledge of the location of these

points is appropriate in the measurement of λ_g. Referring to Fig. 4.23, a minimum location was calculated from the positions of the $\sqrt{2}\,|E_{zo}|_{min}$ points as follows:

$$S_{min} = \frac{S_1 + S_2}{2}$$

In this expression, S denotes a scale reading on the slotted section of Fig. 4.11. In order to measure λ_g, it is apparent from Fig. 4.22 that at least two minima must be located. In the case of the previously discussed air substrate cases, imperfections were introduced into the measurement process by variations in the substrate thickness; uncertainties in the distance measurements; the alignment of the top conductor with respect to the slot; the loading effects of the slot and the probe; and errors in instrument readings. In order to reduce the chance of making mistakes due to one or more of these imperfections, Δx and λ_g were calculated on the basis of three minima as illustrated in Fig. 4.24. Thus, in terms of this figure, the values of Δx and λ_g that were used in the calculation of $|\Gamma|$ are given by

$$\Delta x = \frac{\Delta x_1 + \Delta x_2 + \Delta x_3}{3}$$

$$\lambda_g = \lambda_1 + \lambda_2 \quad .$$

The fact that three minima were used as a basis for computing $|\Gamma|$ and λ_g explains why the length of the slot was designed to be $1.5\,\lambda_o$ at the lowest frequency of operation.

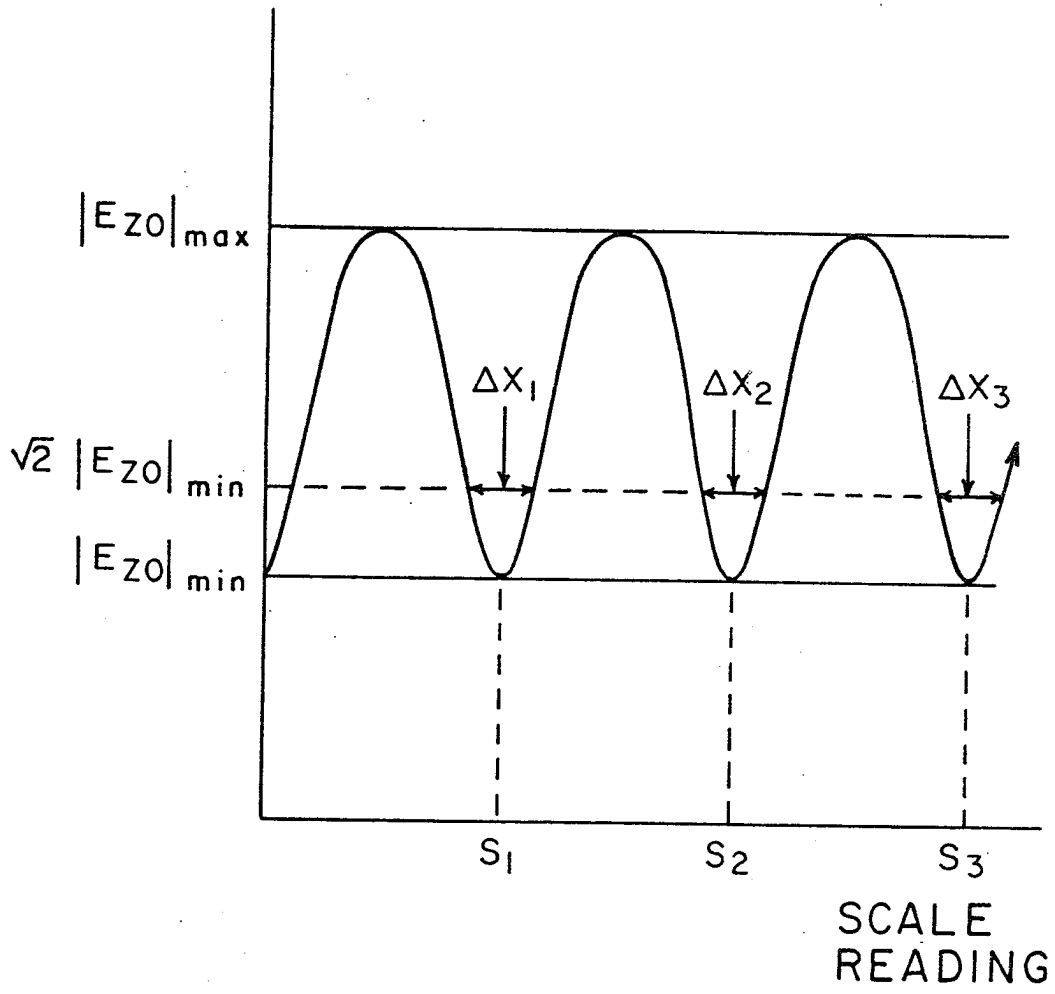
$|E_{zo}|_{max}$
$\sqrt{2}\,|E_{zo}|_{min}$
$|E_{zo}|_{min}$
ΔX_1
ΔX_2
ΔX_3
S_1
S_2
S_3
SCALE READING

Fig. 4.24.

It is apparent from Eq. (4.14) that once λ_g and x_{min} are known, the phase χ of the reflection coefficient can be calculated. Because the slot was located at least a full wavelength away from the open end of the microstrip line, the position of the first minimum could not be measured directly. At this point, let S denote a position indication on the slotted section scale of Fig. 4.11. Once the distance x_{ref} from the open end to the reference line in the slotted section (see Fig. 4.9) was known, the distance x_{min} was calculated from slotted section measurements. Assuming that a minimum is located at a position S_{min}, the electrical distance D from the minimum to the open end was determined by the following equation:

$$D = \frac{S_{min} - S_{ref} + x_{ref}}{\lambda_g} \quad . \tag{4.16}$$

In Eq. (4.16), S_{ref} denotes the indicator scale reading (see Fig. 4.11) when the probe was aligned with reference line of the center piece. As has already been mentioned, the standing wave pattern possesses minima at intervals of $\lambda_g/2$. Thus, if the nearest integer multiple of ½ which is still smaller than D is subtracted from D, the resulting value is the electrical distance from the first minimum to the open end. Mathematically,

$$\frac{x_{min}}{\lambda_g} = D - (\text{nearest multiple of } \tfrac{1}{2} < D) \quad . \tag{4.17}$$

Applying Eq. (4.17) to Eq. (4.14) permits the calculation of the

phase χ from the slotted section measurements. Referring to Fig. 4.22 once again, the value of x_{min}/λ_g used to compute the phase of $\hat{\Gamma}$ was obtained by averaging the three values of x_{min}/λ_g that resulted from the application of S_{min1}, S_{min2}, and S_{min3} to Eq. (4.17). Once $|\Gamma|$ and χ were found, the end admittance was calculated from Eq. (2.33).

4.11. Measurement Procedure for the Lossy Case

In addition to the series of measurements that were performed with low loss foamed dielectric substrate, an additional set of measurements were taken using a lossy polycarbonate (Lexan) substrate. This section deals with the procedure by which $\hat{\Gamma}$ and, therefore, $\hat{y}$ was computed from slotted section measurements on a lossy microstrip line.

Having used a sample of the polycarbonate material in a cavity measurement system developed by Durvasula [12], the relative dielectric constant of this material was found to be 2.82 with a loss tangent of 0.015 at the frequency of 3.015 GHz. Clarke [23] lists values of $\varepsilon_r \simeq 2.76$ and $\frac{\varepsilon_i}{\varepsilon_r} \simeq 0.011$ at $f = 1.0$ GHz (within the accuracy of reading his curves). Because of the loss tangent of the Lexan substrate, the propagation constant of the fundamental mode can be expressed as the complex quantity

$$k_o\alpha = k_o\alpha_r - jk_o\alpha_i \quad . \tag{4.18}$$

Assuming that $k_o d \ll 1$ and $\frac{\varepsilon_i}{\varepsilon_r} \ll 1$ in Eq. (2.36), the following relations result:

$$\alpha_r \simeq |\alpha| \tag{4.19}$$

$$k_o \alpha_i \simeq \frac{k_o \alpha_r}{2} \left(\frac{\varepsilon_i}{\varepsilon_r} \right) \quad . \tag{4.20}$$

Since α_i is roughly 1% of α_r in the frequency range of this experiment, Eq. (4.20) indicates that the loss tangent of 0.015 results in a noticable decay in the magnitude of the fundamental mode as it propagates down the misrostrip line. Also, with $\alpha_r \simeq |\alpha|$, the line wavelength λ_g is not affected by the substrate loss to a first order of approximation. The actual change in λ_g is

$$O\left[\left(\frac{\varepsilon_i}{\varepsilon_r}\right)^2\right]$$

which is too small to be measured on this system. Assuming once again that the open end position of the system of Fig. 4.5 is located at $x = 0$, the electric field variation along the length of the line at $y = 0$ is

$$E_{zo}|_{y=0} = Ce^{-jk_o\alpha_r x} e^{-k_o\alpha_i x} \left[1 + \left(\hat{\Gamma} e^{2k_o\alpha_i x} \right) e^{j2k_o\alpha_r x} \right] \tag{4.21}$$

This equation indicates, unlike the lossless case, that the magnitude of the reflection coefficient is an exponential function of the position along the microstrip line.

A sketch of the magnitude of Eq. (4.21), analogous to that depicted in Fig. 4.22, is given in Fig. 4.25. The curve for $|E_{zo}|$

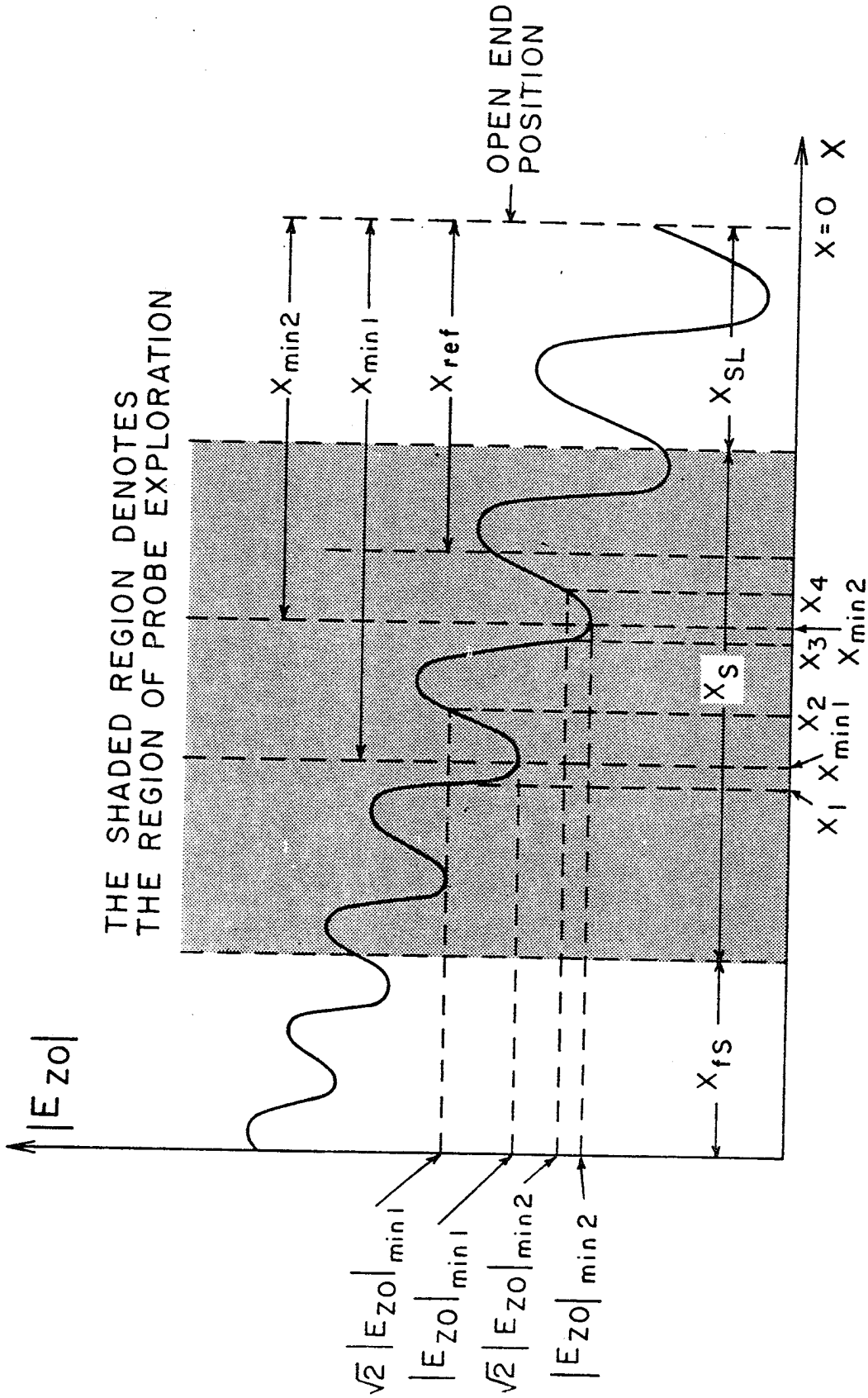
OPEN END POSITION
THE SHADED REGION DENOTES THE REGION OF PROBE EXPLORATION
$|E_{ZO}|$
X_{min2}
X_{min1}
X_{ref}
X_{SL}
X=0 X
X_4
X_3
X_{min2}
X_S
X_2
X_{min1}
X_1
X_{fS}
$\sqrt{2}\,|E_{ZO}|_{min1}$
$|E_{ZO}|_{min1}$
$\sqrt{2}\,|E_{ZO}|_{min2}$
$|E_{ZO}|_{min2}$

Fig. 4.25.

is quite different in form from that of the lossless case. The dielectric loss of the material produces a reduction in interference between the forward and backward traveling waves as the distance from the load increases. Although no minimum $|E_{zo}|$ exists in the lossy case, the pattern of Fig. 4.24 can be viewed as having local minima that are spaced $\lambda_g/2$ apart. The values of these local minima are designated $|E_{zo}|_{min}$, and the field magnitudes at these points differ from point to point.

Because of the different character of the standing wave pattern on a lossy microstrip line, the procedure for calculating $\hat{\Gamma}$ and, therefore, $\hat{y}$ of the open end, from slotted line measurements, had to be modified somewhat. In order to illustrate how $\hat{\Gamma}$ can be calculated from measurements on a lossy line, two successive local minima positions are located at x_{min1} and x_{min2} in Fig. 4.25. The electric field magnitudes at these points are $|E_{zo}|_{min1}$ and $|E_{zo}|_{min2}$, respectively. The points at which $|E_{zo}| = \sqrt{2}\,|E_{zo}|_{min1}$ are labeled x_1 and x_2; and the points where $|E_{zo}| = \sqrt{2}\,|E_{zo}|_{min2}$ are denoted by x_3 and x_4. Assuming that the $\sqrt{2}\,|E_{zo}|_{min}$ points are close together, the positions of the local minima are given by

$$x_{min1} = \frac{x_1 + x_2}{2}$$

$$x_{min2} = \frac{x_3 + x_4}{2} \quad .$$

The distances between the $\sqrt{2}\,|E_{zo}|_{min}$ points are

$$\Delta x_1 = x_2 - x_1$$

$$\Delta x_2 = x_4 - x_3 \quad .$$

Although a standing wave ratio cannot be defined in a strict sense for a lossy line, there is no reason why a local standing wave ratio that is a function of x (or S) cannot be defined. Once the local standing wave ratio has been defined, the relationship between the standing wave ratio and the reflection coefficient can be written

$$|\Gamma| e^{2k_o \alpha_i x} = \frac{SWR(x) - 1}{SWR(x) + 1} = |\Gamma(x)| \quad . \tag{4.22}$$

The functional dependence has been included in the SWR term in order to emphasize that it no longer has a constant value. Making the assumption of gradual decay and a high local SWR (small Δx), the $\sqrt{2}\,|E_{zo}|_{min}$ points can be assumed to be symmetrically displaced with respect to a local minimum. Once the assumption of symmetrical displacement is made, the double-minimum formula of Ginzton can be once again invoked to give

$$SWR(x) = \sqrt{\frac{2}{1 - \cos \theta_o} + 1} \tag{4.23}$$

where

$$\theta_o = \frac{2\pi \Delta x}{\lambda_g} \quad .$$

Inspection of Eq. (4.23) does not reveal an explicit dependence

on x. However, on a lossy line, Δx changes from one local minimum to the next. In fact, as one travels away from the load position in the negative x direction, the width Δx of each successive minimum increases monotonically. The variation in Δx, then, accounts for the x dependence in Eq. (4.23).

In order to evaluate $|\Gamma|$ $(x = 0)$, one must first determine the decay constant $k_o\alpha_i$. $k_o\alpha_i$ can, in principle, be determined from slotted line measurements by evaluating $|\Gamma|e^{2k_o\alpha_i x}$ at two different minima positions. Utilizing the two successive minima of Fig. 4.24 in conjunction with Eq. (4.22) yields

$$e^{2k_o\alpha_i(x_{min1}-x_{min2})} = \frac{[SWR(x_{min1}) - 1][SWR(x_{min2}) + 1]}{[SWR(x_{min1}) + 1][SWR(x_{min2}) - 1]} .$$

Solving for $k_o\alpha_i$ and simplifying by means of Eq. (4.22) yields

$$k_o\alpha_i = \frac{1}{2(x_{min2} - x_{min1})} \ln\left[\frac{|\Gamma(x_{min1})|}{|\Gamma(x_{min2})|}\right] . \qquad (4.24)$$

It should be noted that $k_o\alpha_i$ does not have to be determined from two successive minima. Any two distinct minima should suffice. Once $k_o\alpha_i$ is known, $|\Gamma(x=0)|$ at the open end position can be determined from either $|\Gamma(x_{min1})|$ or $|\Gamma(x_{min2})|$. Thus,

$$|\Gamma| = |\Gamma(x_{min1})|e^{-2k_o\alpha_i x_{min1}} \qquad (4.25)$$

$$= |\Gamma(x_{min2})|e^{-2k_o\alpha_i x_{min2}}$$

x_{min1} and x_{min2} can be found from the slotted section scale readings as

$$x_{min1} = S_{min1} - S_{ref} + x_{ref} \tag{4.26}$$

$$x_{min2} = S_{min2} - S_{ref} + x_{ref} \quad .$$

Equations (4.24), (4.25), and (4.26) provide the basis from which to calculate $|\Gamma|$ of the open end using slotted line measurements. As will be discussed in Chapter V, problems occurred in the measurement system that prevented the reliable measurement of $|\Gamma|$ in the dielectric case.

On account of the periodic occurrences of local minima at intervals of $\lambda_g/2$, the phase χ was determined in exactly the same fashion as in the low loss case. The equations developed for the lossless case were also employed in the calculation of χ in the lossy case.

CHAPTER V

A COMPARISON OF EXPERIMENTAL AND THEORETICAL RESULTS

5.1. Introduction

Having presented an experimental approach to determine the open end admittance of a microstrip line, results obtained by means of the slotted ground plane system are given in this chapter. The normalized end conductance values along with the associated susceptance values are presented for several air substrate cases and one dielectric substrate case. A comparison of experimentally obtained admittance values with those calculated from the theoretical models of Chapters II and III is also made. For the dielectric substrate, the measured dispersion is compared with the predictions from the transverse resonance condition. Both numerical and approximate solutions to the transverse resonance condition are employed.

5.2. Air Substrate Admittance Results

Upon utilizing the foamed dielectric materials with electrical properties very close to those of air, measurements were performed on four different microstrip line geometries. A 9 mm thick substrate was used in conjunction with top conductors

of widths 3" (76.8 mm), 4.5" (115.2 mm), and 6" (153.6 mm). The final air case consisted of a 4.5" wide copper strip (0.5 mm thick) supported by a 6.5 mm substrate. Open end admittance values were obtained in the 0.8 to 2.1 GHz frequency range, providing more than a 2 to 1 variation in $k_o d$.

In Fig. 5.1, the normalized conductance values obtained from the experiment are plotted as a function of $k_o d$. The experimental points are marked according to the microstrip line geometry, from which they were obtained. As a comparison, theoretical conductance values, calculated from Eqs. (2.19) and (2.32), are plotted as a function of $k_o d$. Eq. (2.19) is the approximate reflection coefficient obtained in Appendix A. It was found necessary to use the approximate solution since the computer program of Appendix B experiences numerical difficulties when ε_r is set too close to 1. As a check of the approximate formula, Eq. (2.9) was compared with the computer program with $\varepsilon_r = 1.1$ and $\alpha = 0$. Agreement to three decimal places in both magnitude and phase was obtained for $k_o d$ as high as 0.5.

As can be seen from Fig. 5.1, the functional dependence of the experimental conductance points is different from the Wiener-Hopf conductance. The worst disagreement between theory and experiment occurs in the case of the 3" wide conductor supported by a 9 mm substrate with an aspect ratio of $\ell/d = 4.27$. For this configuration, the relative errors vary from 293% at $k_o d = 0.157$ to 38% at $k_o d = 0.38$. The error is seen to decrease with increasing frequency ($k_o d$). Of course, as the source

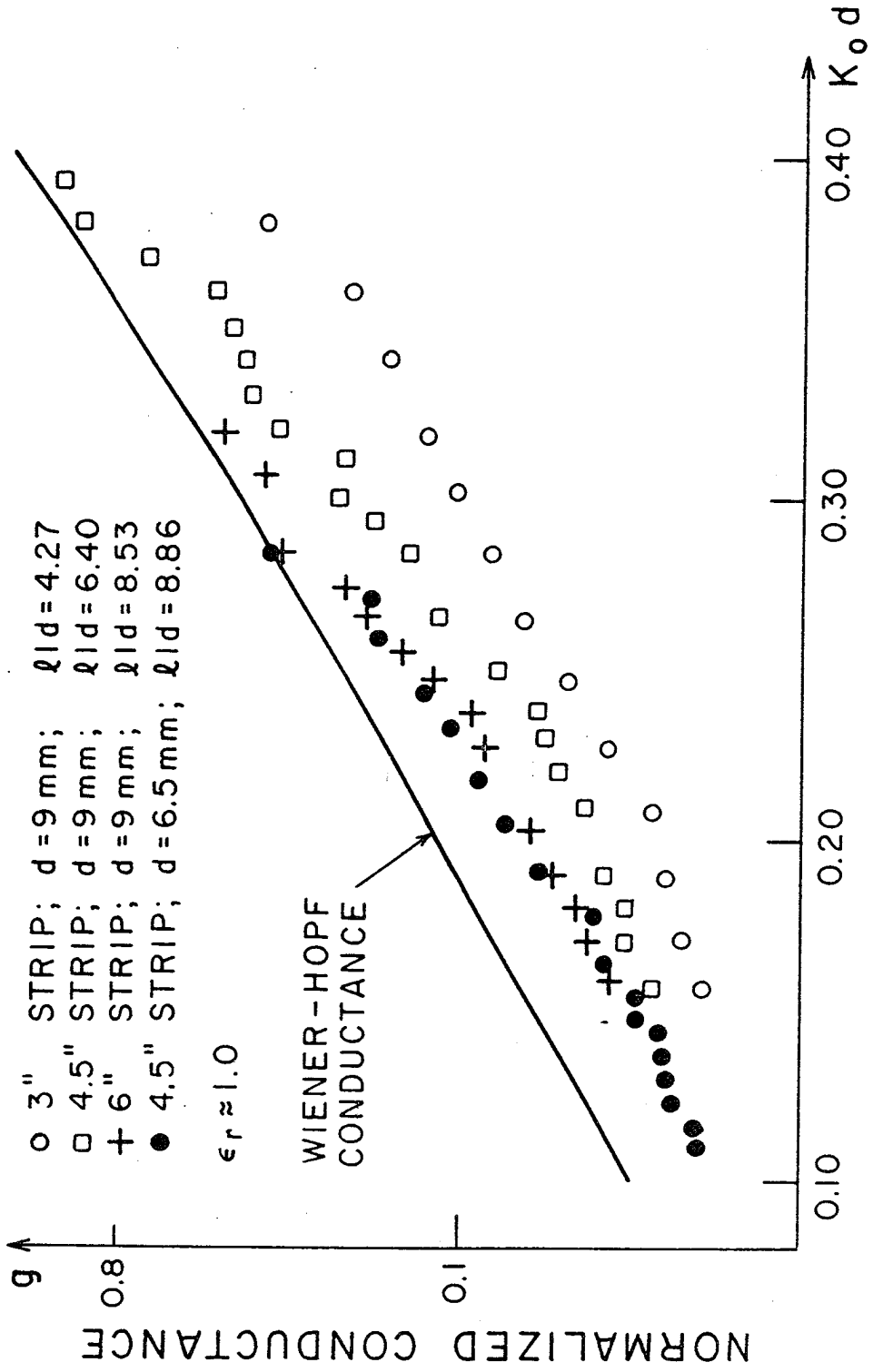
NORMALIZED CONDUCTANCE
g
0.8
0.1
0.10
0.20
0.30
0.40
$K_o d$
WIENER-HOPF CONDUCTANCE
$\epsilon_r \approx 1.0$
○ 3" STRIP; d=9mm; ℓ/d=4.27
□ 4.5" STRIP; d=9mm; ℓ/d=6.40
+ 6" STRIP; d=9mm; ℓ/d=8.53
● 4.5" STRIP; d=6.5mm; ℓ/d=8.86

Fig. 5.1.

frequency increases, the electrical width $k_o \ell$ increases linearly with $k_o d$. Since the Wiener-Hopf solution is, in principle, exact for an infinitely wide microstrip, one would expect the agreement between theory and experiment to improve with increasing $k_o \ell$. This phenomenon is, indeed, observed. For a 4.5" wide conductor and a 9 mm substrate ($\ell/d = 6.40$), the relative error at $k_o d = 0.157$ is 91%, and the relative error at $k_o d = 0.38$ is 3.8%. For the same $k_o d$ value, the corresponding $k_o \ell$ is 1.5 times greater in the 4.5" case than in the 3" case. The improvement in agreement between theory and experiment is obvious. A 6" wide conductor supported by a 9 mm substrate results in an even greater aspect ratio of $\ell/d = 8.53$, which means that $k_o \ell$ is now 1.33 times as great as that of the 4.5" strip for the same $k_o d$. The relative error between theory and experiment is 50% at $k_o d = 0.159$ and 5.3% at $k_o d = 0.319$. The trend of better agreement between theory and experiment with increasing $k_o \ell$ seems even more evident. One more microstrip line structure was investigated in the air case. The line consisted of a 4.5" wide strip supported by a 6.5 mm substrate with the aspect ratio $\ell/d = 8.86$. This aspect ratio is quite close to that of the previously mentioned 6" line. The effect of similar aspect ratios is clearly evident in Fig. 4.1 in which the experimentally obtained conductance values agree very closely. Thus, as a function of $k_o d$, the conductance characteristic appears to be determined by the aspect ratio ℓ/d; and as the aspect ratio increases, the agreement between theory and experiment improves.

More knowledge about the nature of the normalized conductance can be gained if the experimental results are examined in greater detail. Plotting the conductance data on log-log paper indicates that the various conductance curves have the form of a power function in the range $0.1 \leq k_o d \leq 0.38$. Performing a power curve fit by the method of least squares results in the following conductance variations:

$$g \simeq 0.937(k_o d)^{1.87} \qquad 2\ell = 3" \text{ (76.8 mm)}; \; d = 9 \text{ mm} \tag{5.1}$$

$$g \simeq 1.16(k_o d)^{1.81} \qquad 2\ell = 4.5" \text{ (115.2 mm)}; \; d = 9 \text{ mm} \tag{5.2}$$

$$g \simeq 1.15(k_o d)^{1.67} \qquad 2\ell = 6" \text{ (153.6 mm)}; \; d = 9 \text{ mm} \tag{5.3}$$

$$g \simeq 1.27(k_o d)^{1.72} \qquad 2\ell = 4.5" \text{ (115.2 mm)}; \; d = 6.5 \text{ mm} \; . \tag{5.4}$$

For the range $0.1 \leq k_o d \leq 0.38$, the Wiener-Hopf values were also power curve fitted, yielding

$$g \simeq 0.633(k_o d)^{1.11} \; . \tag{5.5}$$

Eqs. (5.1) through (5.5) are plotted in Fig. 5.2 along with the experimental data. The power curves are seen to fit the experimental and theoretical points closely. Although these equations are valid for the range of data to which they have been fitted, an interesting trend is apparent. Inspection of the powers of Eqs. (5.1) through (5.4) indicates that as the aspect ratio ℓ/d

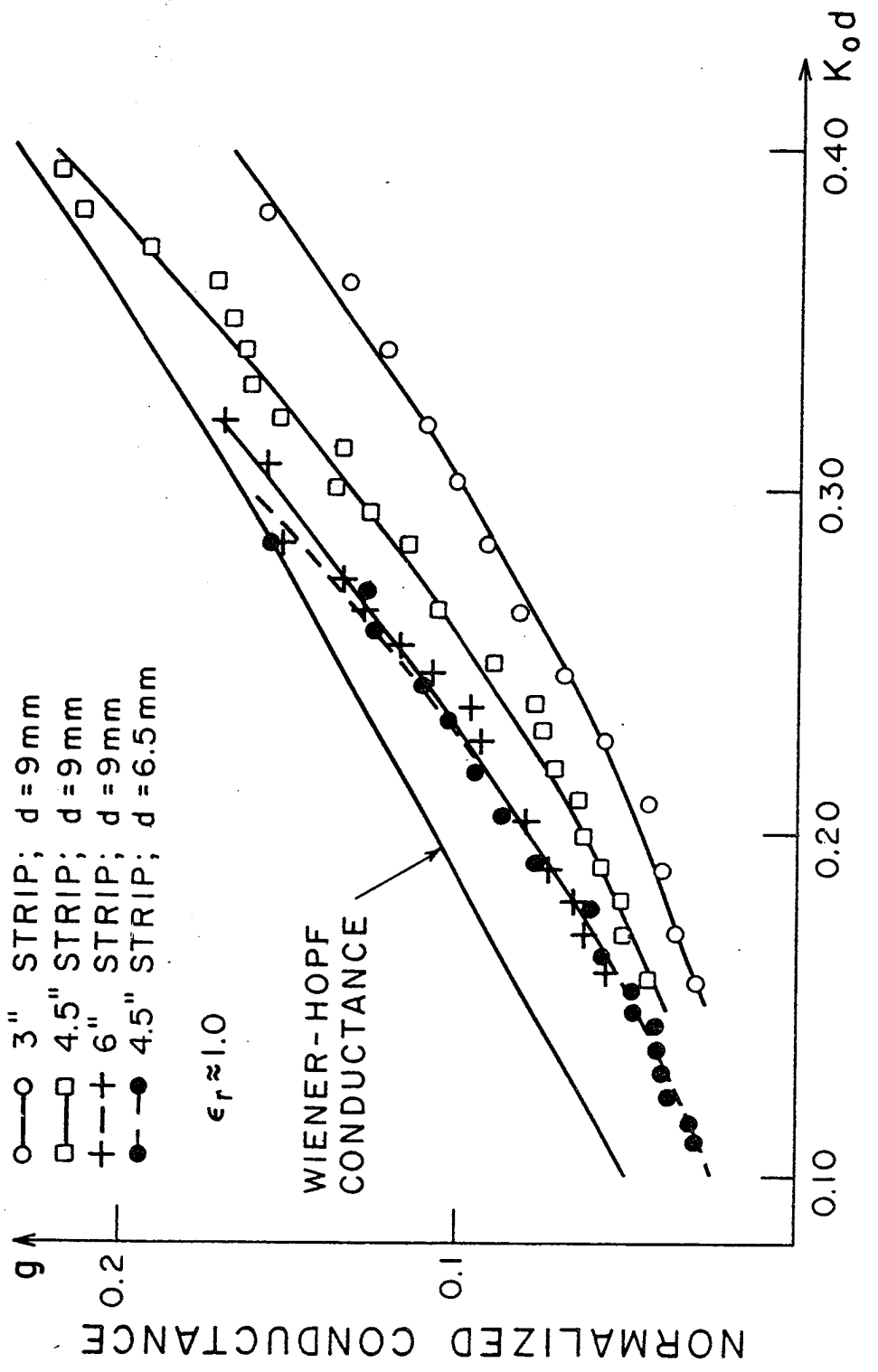
NORMALIZED CONDUCTANCE
g
0.2
0.1
0.10
0.20
0.30
0.40
$K_o d$
WIENER-HOPF CONDUCTANCE
$\epsilon_r \approx 1.0$
3" STRIP; d = 9mm
4.5" STRIP; d = 9mm
6" STRIP; d = 9mm
4.5" STRIP; d = 6.5mm

Fig. 5.2.

of the microstrip line increases, the exponent of the power function appears to be decreasing. This fact is consistent with the results of Derneryd's analysis (Chapter II) in which a square law conductance variation is found for $\ell/d << 1$ (Eq. 3.16) and a linear variation for $\ell/d >> 1$ (Eqs. 3.15 and 3.18). For the smallest aspect ratio, the exponent of the power function is close to 1.9 which is, in fact, approaching a square law variation. In the case of the two largest aspect ratios, the conductance expression has a power that is roughly 1.7. One would expect the conductance function to agree more closely with the Wiener-Hopf model as the ratio ℓ/d increases.

Making use of Eqs. (5.2) through (5.5), the $k_o\ell$ values at which the experimental curves agree with the theoretical ones to within 10% have been computed and are tabulated below.

Table 5.1

d (mm)	ℓ (mm)	$k_o d$	$k_o \ell$
9	57.6	0.37	2.37
9	76.8	0.28	2.48
6.5	57.6	0.29	2.47

Table 5.1 indicates that the experimental results agree to within 10% of the theory at roughly the same $k_o\ell$ value. The $k_o\ell$ value corresponds to a total conductor width of $2\ell \simeq 3\lambda_o/4$,

where λ_o denotes the free space wavelength. Thus, for the Wiener-Hopf theory to predict a reasonable conductance, the electrical width of the top conductor must be roughly halfway between a half and a full wavelength.

In addition to normalized conductance values shown in Fig. 5.2, the experimental susceptances obtained for the same foamed dielectric substrates are plotted in Figs. 5.3 and 5.4. One of the solid curves in these figures is generated from the approximate Wiener-Hopf reflection coefficient solution (Eq. 2.19) in conjunction with Eq. (2.32). The straight lines in these figures correspond to susceptances calculated from the static results of Silvester and Benedek (Chapter III). Eqs. (3.26) and (2.38) have been used to produce the static susceptance curves. In Fig. 5.3, only the static characteristic for the 6" wide top conductor and a 9 mm substrate has been included. The curves corresponding to the other two cases with a 9 mm substrate were not included since these lie close to and slightly below (< 1%) the 6" chatacteristic. It is of interest to note that if one computes the normalized susceptance from Eq. (3.27) (instead of Eq. (3.26)) and from Eq. (2.38) the resulting susceptance curve falls approximately 7% below that predicted by Eq. (2.26).

As is readily seen in these graphs, the experimental data agree well with the predictions of the Wiener-Hopf theory. For almost all of the points, the agreement between theory and experiment is 10% or better. Considering the position of the static susceptance lines, the measured results decisively favor

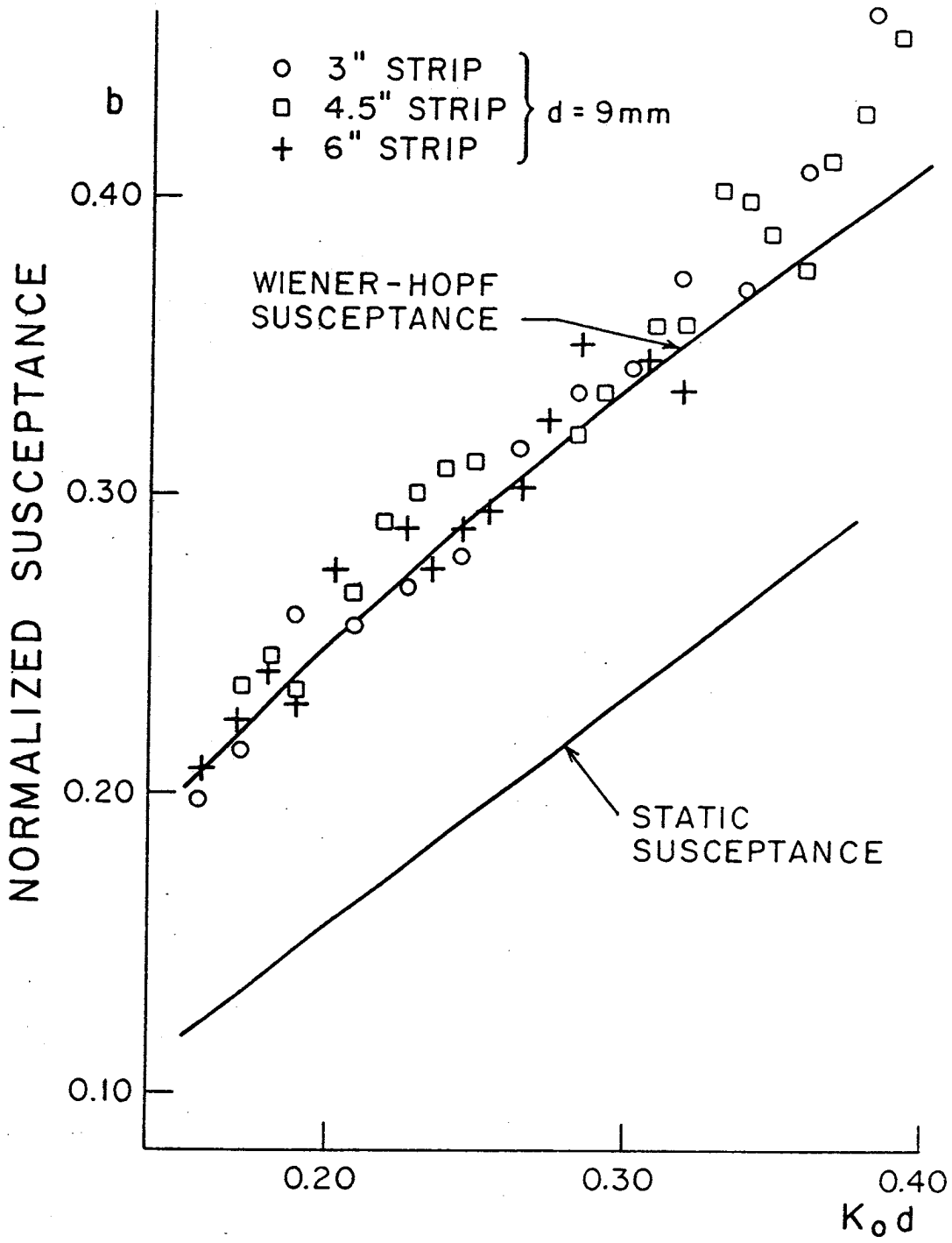
b
NORMALIZED SUSCEPTANCE
0.40
0.30
0.20
0.10
3" STRIP
4.5" STRIP
6" STRIP
d = 9mm
WIENER-HOPF
SUSCEPTANCE
STATIC
SUSCEPTANCE
0.20
0.30
0.40
K o d

Fig. 5.3.

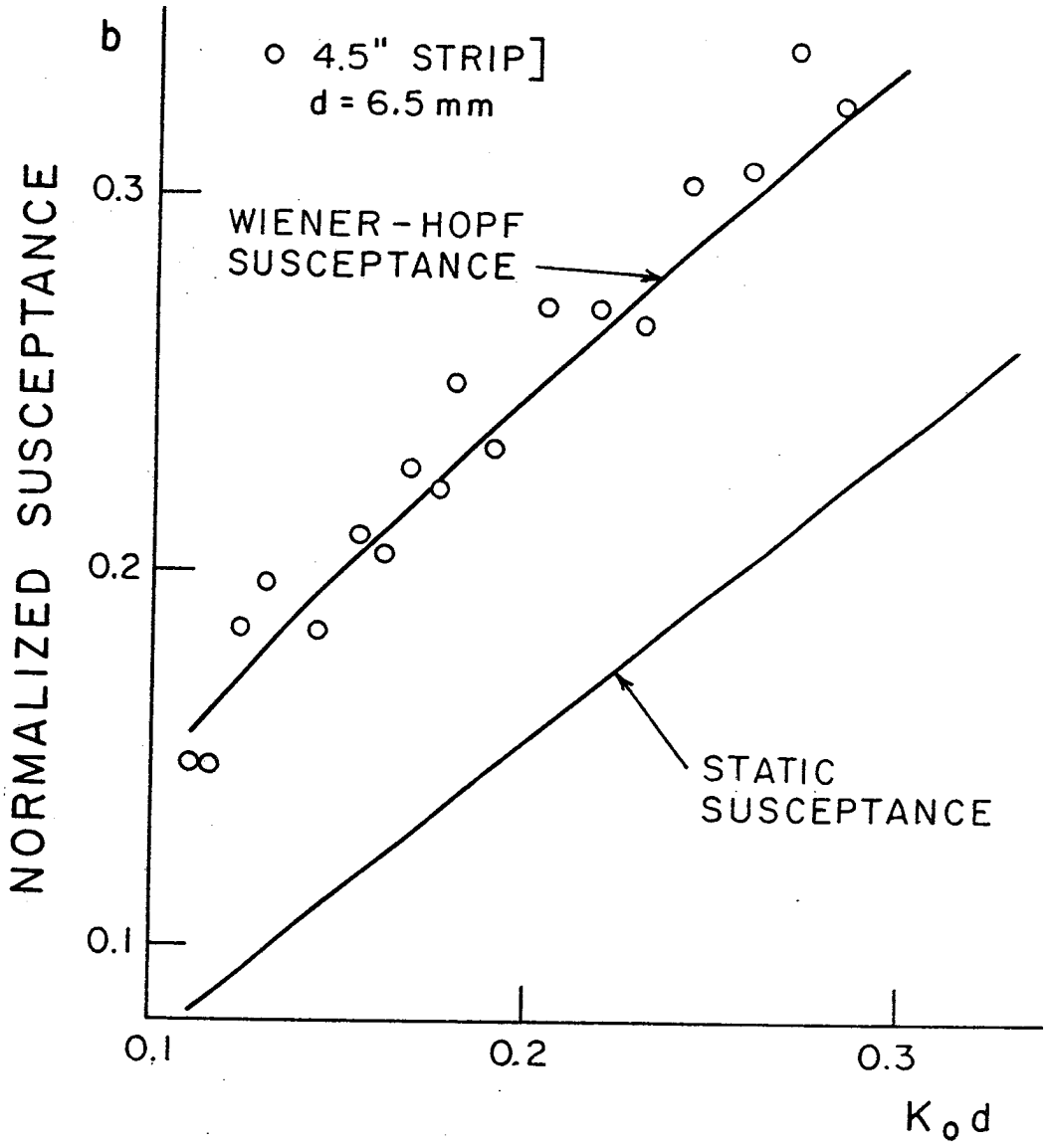
b
4.5" STRIP]
d = 6.5 mm
WIENER-HOPF
SUSCEPTANCE
STATIC
SUSCEPTANCE
NORMALIZED SUSCEPTANCE
0.3
0.2
0.1
0.1
0.2
0.3
K o d

Fig. 5.4.

the Wiener-Hopf theory. At $k_o d = 0.11$, the relative error between the Wiener-Hopf susceptance and the static susceptance is 90%; and at $k_o d = 0.376$, the relative is 36%. With errors as large as these, the static approach provides a very inaccurate prediction of the end susceptance. The poor accuracy of the static approach is probably due to the fact that high frequency effects cannot be properly accounted for by this method. Considering the conductance results, it is interesting to see that the susceptance values agree consistently with the Wiener-Hopf predictions for all of the $k_o d$ values. The reason for this phenomenon is not clear.

5.3. The Occurrence of the First Even Leaky Mode

As is apparent from the susceptance and conductance curves, no experimental data were taken above $k_o d = 0.319$ ($f = 1.695$ GHz) in the case of a 6" wide top conductor supported by a 9 mm substrate. At $f = 1.71$ GHz, the E_z field in the slotted section no longer exhibited a periodic standing wave characteristic. The $|E_z|$ pattern exhibited properties of an interference pattern between two modes. As the frequency increased, this effect became even more pronounced. Because of the symmetrically displaced coaxial feed, it appears that the first even leaky mode was excited. Now the corresponding electrical width of the top conductor at $f = 1.71$ GHz for the 6" strip is $k_o \ell = 2.75$. From Eq. (2.21), the modes on a microstrip are given by

$$2k_o \ell = \frac{m\pi + \chi}{\sqrt{n^2 - \alpha_m^2}} \qquad m = 0, 1, 2, \ldots$$

In the case of an air substrate (n = 1), the first even leaky mode corresponds to the solution of Eq. (2.21) with m = 2. Assuming that the first even leaky mode can be detected when $\alpha_2 = 0$, Eq. (2.21) yields the following condition:

$$k_o \ell = \frac{2\pi + \chi}{2} \quad .$$

From Eq. (2.19), the phase of $\hat{\Gamma}$ at $k_o d = 0.3223$ (f = 1.71 GHz) is $\chi = -0.6962$. Applying this to the above equation yields $k_o \ell = 2.79$. The fact that Eq. (2.21) predicts the appearance of the first leaky mode to within 2% certainly indicates the validity of the transverse resonance formulation. It is interesting to note that Marin [24] (to within the accuracy of reading his curves) predicts the appearance of the first leaky mode at $k_o \ell \simeq 2.7$. This comes as no surprise since Marin also utilizes a Wiener-Hopf solution for the leaky modes.

5.4. The Polycarbonate Substrate Admittance Values

In addition to the various air substrate cases, measurements were also performed on the previously described polycarbonate substrate (d = 9.2 mm; $\varepsilon_r = 2.82$). The width of the top in this case was 2ℓ = 2" (51.2 mm) with an associated aspect ratio of $\ell/d = 2.78$. Although the measurement approach outlined in Chapter IV was used to obtain the phase of the reflection coefficient of

the open end, difficulties were encountered in trying to measure the standing wave ratio at each of the local minima by means of the double-minimum technique. With no reliable information regarding the local SWR, $|\Gamma|$ values for the open end could not be computed. However, in spite of the nature of the difficulties encountered, reliable reflection coefficient phase values were calculated from the slot measurements. It is clear that, in an exact sense, both the magnitude and phase of the reflection coefficient must be known in order to calculate the normalized end susceptance of the open end. As is discussed in Chapter II, however, the susceptance can be calculated from the phase of the reflection coefficient under the assumption of $|\Gamma|$ being close to unity. Thus, Eq. (2.34) was used as the basis for calculating the susceptance from the reflection coefficient information. For convenience, Eq. (2.34) is stated here:

$$b = -\tan\left(\frac{\chi}{2}\right) \quad .$$

Further justification of the use of Eq. (2.34) is given later in this section.

The difficulties that prevented the calculation of the magnitude of the open reflection coefficient are now discussed. By means of metal weights and beadboard blocks, pressure was applied to the top of the microstrip line as is shown in Fig. 5.5. The purpose of the beadboard blocks is to provide sufficient separation between the metal weights and the transmission structure,

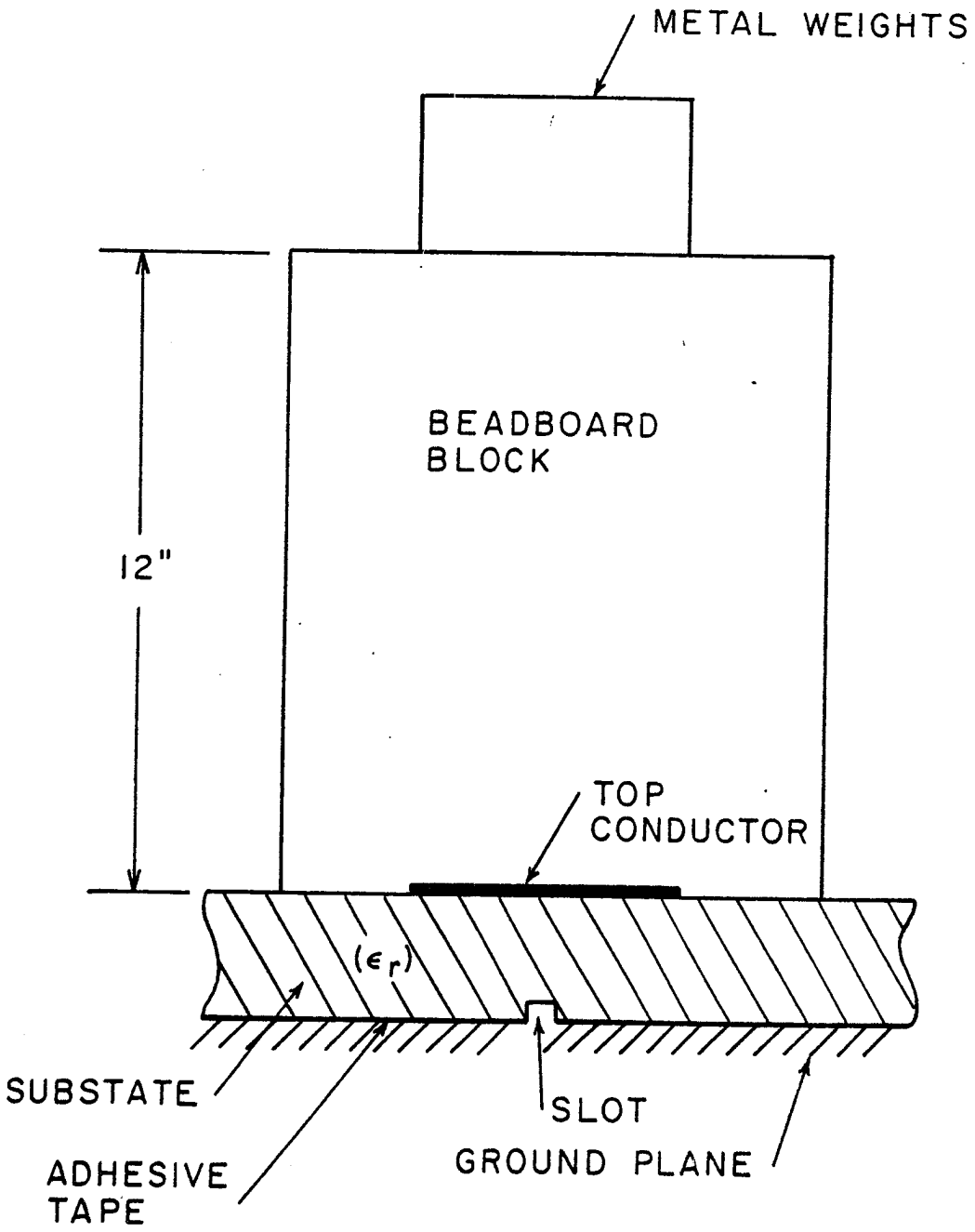
METAL WEIGHTS
BEADBOARD
BLOCK
12"
TOP
CONDUCTOR
(ϵ_r)
SUBSTATE
ADHESIVE
TAPE
SLOT
GROUND PLANE

Fig. 5.5.

thereby preventing measurable field disturbances. Basically, the local SWR measurement problem arose when the pressure on the substrate was varied. It was observed that the distance between the $\sqrt{2}\,E_{min}$ points along with the value of E_{min} changed with the applied pressure. The effects of this problem are illustrated at a source frequency of 928 MHz. At this frequency, four local minima were encountered in the slotted section. With no applied pressure, the widths Δx of these local minima were found to be 0.64 cm, 0.55 cm, 0.43 cm, and 0.41 cm, respectively (proceeding towards the load). When heavy pressure was applied to the substrate, the widths became 0.49 cm, 0.44 cm, 0.37 cm, and 0.31 cm. It is of interest to note that although the widths Δx changed significantly, the computed phases for these cases are -22.6° and -21.3°, which are in very good agreement. As is mentioned in Chapter IV, the widths Δx of the local minima should decrease monotonically as the load is approached. In fact, for the polycarbonate substrate, the widths should decrease roughly in equal increments. This appears to be the case with the 928 MHz data; it was not so for a number of data points, with and without applied pressure. For instance, at $f = 1.224$ GHz with heavy applied pressure, the widths of the minima were 0.61 cm, 0.50 cm, 0.51 cm, and 0.39 cm. The inconsistencies in the minima widths, then, call into question the validity of a reflection coefficient magnitude calculated from slotted section measurements. On the basis of Eq. (2.34), the end conductance cannot be calculated unless the reflection coefficient magnitude is known. Thus, no reliable conductance data could be obtained in

the dielectric substrate case.

On the other hand, it was observed that the measured microstrip line wavelength λ_g and the calculated phase of the open end reflection coefficient were virtually independent of the applied pressure. Now λ_o/λ_g is easily calculated from the experimental data; and in terms of the Chapter II notation, λ_o/λ_g is the quantity α. Recalling the previous discussion in Chapter II, α can be determined from the transverse resonance condition (Eq. 2.21) for $nk_o\ell \gtrsim 0.5$. Since the smallest value of $nk_o\ell$ in the experiment was 0.77, a comparison of the measured α with that predicted by the transverse resonance condition should provide a good indication as to how effectively the experimental system performed. A comparison of the experimentally obtained α values with those generated from the transverse resonance condition ($\varepsilon_r = 2.82$; $\ell = 25.6$ mm; $d = 9.2$ mm) is located in Table 5.2. Along with computer generated α values, α has also been calculated from the approximate expressions (Eqs. 2.25 and 2.26). It should be noted that the effects of the loss on α has not been included since this is too small to be measured. The computer-generated values are numerically exact, so these should provide the basis for comparison. The agreement between the computer values and the measured α is certainly encouraging. Errors no larger than 0.7% occur between the theoretically predicted values (computer) and the experimental results. This fact indicates that the taping of the substrate has defeated the problems produced by air pockets between the substrate and the ground plane. The approximate formula (Eq. 2.25) appears to predict the value of α

Table 5.2.

Frequency GHz	Experimental Value	Computer Value	Eq. (2.25)	Eq. (2.26)
0.842	1.575	1.578	1.580	1.545
0.885	1.572	--	1.582	1.548
0.929	1.576	--	1.584	1.551
0.933	1.578	--	1.584	1.551
1.032	1.580	1.582	1.588	1.557
1.035	1.581	--	1.588	1.557
1.084	1.581	--	--	--
1.167	1.582	--	1.593	1.565
1.224	1.586	--	1.595	1.568
1.318	1.584	1.593	1.598	1.572
1.405	1.587	--	1.600	1.576
1.525	1.591	1.599	1.603	1.581

accurately, but the simplified version of Eq. (2.25) (Eq. 2.26) does not. This is attributable to the fact that the aspect ratio ℓ/d is not large enough for Eq. (2.26) to be accurate. It should finally be noted that if the value of ε_r in the computer program is varied by ±2%, the resulting α values will vary roughly ±1%. This is of importance in assessing errors that might be produced by uncertainties in measuring the substrate dielectric constant.

Since the measured standing wave ratios, although inconsistent, appear to be high along with those predicted by the computer program of Appendix B, the use of Eq. (2.34) to calculate the susceptance from the measured phase seems to be a valid procedure. The susceptance values calculated in this fashion are plotted in Fig. 5.6 as a function of the electrical substrate thickness $k_o d$. Along with the experimental results, five susceptance curves, produced by the computer program of Appendix B, were drawn. Each curve, corresponding to a single α value, was generated by setting $\varepsilon_r = 2.82$ and varying $k_o d$ for $\alpha = 1.57$, 1.58, 1.59, 1.60, or 1.68. In addition to the Wiener-Hopf susceptances, the static susceptance was plotted by means of Eqs. (3.27) and (2.38). As is the case with the air substrate, the Wiener-Hopf susceptance agrees well with the measured results. In fact, the relative error between the experimental values and the four susceptance curves, in the range $1.57 \leq \alpha \leq 1.60$, is less than 10%. Since the measured and calculated α values lie within the same range, the results are particularly satisfying. The good agreement means that the Wiener-Hopf susceptance properly accounts for the dispersion of the microstrip line. This fact is

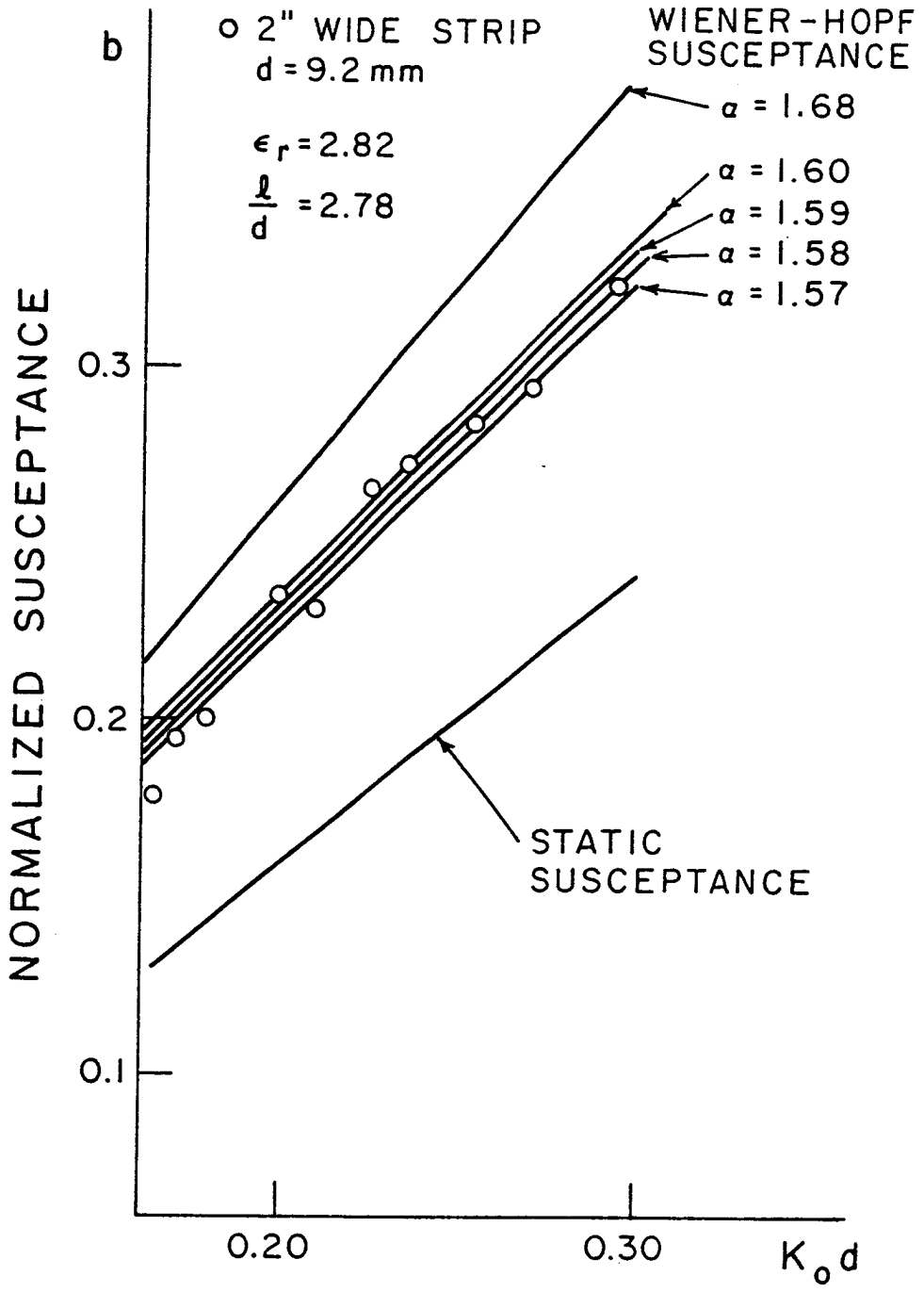
b
o 2" WIDE STRIP
d = 9.2 mm
ϵ_r = 2.82
$\frac{l}{d}$ = 2.78
WIENER-HOPF
SUSCEPTANCE
α = 1.68
α = 1.60
α = 1.59
α = 1.58
α = 1.57
STATIC
SUSCEPTANCE
NORMALIZED SUSCEPTANCE
0.3
0.2
0.1
0.20
0.30
$K_o d$

Fig. 5.6.

more readily apparent when one compares the experimental results and the four curves in the range $1.57 < \alpha < 1.60$ with the curve for $\alpha = 1.68$, which corresponds to the grazing incidence case ($\alpha = n = \sqrt{2.82}$). In Fig. 5.6, the static susceptance once again does poorly in predicting the end susceptance. The relative error between the experimental values and static susceptance ranges from 33% to 38%. It seems apparent that the static theory does not adequately account for the high-frequency effects.

5.5. Conclusions

All in all, the results of this experiment are quite encouraging. The dielectric and air substrate data demonstrate that the Wiener-Hopf theory properly incorporates the high-frequency effects into the modeling of the open end susceptance. On the other hand, the static approach has proved to be totally inadequate. An especially interesting result in the dielectric case is the fact that the incorporation of the angle of incidence in the Wiener-Hopf reflection coefficient produces a susceptance that is in excellent agreement with the experimental results. Another discovery concerns the functional dependence of the end conductance being completely different from the predictions of the Wiener-Hopf theory. Although the measured conductance characteristics are quite different from the Wiener-Hopf model, good agreement occurs when $2k_o \ell \geq \frac{3}{4} \lambda_o$ (air case). It is unfortunate that no reliable conductance data could be obtained in the dielectric substrate case. But based on the air substrate results, one might be able to generalize the above

result to $2nk_o\ell \geq \frac{3}{4}\lambda_o$. This generalization is, of course, a matter of speculation.

It should be remembered that the Wiener-Hopf canonical problem was originally solved so it could be used to develop the theory of an unloaded rectangular patch antenna [2]. In determining the dimensions of the microstrip antenna, the critical factor is the phase of the Wiener-Hopf reflection coefficient. The magnitude of the reflection coefficient does not affect the dimensions. Since the susceptance data along with the dispersion measurements agreed well with the Wiener-Hopf theory for all values of $k_o d$ and aspect ratios ℓ/d, it appears that the Wiener-Hopf theory should accurately predict the patch dimensions over a fairly broad range of $k_o\ell$ and $k_o d$. Although the conductance does not have an effect on the patch antenna dimensions, it does govern the radiation characteristics. Now typical rectangular microstrip antennas have electrical widths in the range $\lambda_g/2 \leq 2k_o\ell < \lambda_g$ where $\lambda_g = \lambda_o/n$. On the basis of the experimental results, the Wiener-Hopf technique should yield precise antenna dimensions; and if the patch is operated in the middle to upper portion of this range, the radiation characteristics, too, should be accurately modeled. Insofar as microstrip antenna design is concerned, the Wiener-Hopf technique should provide the basis for more accurate designs.

As the experimental results indicate, the Wiener-Hopf approach does not accurately model the open-end conductance for $k_o\ell \leq 2$ (air case). Thus, for the design of narrower microstrip antennas, the radiation characteristics would not be accurately modeled by the

Wiener-Hopf approach. This might be a critical factor, particularly if it is desired to design the microstrip antenna to operate over a specified frequency band. Clearly, the results point out the need to pursue further theoretical investigation of the open end conductance in the case of narrower microstrip configurations. Thus, the additional theoretical work should attempt to incorporate the effects of the finite width $k_o \ell$ along with the ratio ℓ/d in order to provide a more accurate conductance model.

REFERENCES

[1] D.C. Chang and E.F. Kuester, "Total and Partial Reflection from the End of a Parallel-Plate Waveguide with an Extended Dielectric Slab," Scientific Report 50, University of Colorado, December 1977.

[2] D.C. Chang, "Analytical Theory of an Unloaded Rectangular Microstrip Patch," IEEE Trans. Antennas Propagat., Vol. AP-29, No. 1, January 1981, pp. 54-62.

[3] P. Silvester and P. Benedek, "Equivalent Capacitance of Microstrip Open Circuits," IEEE Trans. M.T.T., Vol. MTT-20, No. 8, August 1972, pp. 511-516.

[4] A.G. Derneryd, "Linearly Polarized Microstrip Antennas," IEEE Trans. Antennas Propagat., Vol. AP-24, November 1976, pp. 846-851.

[5] E.F. Kuester, R.T. Johnk and D.C. Chang, "The Thin-Substrate Approximate for Reflection from the End of a Slab-Loaded Parallel-Plate Waveguide with Application to Microstrip Patch Antennas," To be published in IEEE Trans. Antennas Propagat., 1982.

[6] E.I. Nefedov and A.T. Fialkovskii, "Dispersion Characteristics of a Microstrip Waveguide," Sov. Phys. Dokl., Vol. 22, No. 4, 1977, pp. 448-450.

[7] C.P. Bates and R. Mittra, "Waveguide Excitation of Dielectric and Plasma Slabs," Radio Science, Vol. 3, No. 3, March 1968, pp. 251-266.

[8] D.C. Chang, private communication.

[9] R.E. Munson, "Conformal Microstrip Antennas and Microstrip Phased Arrays," IEEE Trans. on Antennas and Propagat., Vol. AP-22, January 1974, pp. 74-78.

[10] K. Carver and J. Mink, "Microstrip Antenna Technology," IEEE Trans. Antennas Propagat., Vol. AP-29, January 1981, pp. 2-24.

[11] E.O. Hammerstad, "Equations for Microstrip Circuit Design," Proc. 5th European Microwave Conf., 1975, pp. 268-272.

[12] B. Durvasula, "Cavity Measurements," M.S. Thesis, University of Colorado, 1981.

[13] I.J. Bahl and P. Bhartia, Microstrip Antennas. Dedham, Mass.: Artech House, 1980.

[14] K.C. Gupta, R. Garg, and I.J. Bahl, Microstrip Lines and Slotlines. Dedham, Mass.: Artech House, 1979.

[15] L. Lewin, Advanced Theory of Waveguides. London, Iliffe and Sons, 1951, Chapter 6.

[16] L.A. Wienstein, The Theory of Diffraction and the Factorization Method. Boulder, Colo.: Golem Press, 1969, Chapter 1.

[17] E.L. Ginzton, Microwave Measurements. New York: McGraw-Hill, 1957.

[18] C.G. Montgomery, Technique of Microwave Measurements. New York: McGraw-Hill, 1947, Chapter 8.

[19] S.I. Pearson and G.J. Maler, Introductory Circuit Analysis. New York: John Wiley and Sons, 1965, Chapter 4.

[20] C.T.A. Johnk, Engineering Electromagnetic Fields and Waves. New York: John Wiley and Sons, 1975, Chapter 10.

[21] R.F. Harrington, Time-Harmonic Electromagnetic Fields. New York: McGraw-Hill, 1961, Chapters 3 and 8.

[22] P. Silvester and M.S. Hsieh, "TEM Wave Properties of Microstrip Transmission Lines," Proc. IEE, Vol. 115, No. 1, 1968, pp. 43-48.

[23] Clark, F.M., Insulating Materials for Design and Engineering Practice. New York: John Wiley and Sons, 1962, pp. 593-599.

[24] L. Marin, "Modes on a Finite-Width Parallel-Plate Simulator," Sensor and Simulation Notes, Note 223, November 1977, pp. 32-43.

[25] I.S. Gradshteyn and I.M. Ryzhik, Tables of Integrals, Series, and Products. New York: Academic Press, 1980.

APPENDIX

APPENDIX A

APPROXIMATE EXPRESSIONS FOR THE WIENER-HOPF REFLECTION COEFFICIENT

A.1. The Normal Incidence Case

In this appendix, approximate expressions for $|\Gamma|$ and χ are derived. The first section deals with the normal incidence case in which $\phi = \alpha = 0$. A more general formula, valid for values of α not too close to 1 or n, is derived in the final section.

From Chapter II,

$$\hat{\Gamma} = e^{+j\chi} \tag{A.1}$$

where

$$\hat{\chi}(\alpha) = 2 \tan^{-1}\left(\sqrt{\frac{\alpha \tanh \Delta}{\alpha^2 - 1}}\right) + f_e(-\sqrt{n^2 - \alpha^2}) \tag{A.2}$$

$$f(-\sqrt{n^2 - \alpha^2}) = -\tan^{-1}\left(\sqrt{\frac{n^2 - \alpha^2}{\alpha^2 - 1}}\right) + \frac{2}{\pi}\sqrt{n^2 - \alpha^2}$$

$$\times \int^{\infty} \ell n\left[\frac{(1 + \varepsilon_r)u_o^2 \tanh u_n k_o d}{u_n(\varepsilon_r u_o + u_n \tanh u_n k_o d}\right] \frac{d\lambda}{\lambda^2 - (n^2 - \alpha^2)} \tag{A.3}$$

$$\Delta = \frac{\alpha}{\pi}\int_0^{\infty} \ell n\left[\frac{u_o n^2}{u_n}\left(\frac{u_n + u_o \tanh u_n k_o d}{n^2 u_o + u_n \tanh u_n k_o d}\right)\right] \frac{d\lambda}{\lambda^2 + \alpha^2} \tag{A.4}$$

In more compact form, (A.3) is written as

$$f_e(-\sqrt{n^2 - \alpha^2}) = -\tan^{-1}\left(\sqrt{\frac{n^2 - \alpha^2}{\alpha^2 - 1}}\right) + \frac{2}{\pi}\sqrt{n^2 - \alpha^2}\ \upsilon \qquad (A.5)$$

It is now assumed that $\alpha = 0$ and $(nk_od)^2 << 1$. With $u_n = \sqrt{\lambda^2 - n^2}$ and $u_o = \sqrt{\lambda^2 - 1}$, the integral in (A.5) becomes

$$\upsilon = \int_0^\infty \ell n\left[\frac{n^2 u_o^2 \tanh u_n k_o d}{\sqrt{n^2 - 1}\, k_o d\, u_n (n^2 u_o + u_n \tanh u_n k_o d)}\right] \frac{d\lambda}{\lambda^2 - n^2} \qquad (A.6)$$

Assuming that $\lambda_o^2 >> n^2$ and $\lambda' = \lambda k_o d$, Eq. (A.6) is split as follows:

$$\upsilon = \int_0^\infty \ell n\left[\frac{u_o}{\sqrt{n^2 - 1}}\right] \frac{d\lambda}{\lambda^2 - n^2} + \int^\infty \ell n\left[\frac{n^2 u_o}{n^2 u_o + u_n^2 k_o d}\right] \frac{d\lambda}{\lambda^2 - n^2}$$

$$+ k_o d \int_{\lambda_o'}^\infty \ell n\left[\frac{n^2 \tanh \lambda'}{\lambda'(n^2 + \tanh \lambda')}\right] \frac{d\lambda'}{\lambda'^2} \qquad (A.7)$$

The identity $\int_0^{\lambda_o} = \int_0^\infty - \int_{\lambda_o}^\infty$ is applied to the second integral of Eq. (A.7) which yields

$$\int_0^\infty \ell n\left[\frac{n^2 u_o^2}{\sqrt{n^2 - 1}\ (n^2 u_o + u_n^2 k_o d)}\right] \frac{d\lambda}{\lambda^2 - n^2}$$

$$+ k_o d \int_{\lambda_o'}^{\infty} \ell n \left[\frac{n^2 \tanh \lambda'}{\lambda'(n^2 + \tanh \lambda')} \right] \frac{d\lambda'}{\lambda'^2}$$

$$- \int_{\lambda_o}^{\infty} \ell n \left[\frac{n^2 u_o}{n^2 u_o + n^2 k_o d} \right] \frac{d\lambda}{\lambda^2} \qquad \text{(A.8)}$$

Since $\lambda_o^2 >> n^2$, u_o and u_n are replaced by λ in the third term of Eq. (A.8), and the substitution $\lambda' = k_o d\lambda$ is made. Combining the second term of (A.8) with the modified third term yields

$$\mathcal{V} = \int_0^{\infty} \ell n \left[\frac{n^2 u_o^2}{\sqrt{n^2 - 1}(n^2 u_o + u_n^2 k_o d)} \right] \frac{d\lambda}{\lambda^2 - n^2}$$

$$+ k_o d \int_{\lambda_o'}^{\infty} \ell n \left[\frac{\tanh \lambda'(n^2 + \lambda')}{\lambda'(n^2 + \tanh \lambda')} \right] \frac{d\lambda'}{\lambda'^2} \qquad \text{(A.9)}$$

Inspection of the second term of Eq. (A.9) reveals that a small λ' results in a term that is $O((k_o d)^2)$. This fact allows the lower limit λ_o' of the intergal to be replaced by zero. Thus, the modified expression is given by

$$\mathcal{V} \simeq \int_0^{\infty} \ell n \left[\frac{n^2 u_o^2}{\sqrt{n^2 - 1}\ (n^2 u_o + u_n^2 k_o d)} \right] \frac{d\lambda}{\lambda^2 - n^2}$$

$$+ k_o d \int_0^{\infty} \ell n \left[\frac{\tanh \lambda}{\lambda} \left(\frac{n^2 + \lambda}{n^2 + \tanh \lambda} \right) \right] \frac{d\lambda}{\lambda^2} \qquad \text{(A.10)}$$

$$= I_1 + I_2$$

where

$$I_1 = \int_0^{\infty} \ell n \left[\frac{n^2 u_o^2}{\sqrt{n^2 - 1}\,(n^2 u_o + u_n^2 k_o d)} \right] \frac{d\lambda}{\lambda^2 - n^2} \tag{A.11}$$

$$I_2 = \int_0^{\infty} \ell n \left[\frac{\tanh \lambda}{\lambda} \left(\frac{n^2 + \lambda}{n^2 + \tanh \lambda} \right) \right] \frac{d\lambda}{\lambda^2} \tag{A.12}$$

At this point, the evaluation of I_1 is considered. Fig. A.1a shows the contour of integration of I_1, in which the line with the x's denotes the square root branch cut of $u_o = \sqrt{\lambda^2 - 1}$. The zig-zag line in the figure is a logarithmic branch cut produced by the $n^2 u_o + u_n^2 k_o d$ term inside the logarithm of I_1. The utility of defining branch cuts in such a fashion is discussed later in this section. As a first step in the evaluation, the contour of I_1 is deformed to that of Fig. A.1b. Clearly, this deformation ignores the contribution between the branch points at $\lambda = 1$ and $\lambda = \lambda_e$, which is equivalent to ignoring the surface wave effects of the dielectric slab. For a small $k_o d$, the surface wave contribution to I_1 is quite small. In order to assess the order of magnitude of the surface wave contribution, consider the portion of the contour that is ignored after the deformation. The integral contribution of the surface waves is shown in Fig. A.2. From Eq. (A.11), the surface wave contribution is estimated to be

$$I_{sw} \propto j\pi \int_1^{\alpha_p} \frac{d\lambda}{\lambda^2 - n^2} \tag{A.13}$$

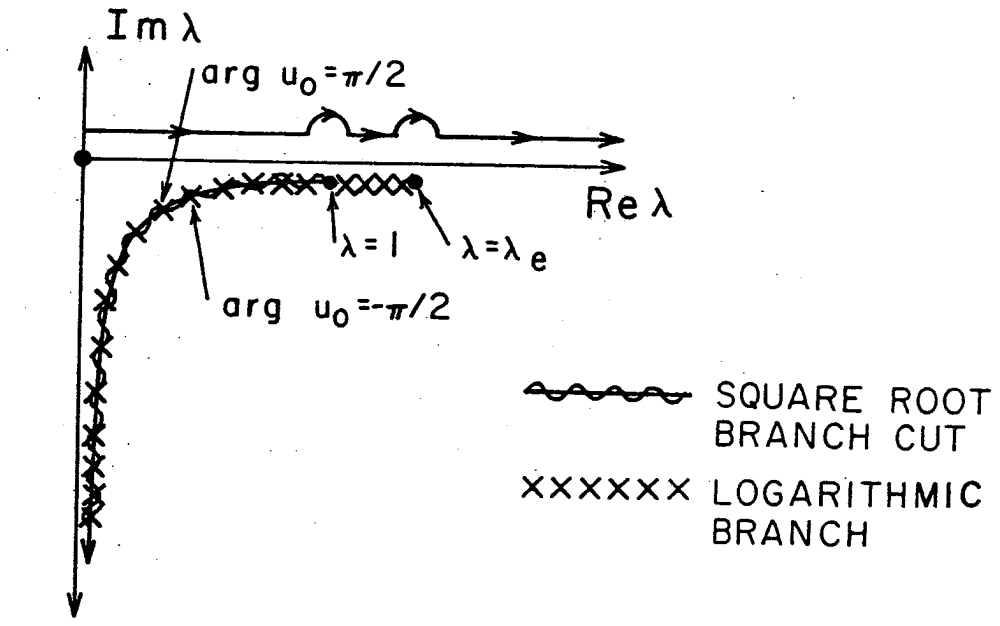
Im λ
arg $u_0 = \pi/2$
Re λ
λ = 1
$\lambda = \lambda_e$
arg $u_0 = -\pi/2$
SQUARE ROOT BRANCH CUT
XXXXXX LOGARITHMIC BRANCH

(a)

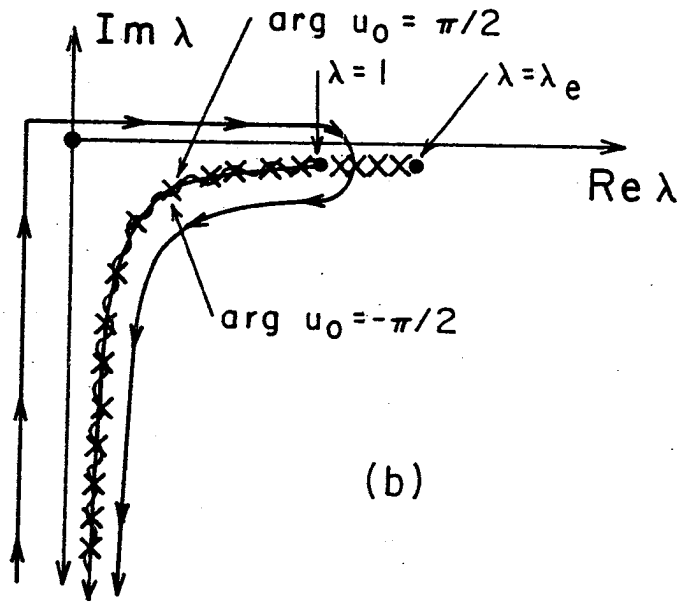
Im λ
arg $u_0 = \pi/2$
λ = 1
$\lambda = \lambda_e$
Re λ
arg $u_0 = -\pi/2$

(b)

Fig. A.1.

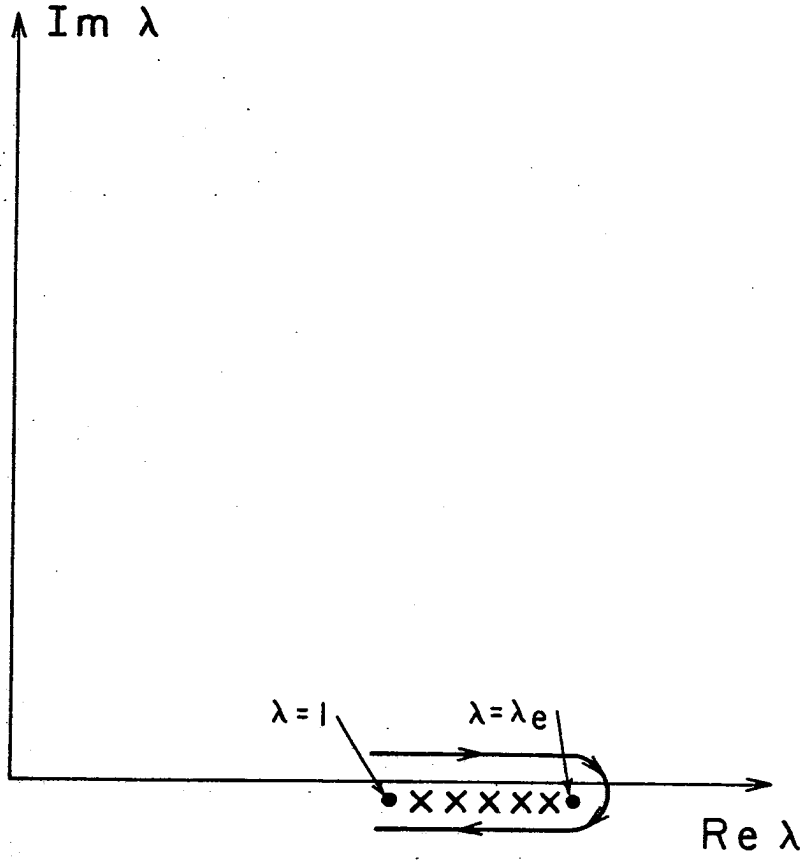

Fig. A.2.

where

$$\alpha_p \simeq 1 + \frac{(k_o d)^2 (n^2 - 1)^2}{2n^4}$$

α_p is determined by approximating the transcendental equation, (2.7). The evaluation of Eq. (A.13) indicates that

$$I_{sw} = 0\left(\frac{(k_o d)^2}{2n^3}\right) . \tag{A.14}$$

In the case of a thin substrate, Eq. (A.14) indicates that the effects of surface waves are indeed small. Thus, the deformation of the contour in Fig. A.1 appears to be a good approximation for small $k_o d$.

Having determined the effects of surface wave propagation, expressing I_1 along the contour of Fig. Alb yields

$$I_1 = \frac{1}{2}\int_0^1 \ell n\left[\frac{(n^2 - \lambda^2)k_o d + jn^2\sqrt{1 - \lambda^2}}{(n^2 - \lambda^2)k_o d - jn^2\sqrt{1 - \lambda^2}}\right]\frac{d\lambda}{\lambda^2 - n^2}$$

$$+ \frac{1}{2}\int_{-j\infty}^0 \ell n\left[\frac{(n^2 - \lambda^2)k_o d + jn^2\sqrt{1 - \lambda^2}}{(n^2 - \lambda^2)k_o d - jn^2\sqrt{1 - \lambda^2}}\right]\frac{d\lambda}{\lambda^2 - n^2} \tag{A.15}$$

Since $\tan^{-1}x = \frac{-j}{2}\ell n\left(\frac{1 + jx}{1 - jx}\right)$, Eq. (A.15) becomes

$$I_1 = j\int_0^1 \tan^{-1}\left(\frac{n^2\sqrt{1 - \lambda^2}}{(n^2 - \lambda^2)k_o d}\right)\frac{d\lambda}{\lambda^2 - n^2}$$

$$+ j \int_{-j\infty}^{0} \tan^{-1}\left(\frac{n^2\sqrt{1-\lambda^2}}{(n^2-\lambda^2)}\right)\frac{d\lambda}{\lambda^2-n^2} \qquad (A.16)$$

Making the substitution $\lambda = -jt$ in the second term of Eq. (A.16) and replacing the arctangent in the first term by its large argument expansion $\left(\frac{1}{k_o d} \gg 1\right)$ gives

$$I_1 = j \int_0^1 \left(\frac{\pi}{2} - \frac{(n^2-\lambda^2)k_o d}{n^2\sqrt{1-\lambda^2}}\right)\frac{d\lambda}{\lambda^2-n^2}$$

$$+ \int_0^\infty \tan^{-1}\left(\frac{n^2\sqrt{1+t^2}}{(n^2+t^2)k_o d}\right)\frac{dt}{t^2+n^2}$$

$$= j \int_0^1 \left(\frac{\pi}{2(\lambda^2-n^2)} + \frac{k_o d}{n^2\,1-\lambda^2}\right) d\lambda + k_o d\, I_3 \quad . \qquad (A.17)$$

The evaluation of the first term in Eq. (A.17) results in the following expression

$$I_1 = j\,\frac{\pi}{2}\left(\frac{-1}{2n}\,\ell n\left(\frac{n+1}{n-1}\right) + \frac{k_o d}{n^2}\right) + k_o d\, I_3 \quad .$$

Applying this equation to Eq. (A.10) yields

$$\mho = j\,\frac{\pi}{2}\left\{\frac{-1}{2n}\,\ell n\left(\frac{n+1}{n-1}\right) + \frac{k_o d}{n^2}\right\} + k_o d(I_2 + I_3) \quad . \qquad (A.18)$$

It is also noted that

$$\tan^{-1}\left(\frac{\sqrt{n^2-\alpha^2}}{\sqrt{\alpha^2-1}}\right) = \frac{-j}{2}\,\ell n\left(\frac{\sqrt{1-\alpha^2}+\sqrt{n^2-\alpha^2}}{\sqrt{1-\alpha^2}-\sqrt{n^2-\alpha^2}}\right) \quad . \qquad (A.19)$$

Substituting Eqs. (A.18) and (A.19) into (A.2) results in the reflection coefficient for the case of normal incidence,

$$\hat{\Gamma}(\alpha=0) = \exp\left(\frac{-k_o d}{n}\right) \exp\left\{j\left(\frac{2nk_o d}{\pi}\ (I_2 + I_3) - \frac{\pi}{2}\right)\right\} \qquad (A.20)$$

In order to evaluate I_3 of Eq. (A.17), the integral,

$$\frac{1}{k_o d}\int_0^\infty \tan^{-1}\left(\frac{n^2}{tk_o d}\right)\frac{dt}{t^2 + n^2}\ ,$$

is added to and subtracted from I_3, which gives

$$I_3 = \frac{1}{k_o d}\int_0^\infty \left[\tan^{-1}\left(\frac{n^2\sqrt{t^2+1}}{(t^2+n^2)k_o d}\right) - \tan^{-1}\left(\frac{n^2}{tk_o d}\right)\right]\frac{dt}{t^2+n^2}$$

$$+ \frac{1}{k_o d}\int_0^\infty \tan^{-1}\left(\frac{n^2}{tk_o d}\right)\frac{dt}{t^2+n^2}\ . \qquad (A.21)$$

Replacing the arctangent terms of the first integral in Eq. (A.21) by corresponding large argument expansions, and performing and integrating by parts on the second integral of this equation, results in the following equation:

$$I_3 = \int_0^\infty \left(\frac{t}{n^2} - \frac{(t^2+n^2)}{n\sqrt{t^2+1}}\right)\frac{dt}{t^2+n^2} + n\int_0^\infty \tan^{-1}\left(\frac{t}{n}\right)\frac{dt}{(k_o dt)^2 + n^4}\ . \qquad (A.22)$$

The direct evaluation of the first integral in Eq. (A.22) yields

$$I_3 = \frac{-1}{n^2} \ln 2n + n \int_0^\infty \tan^{-1}\left(\frac{t}{n}\right) \frac{dt}{(k_o dt)^2 + n^4} \quad .$$

Adding and subtracting a large argument term in this expression results in the following:

$$I_3 = \frac{-1}{n^2} \ln 2n + \frac{1}{n^3} \int_0^\infty \left[\tan^{-1}\left(\frac{t}{n}\right) - \frac{\frac{\pi}{2} t}{t + \frac{2n}{\pi}} \right]$$

$$+ \frac{n\pi}{4} \int_0^\infty \frac{t \, dt}{(t + \frac{2n}{\pi})\,(k_o dt)^2 + n^4} \quad . \qquad \text{(A.23)}$$

Expanding the second integral in Eq. (A.23) by the method of partial fractions yields

$$I_3 = \frac{-1}{n^2} \ln 2n + \frac{1}{n^3} \int_0^\infty \left(\tan^{-1}\left(\frac{t}{n}\right) - \frac{\frac{\pi}{2} t}{t + \frac{2n}{\pi}} \right) dt$$

$$+ \frac{\pi}{2n^3} \int_0^\infty \left[\frac{(k_o d)^2 \, \frac{2n}{\pi} \, t + n^4}{(k_o dt)^2 + n^4} - \left(\frac{2n}{\pi}\right) \frac{1}{t + \frac{2n}{\pi}} \right] dt \, . \qquad \text{(A.24)}$$

From an integration by parts,

$$\int_0^{t_o} \tan^{-1}\left(\frac{t}{n}\right) = t_o \tan^{-1}\left(\frac{t_o}{n}\right) - n \ln \left(\frac{\sqrt{t_o^2 + n^2}}{n} \right) \quad . \qquad \text{(A.25)}$$

Also,

$$\frac{\pi}{2} \int_0^{t_o} \frac{t \, dt}{t + \frac{2n}{\pi}} = \frac{\pi}{2} t_o - n \ln \left(t_o + \frac{2n}{\pi} \right) + n \ln \left(\frac{2n}{\pi} \right) \quad . \qquad \text{(A.26)}$$

Combining Eqs. (A.25) and (A.26) yields

$$\int_0^{t_o} \left[\tan^{-1}\left(\frac{t}{n}\right) - \frac{\frac{\pi}{2}\, t}{t + \frac{2n}{\pi}} \right] dt = t_o \tan^{-1}\left(\frac{t_o}{n}\right)$$

$$- n \ln\left(\frac{\sqrt{t_o^2 + n^2}}{n}\right) - \frac{\pi}{2} t_o - n \ln\left(t_o + \frac{2n}{\pi}\right) + n \ln\left(\frac{2n}{\pi}\right) . \tag{A.27}$$

In a similar fashion, the second term of Eq. (A.24) is given by

$$\int_0^{t_o} \left[\frac{(k_o d)^2 \left(\frac{2n}{\pi}\right) t + n^4}{(k_o d)^2 t^2 + n^4} - \frac{2n}{\pi} \frac{1}{t + \frac{2n}{\pi}} \right] dt = \frac{n^2}{k_o d} \tan^{-1}\left(\frac{k_o d\, t_o}{n^4}\right)$$

$$+ \frac{2n}{\pi} \ln (k_o d\, t_o) - \frac{2n}{\pi} \ln t_o - \frac{4n}{\pi} \ln (n) + \frac{2n}{\pi} \ln\left(\frac{2n}{\pi}\right) . \tag{A.28}$$

Applying Eqs. (A.27) and (A.28) to Eqs. (A.24) and taking the limit as $t_o \to \infty$ yields

$$I_3 = \frac{\pi}{4k_o dn} - \frac{1}{n^2} + \frac{1}{n^2} \ln\left(\frac{k_o d}{2n^2}\right) . \tag{A.29}$$

In order to complete the approximate expression for $\hat{\Gamma}$, I_2 must be evaluated. From Eq. (A.12),

$$I_2 = \int_0^{\infty} \ln \left[\left(\frac{\tanh \lambda}{\lambda}\right) \left(\frac{n^2 + \lambda}{n^2 + \tanh \lambda}\right) \right] \frac{d\lambda}{\lambda^2} .$$

Integrating this equation by parts gives

$$I_2 = \int_0^\infty \left[\frac{1}{n^2 + \lambda} - \frac{1}{\lambda} + \frac{2e^{-2\lambda}}{1 - e^{-2\lambda}} + \frac{2\delta_e e^{-2\lambda}}{1 + \delta_e e^{-2\lambda}} \right] \frac{d\lambda}{\lambda} \qquad (A.30)$$

where

$$\delta_e = \frac{n^2 - 1}{n^2 + 1} \quad .$$

Eq. (A.30) is now modified by adding and subtracting $\int \frac{d\lambda}{\lambda}$, and applying a binomial expansion to the last term in the integrand. Writing the resulting equation in limiting form yields

$$I_2 = \lim_{a \to 0} \left\{ \int_0^\infty \left[1 - \frac{1}{\lambda} + \frac{2e^{-2\lambda}}{1 - e^{-2\lambda}} \right] \frac{e^{-2a\lambda} d\lambda}{\lambda} + \int_0^\infty \left[\frac{-\lambda}{n^2(\lambda + n^2)} + 2 \sum_{m=1}^{\infty} (-\delta_e)^m (1 - e^{-2m\lambda}) \right] \frac{e^{2a\lambda} d\lambda}{\lambda} \right\} . \qquad (A.31)$$

From a table of integrals [25], the first integral in Eq. (A.31) is given by

$$2 \int_0^\infty \left[1 - \frac{1}{\lambda} - \frac{2e^{-2\lambda}}{1 - e^{-2\lambda}} \right] \frac{e^{-2a\lambda} d\lambda}{\lambda} = 2\Gamma(a) - 2(a - \tfrac{1}{2}) \ln a - \ln 2\pi \qquad (A.32)$$

where Γ denotes the gamma function. For small a, the right side of Eq. (A.32) becomes

$$-\ln(a) - \ln(2\pi) \quad .$$

From the same integral tables,

$$\frac{-1}{n^2}\int \frac{e^{-2a\lambda}d\lambda}{\lambda + n^2} = \frac{e^{-2n^2}}{n^2}\,Ei(-2an^2) \quad . \tag{A.34}$$

In Eq. (A.34), E_i denotes the exponential integral function. The small agrument expansion is

$$\frac{1}{n^2}\left[\gamma + \ell n\ 2an^2\right] \quad \text{where} \quad \gamma = 0.57721\ldots \quad . \tag{A.35}$$

Finally,

$$2\sum_{m=1}^{\infty}(-\delta_e)^m \int_0^{\infty}\left(e^{-2a\lambda} - e^{-2(a+m)\lambda}\right)\frac{d\lambda}{\lambda}$$

$$= 2\sum_{m=1}^{\infty}(-\delta_e)^m\,\ell n\ m + \frac{n^2-1}{n^2}\,\ell n\ a \quad . \tag{A.36}$$

Applying Eqs. (A.33), (A.35), and (A.36) to Eq. (A.31) yields

$$I_2 = \ell n\left(\frac{1}{2\pi}\right) + \frac{1}{n^2}\left(\ell n\ 2n^2 + \gamma\right) + 2Q_o \tag{A.37}$$

where

$$Q_o = \sum_{m=1}^{\infty}(-\delta_e)^m\,\ell n\ m \quad .$$

Substituting Eqs. (A.37) and (A.29) into Eq. (A.20) results in the following reflection coefficient for the normal incidence case:

$$\hat{\Gamma} = |\Gamma_o|e^{i\chi_o} \tag{A.38}$$

where

$$|\Gamma_o| = \exp\left(\frac{-k_o d}{n}\right)$$

$$\chi_o = \frac{2nk_o d}{\pi}\left[2Q_o - \ell n\, 2\pi + \frac{1}{n^2}(\ell n\, k_o d + \gamma - 1)\right]$$

in agreement with Eq. (2.19).

A.2. The General Case

This section deals with the evaluation of $\hat{\Gamma}$ in the range $0 < \alpha < n$, in which α is not too close to $\alpha = 1$ or $\alpha = n$. The first integral to be evaluated is Δ. From Eq. (A.4),

$$\Delta = \frac{\alpha}{\pi}\int_0^\infty \ell n\left[\frac{u_o n^2}{u_n}\left(\frac{u_n + u_o \tanh u_n k_o d}{n^2 u_o + u_n \tanh u_n k_o d}\right)\right]\frac{d\lambda}{\lambda^2 + \alpha^2} \quad .$$

Adding and subtracting the integral,

$$\frac{\alpha}{\pi}\int_0^\infty \frac{u_o(1 + n^2)\tanh u_n k_o d}{\lambda^2 + \alpha^2}\, d\lambda \quad ,$$

yields

$$\Delta = \frac{\alpha}{\pi}\int_0 \left[\ell n\left(\frac{u_o^2(n^2 + 1)\tanh u_n k_o d}{u_n(n^2 u_o + u_n \tanh u_n k_o d}\right)\right.$$

$$\left. + \ell n\left(\frac{n^2(u_n + u_o \tanh u_n k_o d}{u_n(n^2 + 1)\tanh u_n k_o d}\right)\right] \frac{d\lambda}{\lambda^2 + \alpha^2}$$

$$= \Delta_e + \Delta_m \tag{A.39}$$

where

$$\Delta_e = \frac{\alpha}{\pi}\int_0^{\infty} \ell n\left(\frac{u_o^2(n^2+1)\tanh u_n k_o d)}{u_n(n^2 u_o + u_n \tanh u_n k_o d}\right)\frac{d\lambda}{\lambda^2+\alpha^2} \tag{A.40}$$

$$\Delta_m = \frac{\alpha}{\pi}\int_0^{\infty} \ell n\left(\frac{n^2(u_n + u_o \tanh u_n k_o d)}{u_o(n^2+1)\tanh u_n k_o d}\right)\frac{d\lambda}{\lambda^2+\alpha^2} \tag{A.41}$$

Splitting the integral (A.41) into parts, with $\lambda_o^2 >> \alpha^2$ and $(nk_o d)^2 << 1$ yields

$$\Delta_m \simeq \frac{\alpha}{\pi}\int_0^{\lambda_o} \ell n\left(\frac{n^2(1+u_o k_o d)}{(n^2+1)u_o k_o d}\right)\frac{d\lambda}{\lambda^2+\alpha^2}$$

$$+ \frac{\alpha}{\pi}\int_{\lambda_o}^{\infty} \ell n\left(\frac{n^2(1+\tanh\lambda k_o d)}{(n^2+1)\tanh\lambda k_o d}\right)\frac{d\lambda}{\lambda^2} \quad . \tag{A.42}$$

Applying the identity $\int_0^{\lambda_o} = \int_0^{\infty} - \int_{\lambda_o}^{\infty}$ to the first term of Eq. (A.42) and replacing the lower limit λ_o by zero results in the following:

$$\Delta_m = \Delta_{m1} + \Delta_{m2} \tag{A.43}$$

where

$$\Delta_{m1} = \frac{\alpha}{\pi}\int_0^{\infty} \ell n\left(\frac{n^2(1+u_o k_o d)}{u_o k_o d(n^2+1)}\right)\frac{d\lambda}{\lambda^2+\alpha^2} \tag{A.44}$$

$$\Delta_{m2} = \frac{\alpha}{\pi} \int_0^{\infty} \ell n \left[\left(\frac{1 + \tanh \lambda\, k_o d}{\tanh \lambda\, k_o d} \right) \left(\frac{\lambda\, k_o d}{1 + \lambda\, k_o d} \right) \right] \frac{d\lambda}{\lambda^2} \quad . \tag{A.45}$$

Consider now the integral of Eq. (A.44). Utilizing the symmetry properties of the integrand, the range of integration of Δ_{m1} can be doubled to yield

$$\Delta_{m1} = \frac{\alpha}{2\pi} \int_{-\infty}^{\infty} \ell n \left(\frac{n^2(1 + u_o k_o d)}{u_o k_o d(n^2 + 1)} \right) \frac{d\lambda}{\lambda^2 + \alpha^2} \quad . \tag{A.46}$$

In order to evaluate Eq. (A.46), the contour of integration is deformed to that of Fig. A.3. The branch cut, which has a branch point at $\lambda = -j\sqrt{\alpha^2 - 1}$, is represented as a square root branch cut. A pole is located at $\lambda = -j\alpha$, and it contributes to the integral in the form of two half residues. When the identity,

$$j2 \tan^{-1} x = \ell n \left(\frac{1 + jx}{1 - jx} \right),$$

and the substitution $\lambda = j\tau'$ are applied to the deformed version of Eq. (A.46), the following integral results:

$$\Delta_{m1} = \frac{\alpha}{\pi} \int_{\sqrt{\alpha^2 - 1}}^{\infty} \left[\frac{\pi}{2} - \tan^{-1}(k_o d \sqrt{1 - \alpha^2 + \tau'^2}) \right] \frac{d\tau'}{\alpha^2 - \tau'^2}$$

$$+ j\pi \left(\frac{\alpha}{\pi} \right) \lim_{\tau \to \alpha} \left\{ \frac{(\alpha - \tau')}{(\alpha^2 - \tau'^2)} \left[\frac{\pi}{2} - \tan^{-1}(k_o d \sqrt{1 - \alpha^2 + \tau'^2}) \right] \right\} \tag{A.47}$$

The limit in the above equation is a result of the residue

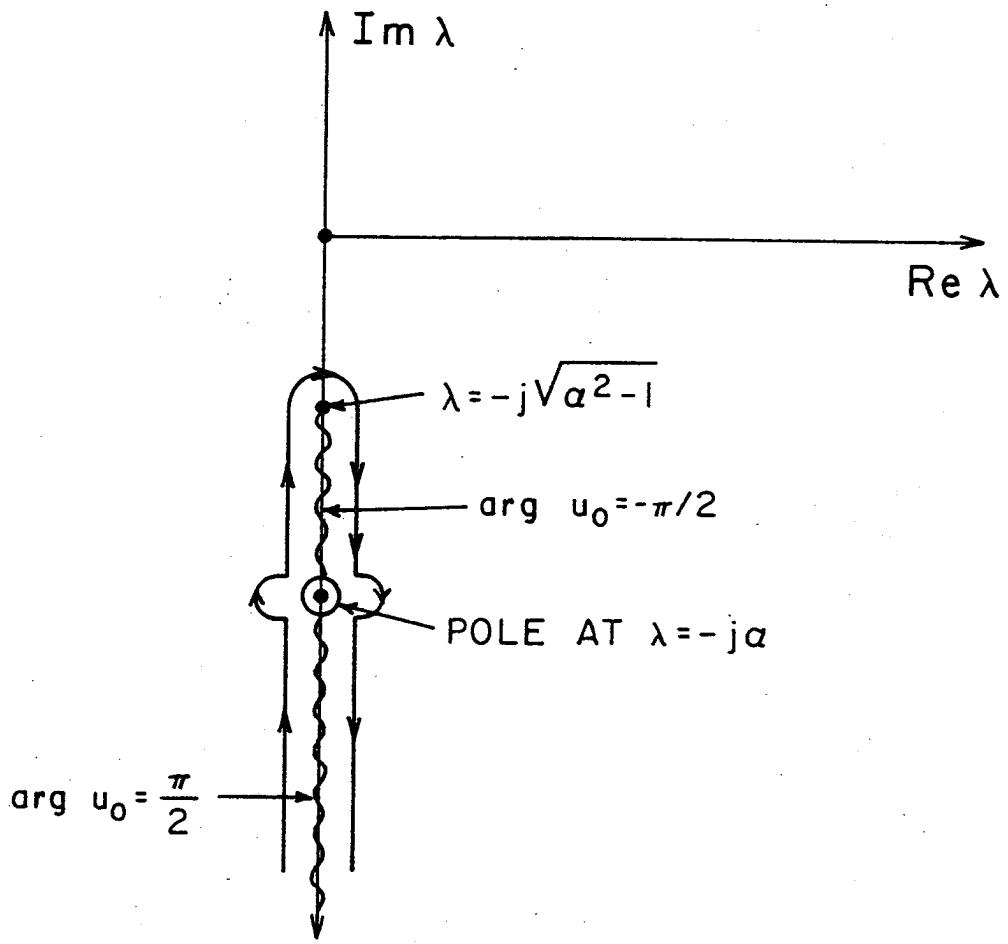

Fig. A.3.

contribution of the pole at $\lambda = -j\alpha$. When the substitution $\tau = \sqrt{1 - \alpha^2 + \tau'^2}$ is employed in Eq. (A.47), the expression for Δ_{ml} becomes

$$\Delta_{ml} = \frac{\alpha}{\pi} \int_0^{\infty} \left[\frac{\pi}{2} - \tan^{-1}(k_o d\tau) \right] \frac{\tau \, d\tau}{(1 - \tau^2)\sqrt{\tau^2 + \alpha^2 - 1}}$$

$$+ \frac{j}{2} \left[\frac{\pi}{2} - k_o d \right] \quad . \tag{A.48}$$

The two terms of the integral in Eq. (A.48) must now be evaluated. For the first term,

$$\frac{\alpha}{2} \int_0^{\infty} \frac{\tau \, d\tau}{(1 - \tau^2)\sqrt{\tau^2 - \alpha^2 - 1}} = \frac{-1}{4} \ln \left(\frac{\alpha + \sqrt{\alpha^2 - 1}}{\alpha - \sqrt{\alpha^2 - 1}} \right) \quad . \tag{A.49}$$

The second term has the following equivalent representation:

$$\frac{\alpha}{\pi} \int_0^{\infty} \frac{\tan^{-1}(k_o d\tau)\tau \, d\tau}{(1 - \tau^2)\sqrt{\tau^2 + \alpha^2 - 1}} = \lim_{\tau_o \to \infty} \int_0^{\tau_o} (\tan^{-1}(k_o d\tau)$$

$$- k_o d\tau) \frac{d\tau}{(1 - \tau^2)\sqrt{\tau^2 + \alpha^2 - 1}}$$

$$- k_o d \int_0^{\tau_o} \left(1 - \frac{1}{1 - \tau^2} \right) \frac{d\tau}{\sqrt{\tau^2 + \alpha^2 - 1}} \tag{A.50}$$

In the first integral on the right side of Eq. (A.50), $\tan^{-1}(k_o d\tau) - k_o d\tau \simeq 0$ when $k_o d\tau \ll 1$. Thus, the first integral of Eq. (A.50) can be written as

$$- \int_0^{\tau_o} (\tan^{-1}(k_o d\tau) - k_o d\tau) \frac{d\tau}{\tau^2} \quad . \tag{A.51}$$

Making the substitution $\tau = \sqrt{\alpha^2 - 1} \sinh t$ in the second integral of Eq. (A.50), and substituting (A.51) yields

$$\frac{\alpha}{\pi} \int_0^{\infty} \frac{\tan^{-1}(k_o d\tau)\tau \, d\tau}{(1 - \tau^2)\sqrt{\tau^2 + \alpha^2 - 1}} = \lim_{\tau_o \to 0} \left[- \int_0^{\tau_o} (\tan^{-1}(k_o d\tau) \right.$$

$$\left. - k_o d\tau) \frac{d\tau}{\tau^2} - \int_0^{\sinh^{-1}\left(\frac{\tau_o}{\sqrt{\alpha^2-1}}\right)} \left(1 - \frac{2}{(\alpha^2+1)-(\alpha^2-1)\cosh 2t}\right) dt \right] \tag{A.52}$$

From Gradshteyn [25] with $b^2 < a^2$,

$$\int_0^{\infty} \frac{dx}{a + b \cosh x} = \frac{1}{\sqrt{a^2 - b^2}} \ln \left(\frac{a + b + \sqrt{a^2 - b^2}}{a + b - \sqrt{a^2 - b^2}} \right) \tag{A.53}$$

Integrating the first integral on the right side of Eq. (A.52) by parts and applying Eq. (A.53) to the second integral yields the following result:

$$\frac{\alpha}{\pi} \int_0^{\infty} \frac{\tan^{-1}(k_o d\tau)\tau \, d\tau}{(1 - \tau^2)\sqrt{\tau^2 + \alpha^2 - 1}} = -k_o d + (k_o d) \ln \left(\frac{k_o d \sqrt{\alpha^2 - 1}}{2} \right)$$

$$+ \frac{k_o d}{2} \ln \left(\frac{1 + \alpha}{1 - \alpha} \right) \quad . \tag{A.54}$$

Substituting Eqs. (A.54) and (A.49) into (A.48) yields

$$\Delta_{m1} = \frac{\alpha}{\pi}\left\{\frac{-\pi}{4\alpha}\,\ell n\left(\frac{\alpha+\sqrt{\alpha^2-1}}{\alpha-\sqrt{\alpha^2-1}}\right) + k_o d + k_o d\,\ell n\left(\frac{2}{k_o d\sqrt{\alpha^2-1}}\right)\right.$$

$$\left. - \frac{k_o d}{2\alpha}\,\ell n\left(\frac{1+\alpha}{1-\alpha}\right)\right\} + \frac{j}{2}\left(\frac{\pi}{2} - k_o d\right) \quad . \tag{A.55}$$

Now consider Δ_e as given in Eq. (A.40). Splitting the integral as before gives

$$\Delta_e \simeq \frac{\alpha}{\pi}\int_0^{\lambda_o} \ell n\left[\frac{u_o^2(n^2+1)k_o d}{n^2 u_o + u_n^2 k_o d}\right]\frac{d\lambda}{\lambda^2+\alpha^2}$$

$$+ \int_{\lambda_o}^{\infty} \ell n\left[\frac{(n^2+1)\tanh(\lambda k_o d)}{n^2 + \tanh(\lambda k_o d)}\right]\frac{d\lambda}{\lambda^2} \quad . \tag{A.56}$$

Modifying Eq. (A.56) in the same manner as Eq. (A.7) yields

$$\Delta_e = \Delta_{e1} + \Delta_{e2} \tag{A.57}$$

where

$$\Delta_{e1} = \frac{\alpha}{\pi}\int_0^{\infty} \ell n\left[\frac{u_o^2(n^2+1)k_o d}{n^2 u_o + u_n^2 k_o d}\right]\frac{d\lambda}{\lambda^2+\alpha^2} \tag{A.58}$$

$$\Delta_{e2} = \frac{\alpha}{\pi}\int_0^{\infty} \ell n\left[\frac{(n^2 + k_o d)\tanh \lambda k_o d}{(n^2 + \tanh \lambda k_o d)\, k_o d}\right]\frac{d\lambda}{\lambda^2} \quad . \tag{A.59}$$

The contour of Eq. (A.58) is now deformed to that of Fig. A.3.

Following the same steps that have already been used to derive Eq. (A.47), Eq. (A.58) becomes

$$\Delta_{el} = \frac{\alpha}{\pi} \int_{\sqrt{\alpha^2-1}}^{\infty} \tan^{-1}\left(\frac{n^2\sqrt{1-\alpha^2+\tau^2}}{(n^2-\alpha^2+\tau^2)k_o d}\right)\frac{d\tau}{\tau^2-\alpha^2} - \frac{j}{2}\left(\frac{\pi}{2} - k_o d\right).$$

Adding and subtracting a term in the above equation yields

$$\Delta_{el} = \frac{\alpha}{\pi} \int_{\sqrt{\alpha^2-1}}^{\infty} \left[\tan^{-1}\left(\frac{n^2\sqrt{1-\alpha^2+\tau^2}}{(n^2-\alpha^2+\tau^2)k_o d}\right) - \tan^{-1}\left(\frac{n^2}{k_o d\tau}\right)\right]\frac{d\tau}{\tau^2-\alpha^2}$$

$$+ \int_{\sqrt{\alpha^2-1}}^{\infty} \tan^{-1}\left(\frac{n^2}{\tau k_o d}\right)\frac{d\tau}{\tau^2-\alpha^2} - \frac{j}{2}\left(\frac{\pi}{2} - k_o d\right) \quad . \qquad (A.60)$$

Replacing the arctangent terms in the first integral of Eq. (A.60) by large argument expansions produces the following result:

$$\Delta_{el} = \frac{k_o d\alpha}{\pi} \int_{\sqrt{\alpha^2-1}}^{\infty} \left(\tau - \frac{(n^2-\alpha^2+\tau^2)}{\sqrt{1-\alpha^2+\tau^2}}\right)\frac{d\tau}{\tau^2-\alpha^2}$$

$$\frac{\alpha}{\pi} \int_{\sqrt{\alpha^2-1}}^{\infty} \tan^{-1}\left(\frac{n^2}{\tau k_o d}\right)\frac{d\tau}{\tau^2-\alpha^2} - \frac{j}{2}\left(\frac{\pi}{2} - k_o d\right) \quad . \qquad (A.61)$$

Upon integrating the second integral by parts, Eq. (A.61) becomes

$$\Delta_{el} = \frac{1}{2\pi} \ell n\left(\frac{\alpha+\sqrt{\alpha^2-1}}{\alpha-\sqrt{\alpha^2-1}}\right) \tan^{-1}\left(\frac{n^2}{\sqrt{\alpha^2-1}\, k_o d}\right)$$

$$+ k_o d(I_4 + I_5) - j\left(\frac{\pi}{2} - k_o d\right) \qquad (A.62)$$

where

$$I_4 = \int_{\sqrt{\alpha^2-1}}^{\infty} \left(\frac{\tau}{\tau^2 - \alpha^2} - \frac{n^2}{\sqrt{1 - \alpha^2 + \tau^2(\tau^2 - \alpha^2)}} - \frac{1}{\sqrt{1 - \alpha^2 - \tau^2}} \right) d\tau \tag{A.63}$$

$$I_5 = \frac{-n^4}{2} \int_{\sqrt{\alpha^2-1}}^{\infty} \ln \left(\frac{\tau + \alpha}{|\tau - \alpha|} \right) \frac{d\tau}{(k_o d)^2 \tau^2 + n^4} \tag{A.64}$$

Integrating the first and third terms in Eq. (A.63) directly and making the change of variable $\tau = \sqrt{\alpha^2 - 1} \cosh t$ in the second term produces the following equation:

$$I_4 = \frac{1}{2} \ln(|\tau^2 - \alpha^2|) \Big|_{\sqrt{\alpha^2-1}}^{\infty} - \ln(\tau + \sqrt{\tau^2 + 1 - \alpha^2}) \Big|_{\sqrt{\alpha^2-1}}^{\infty}$$

$$- n^2 \int_0^{\infty} \frac{dt}{(\alpha^2 - 1)(\frac{1}{2} + \frac{1}{2} \cosh 2t) - \alpha^2} \quad . \tag{A.65}$$

From Gradshteyn [25],

$$\int_0^{\infty} \frac{dt}{(\alpha^2 - 1)\cosh t - (\alpha^2 - 1)} = \frac{1}{2} \ln \left(\frac{\alpha - 1}{\alpha + 1} \right) \quad . \tag{A.66}$$

Upon making the substitution $t' = 2t$, the third term of Eq. (A.65) is evaluated by means of Eq. (A.66). After terms are combined,

$$I_4 = \frac{n^2}{2\alpha} \ln \left(\frac{\alpha + 1}{\alpha - 1} \right) + \ln \left(\frac{\sqrt{\alpha^2 - 1}}{2} \right) \quad . \tag{A.67}$$

In order to evaluate I_5, a term is added and subtracted in Eq. (A.64) to give

$$I_5 = \frac{-n^4}{2} \int_{\sqrt{\alpha^2-1}}^{\infty} \left[\ln \left(\frac{\tau + \alpha}{|\tau - \alpha|} \right) - \frac{2\alpha}{\tau} \right] \frac{d\tau}{(k_o d\tau)^2 + n^4}$$

$$- n^4 \int_{\sqrt{\alpha^2-1}}^{\infty} \frac{1}{(k_o d\tau)^2 + n^4} \frac{d\tau}{\tau} \quad . \tag{A.68}$$

Since $k_o d \ll 1$,

$$\frac{1}{(k_o d\tau)^2 + n^4} \ln \left(\frac{\tau + \alpha}{|\tau - \alpha|} \right) \simeq \frac{1}{n^4} \ln \left(\frac{\tau + \alpha}{|\tau - \alpha|} \right) . \tag{A.69}$$

Also,

$$\frac{n^4}{\tau \left((k_o d\tau)^2 + n^4 \right)} = 1 - \frac{(k_o d)^2 \tau^2}{(k_o d)^2 \tau^2 + n^4} \quad . \tag{A.70}$$

Applying Eqs. (A.69) and (A.70) to (A.68) yields

$$I_5 = \frac{-1}{2\alpha} \int_{\sqrt{\alpha^2-1}}^{\infty} \ln \left(\frac{\tau + \alpha}{|\tau - \alpha|} \right) d\tau + (k_o d)^2 \int_{\sqrt{\alpha^2-1}}^{\infty} \frac{\tau \, d\tau}{(k_o d)^2 \tau^2 + n^4} \quad . \tag{A.71}$$

Integrating the first term of Eq. (A.71) by parts and integrating the second term directly results in the following expression for I_5:

$$I_5 = -1 + \frac{1}{2\alpha}\sqrt{\alpha^2 - 1}\ \ln\left(\frac{\alpha + \sqrt{\alpha^2 - 1}}{\alpha - \sqrt{\alpha^2 - 1}}\right) + \ln\frac{k_o d}{n^2} \quad . \tag{A.72}$$

Substituting Eqs. (A.72) and (A.67) into (A.62) yields

$$\Delta_{e1} = \frac{1}{4}\ln\left(\frac{\alpha + \sqrt{\alpha^2 - 1}}{\alpha - \sqrt{\alpha^2 - 1}}\right) + \frac{k_o d\alpha}{\pi}\left[-1 + \ln\left(\frac{k_o d\sqrt{\alpha^2 - 1}}{2n^2}\right)\right.$$

$$\left. + \frac{n^2}{2\alpha}\ln\left(\frac{\alpha + 1}{\alpha - 1}\right)\right] - \frac{j}{2}\left[\frac{\pi}{2} - k_o d\right] \quad . \tag{A.73}$$

Adding Eqs. (A.55) and (A.73) produces the following result:

$$\Delta_{e1} + \Delta_{m1} = \frac{\alpha k_o d}{\pi}\left[\left(1 - \frac{1}{n^2}\right)\left(\ln\left(\frac{2}{k_o d\sqrt{\alpha^2 - 1}}\right) - \frac{2}{n^2}\ln(n)\right)\right] . \tag{A.74}$$

The final step in deriving the approximate involves the evaluation of the sum $\Delta_{m2} + \Delta_{e2}$. Adding Eqs. (A.59) and (A.45) yields

$$\Delta_{m2} + \Delta_{e2} = \frac{\alpha k_o d}{\pi}\int_0^\infty \ln\left[\frac{(\lambda + n^2)}{(\lambda + 1)}\left(\frac{2}{n^2 + 1}\right)\left(\frac{1}{1 + \delta_e e^{-2\lambda}}\right)\right]\frac{d\lambda}{\lambda^2} \tag{A.75}$$

where

$$\delta_e = \frac{n^2 - 1}{n^2 - 1} \quad .$$

Integrating Eq. (A.75) by parts, applying the binomial theorem, and expressing the resulting integral in the form of a limit obtains

$$\Delta_{m2} + \Delta_{e2} = \frac{\alpha k_o d}{\pi} \lim_{a \to 0} \left\{ \int_0^\infty \left[\left(\frac{1}{\lambda + 1} - \frac{\frac{1}{n^2}}{\lambda + n} \right) \right.\right.$$

$$\left.\left. - 2 \sum_{m=1}^{\infty} (-\delta_e)^m \left(\frac{e^{-2m\lambda} - 1}{\lambda} \right) \right] e^{-2a\lambda} \, d\lambda \right\} \qquad \text{(A.76)}$$

Utilizing the integral tables [25], each term of Eq. (A.76) is evaluated. After combining terms and taking the limit, the resulting expression is

$$\Delta_{m2} + \Delta_{e2} = \frac{\alpha k_o d}{\pi} \left[\gamma \left(1 - \frac{1}{n^2} \right) - \left(1 - \frac{1}{n^2} \right) \ell n \; 2 + \frac{2}{n^2} \ell n \; n + 2Q_o \right] \qquad \text{(A.77)}$$

The formula for Δ is now obtained by adding Eqs. (A.77) and (A.74):

$$\Delta = \frac{\alpha k_o d}{\pi} \left\{ \left(1 - \frac{1}{n^2} \right) \left[1 - \gamma + \ell n \left(\frac{1}{k_o d \sqrt{\alpha^2 - 1}} \right) + 2Q_o \right] \right\} . \qquad \text{(A.78)}$$

Having derived the approximate expression for Δ, an approximate formula for the $\mho$ integral is now derived. As a first step, the integral (A.6) in split into two parts in precisely the same manner as before, Therefore,

$$\mho \simeq I_6 + k_o d \; I_2 \qquad \text{(A.79)}$$

where

$$I_6 = \int_0^\infty \ell n \left[\frac{n^2 u_o^2}{\sqrt{n^2 - 1}(n^2 u_o + u_n^2 k_o d} \right] \frac{d\lambda}{\lambda^2 - (n^2 - \alpha^2)} \qquad \text{(A.80)}$$

and

$$I_2 = k_o d \int_0^\infty \ell n \left(\frac{\tanh \lambda}{\lambda}\right)\left(\frac{n^2 + \lambda}{n^2 + \tanh \lambda}\right)\frac{d\lambda}{\lambda^2} \quad .$$

I_2 has already been evaluated, and it is given by Eq. (A.37). In order to evaluate the integral I_6, the range of integration is changed to $-\infty < \lambda < \infty$, and the contour is then deformed to that of Fig. A.4. In this figure, the only singularity that is shown is a square root branch cut with a branch point at $\lambda = -j\sqrt{\alpha^2 - 1}$. Substituting an arctangent function for the logarithmic integrand and making the substitution $\tau = j\lambda$ yields

$$I_6 = \int_{\sqrt{\alpha^2-1}}^\infty \tan^{-1}\left(\frac{n^2\sqrt{\tau^2 + 1 - \alpha^2}}{k_o d(\tau^2 + n^2 - \alpha^2)}\right)\frac{d\tau}{\tau^2 + n^2 - \alpha^2} \quad . \qquad \text{(A.81)}$$

Adding and subtracting a term in Eq. (A.81) obtains the modified integral

$$\int_{\sqrt{\alpha^2-1}}^\infty \left[\tan^{-1}\left(\frac{n^2\sqrt{\tau^2 + 1 - \alpha^2}}{k_o d(\tau^2 + n^2 - \alpha^2)}\right) - \tan^{-1}\left(\frac{n^2}{\tau k_o d}\right)\right]\frac{d\tau}{\tau^2 + n^2 - \alpha^2}$$

$$+ \int_{\sqrt{\alpha^2-1}}^\infty \tan^{-1}\left(\frac{n^2}{\tau k_o d}\right)\frac{d\tau}{\tau^2 + n^2 - \alpha^2} \quad . \qquad \text{(A.82)}$$

Making use of the integral identity

$$\int_{\sqrt{\alpha^2-1}}^\infty = \int_0^\infty - \int_0^{\sqrt{\alpha^2-1}}$$

and the large argument expansion $\tan^{-1} x = \frac{\pi}{2} - \frac{1}{x}$ in Eq. (A.82) produces the result

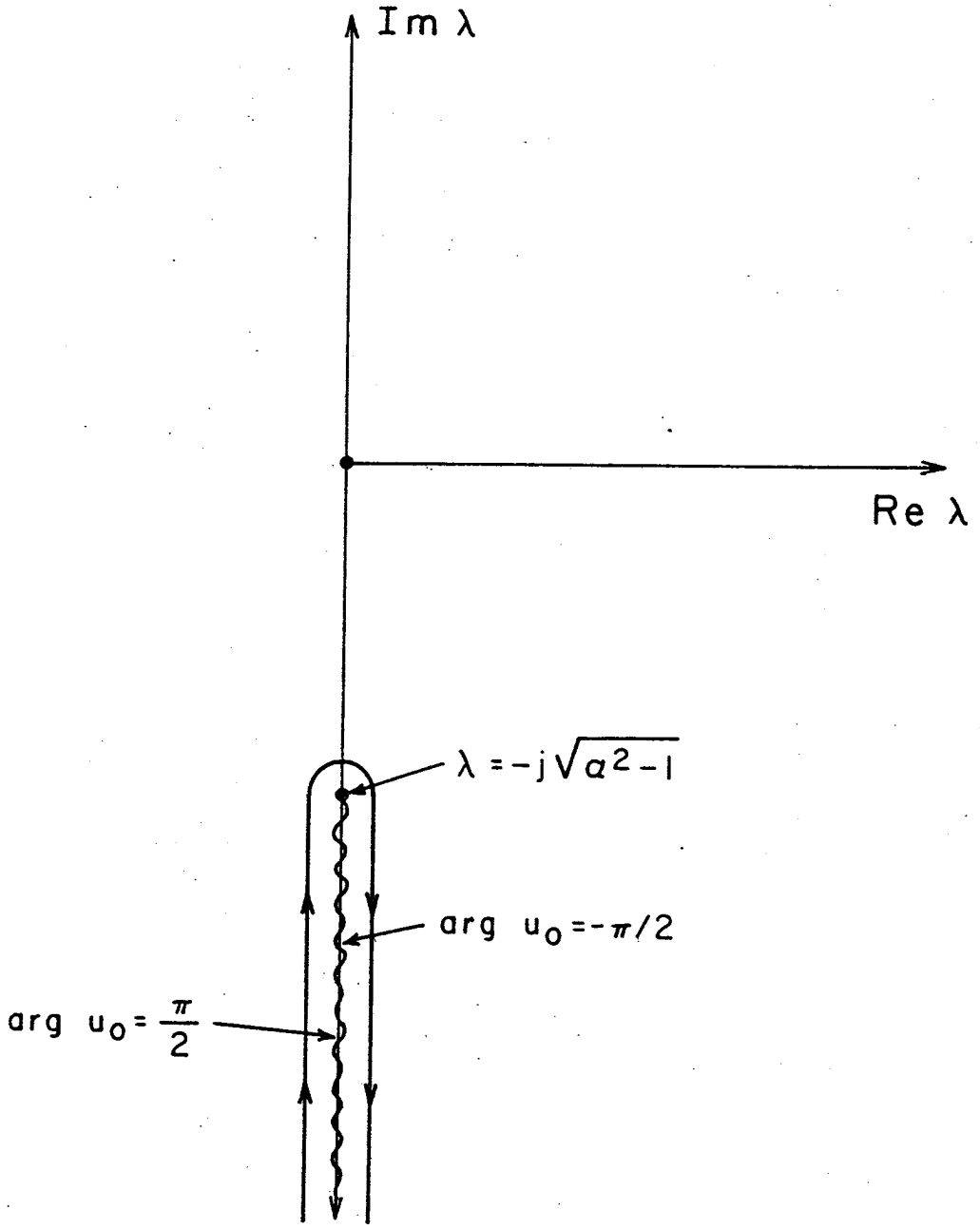

Fig. A.4.

$$I_6 = \frac{k_o d}{n^2} \ln\left(\frac{\sqrt{\alpha^2 - 1}}{2\sqrt{n^2 - \alpha^2}}\right) - \frac{\pi}{2\sqrt{n^2 - \alpha^2}} \tan^{-1}\left(\frac{\sqrt{\alpha^2 - 1}}{\sqrt{n^2 - \alpha^2}}\right) + I_7 \, . \tag{A.83}$$

In Eq. (A.83),

$$I_7 = \int_0^\infty \tan^{-1}\left(\frac{n^2}{\tau k_o d}\right) \frac{d\tau}{\tau^2 + n^2 - \alpha^2}$$

$$= \frac{n^2 k_o d}{\sqrt{n^2 - \alpha^2}} \int_0^\infty \tan^{-1}\left(\frac{\tau}{\sqrt{n^2 - \alpha^2}}\right) \frac{d\tau}{(k_o d)^2 \tau^2 + n^2} \, . \tag{A.84}$$

Eq. (A.84) is modified by adding and subtracting a term which is similar to the one above, except that the arctangent in the integrand is replaced by a two term large argument expansion. Thus,

$$I_7 = \frac{n^2 k_o d}{\sqrt{n^2 - \alpha^2}} \int_0^\infty \left[\tan^{-1}\left(\frac{\tau}{\sqrt{n^2 - \alpha^2}}\right) - \frac{\frac{\pi}{2}\tau}{\tau + \frac{2}{\pi}\sqrt{n^2 - \alpha^2}}\right]$$

$$+ \frac{d\tau}{\tau + \frac{2}{\pi}\sqrt{n^2 - \alpha^2}} + \int_0^\infty \frac{\frac{\pi}{2}\tau \, d\tau}{(\tau + \frac{2}{\pi}\sqrt{n^2 - \alpha^2})((k_o d\tau)^2 + n^4)} \, . \tag{A.85}$$

The first integral in Eq. (A.85) has already been evaluated, and it is given by Eq. (A.27). The second integral on the right side of Eq. (A.85) can be expanded by the method of partial fractions to give

$$\frac{\pi}{2}\int_0^\infty \frac{\tau\, d\tau}{(\tau + \frac{2}{\pi}\sqrt{n^2-\alpha^2})((k_o d\tau)^2 + n^4} = \frac{(k_o d)^2\sqrt{n^2-\alpha^2}}{n^4}$$

$$\times \int_0^\infty \frac{\tau\, d\tau}{(k_o d)^2\tau^2 + n^4} + \frac{\pi}{2}\int_0^\infty \frac{d\tau}{(k_o d)^2\tau^2 + n^4}$$

$$= \frac{1}{n^4}\left[\left(\frac{\pi}{2}\right)^2 \frac{n^2}{k_o d} + \sqrt{n^2-\alpha^2}\ \ell n\left(\frac{2k_o d}{\pi n^2}\sqrt{n^2-\alpha^2}\right)\right] \qquad (A.86)$$

Applying Eqs. (A.86) and (A.27) to (A.85) yields

$$I_7 = \frac{k_o d}{n^2}\ \ell n\left(\frac{k_o d\sqrt{n^2-\alpha^2}}{n^2}\right) - \frac{k_o d}{n^2} + \frac{\left(\frac{\pi}{4}\right)^2}{\sqrt{n^2-\alpha^2}} \quad . \qquad (A.87)$$

From Eqs. (A.87) and (A.83), I_6 is given by

$$I_6 = \frac{k_o d}{n^2}\left[\ell n\left(\frac{k_o d\sqrt{\alpha^2-1}}{2n^2}\right) - 1\right] - \frac{\pi}{2\sqrt{n^2-\alpha^2}}\tan^{-1}\left(\frac{\sqrt{\alpha^2-1}}{\sqrt{n^2-\alpha^2}}\right)$$

$$+ \frac{\pi^2}{4\sqrt{n^2-\alpha^2}} \quad . \qquad (A.88)$$

The approximate formula for $\hat{\upsilon}$ is obtained by substituting Eqs. (A.88) and (A.37) into Eq. (A.79). Hence,

$$\hat{\upsilon} = k_o d[-\ell n\ 2\pi + \frac{1}{n^2}(\ell n\ k_o d\sqrt{\alpha^2-1} + \gamma - 1) + 2Q_0]$$

$$+ \frac{\pi}{2\sqrt{n^2-\alpha^2}}\tan^{-1}\left(\frac{\sqrt{n^2-\alpha^2}}{\sqrt{\alpha^2-1}}\right) \quad . \qquad (A.89)$$

Inserting Eqs. (A.89) and (A.78) into Eq. (A.2) yields

$$\hat{\chi} = 2 \tan^{-1}\left[\frac{\alpha^2}{\sqrt{n^2-\alpha^2}}\left(\frac{k_o d}{\pi}\right)\left\{\left(1-\frac{1}{n^2}\right)\left[\ln\left(\frac{1}{k_o d\sqrt{\alpha^2-1}}\right)\right.\right.\right.$$

$$\left.\left.\left.+\gamma-1\right]+2Q_o\right\}\right] + \frac{2k_o d}{\pi}\sqrt{n^2-\alpha^2}\left[-\ln 2\pi\right.$$

$$\left.+\frac{1}{n^2}\left(\ln(k_o d\sqrt{\alpha^2-1})+\gamma-1\right)+2Q_o\right] \qquad (1<\alpha<n) \quad (A.90)$$

Since $n\,k_o d \ll 1$, the arctangent function in Eq. (A.90) can be replaced by its small argument expansion. Thus, $\hat{\chi}$ simplifies to

$$\hat{\chi} \simeq \frac{2k_o d}{\pi}\left\{\frac{n^2}{\sqrt{n^2-\alpha^2}}\left[\left(1-\frac{1}{n^2}\right)\left(1-\gamma+\ln\left(\frac{1}{k_o d\sqrt{\alpha^2-1}}\right)\right)\right.\right.$$

$$\left.\left.+2Q_o\right]-\sqrt{n^2-\alpha^2}\left[1-\gamma+\ln\left(\frac{2\pi}{k_o d\sqrt{\alpha^2-1}}\right)\right]\right\} \qquad (A.91)$$

for $1<\alpha<n$.

It should be noted that the use of the small argument expansion is contingent on α not being too close to n. In practical situations when α is close to n, α normally has a value which results in a ratio $\frac{(k_o d)\alpha^2}{\pi\sqrt{n^2-\alpha^2}} \ll 1$. This fact allows the small argument expansion of the arctangent term.

Eqs. (A.78) and (A.89) are derived in a manner which makes them valid in the range $1<\alpha<n$. A question arises, however, when the equations are to be applied in the range

$0 \leq \alpha < 1$. Clearly, if one has knowledge about which branch of $\sqrt{\alpha^2 - 1}$ must be selected in this range, then Eqs. (A.78) and (A.89) can be extended into the range $0 \leq \alpha < 1$ by the principle of analytic continuation. The solution for $\hat{\Gamma}$ when $\alpha = 0$, as is given by Eq. (A.38), provides the essential information. A comparison of Eqs. (A.38) and (A.91) indicates that the proper choice of branch is given by

$$\sqrt{\alpha^2 - 1} = +j\sqrt{1 - \alpha^2} \quad . \tag{A.92}$$

Having selected the proper branch, the solution of Eqs. (A.78) and (A.89) can be extended into the range $0 \leq \alpha < 1$ as long as α is not too close to 1 or n. As a check, the solution for agrees with that given by Kuester [5], who uses a more general approach to generate an expression for $\hat{\chi}$ that is valid in the range $0 \leq \alpha < n$.

APPENDIX B

COMPUTER PROGRAM THAT EVALUATES

THE WIENER-HOPF REFLECTION COEFFICIENT

```
      PROGRAM JOHNK(INPUT,TAPE5=INPUT,OUTPUT,TAPE6=OUTPUT)
C     MAIN PROGRAM
C   THIS PROGRAM EVALUATES THE WIENER-HOPF REFLECTION COEFFICIENT
C OF EQ. 2-9 BY MEANS OF NUMERICAL INTEGRATION OF EQS. 2-10 AND 2-11.
C THE VARIABLES USED IN THIS PROGRAM HAVE THE FOLLOWING MEANINGS:
C ALPHA CORRESPONDS TO THE VARIABLE ALPHA.IT IS DECLARED AS A COMPLEX
C QUANTITY,BUT ONLY THE REAL PART IS USED.
C FREQ IS THE FREQUENCY OF OPERATION.
C N IS THE INDEX OF REFRACTION.
C EPSR IS THE RELATIVE PERMITTIVITY.
C UREL IS THE RELATIVE PERMEABILITY.
C KO IS THE FREE SPACE WAVE NUMBER.
C KD IS THE ELECTRICAL SUBSTRATE THICKNESS.
C LAMDA CORRESPONDS TO THE GREEK LETTER LAMBDA, AND IT IS THE
C VARIABLE OF INTEGRATION.
      DIMENSION AFRE(7)
       COMPLEX CADM,FEIA,U6,U7,FEIMD,SM1,XXX
       COMPLEX KUE1,KUE2,SUMFM,SUMFMC,S30,S31,RFC
       COMPLEX R1P,R1PP,T01,T02,FA1,FA1D,THR,SHR
       COMPLEX U01,U02,S21,XAPH1,XAPH,U1,U2,U3,U4,U5
       COMPLEX RFE,RF1,RF2,RF3,ANS,CX1,CX2,SUM,VAL
       COMPLEX FEI,DELTA,VALD,SUMD,ANSD,ALPHA,RD,RF
       REAL L,KO,L0,L1,L2,L3,L4,L5,LAMS,LM
       REAL L6,L7,L8,L9,L10,L11,MAGR
       REAL LAMDA,KD,EPSR,UREL,N,PI
       REAL L1P,L2P,LCOR
      EXTERNAL FEIM
      EXTERNAL FEI
      EXTERNAL DELTA
      COMMON/PRMTRS/KD,EPSR,UREL,N,PI,ALPHA
100   FORMAT(2F15.8)
105   FORMAT(2F15.8)
110   FORMAT(6F15.8,1F15.8,1F15.8,1F15.8)
111   FORMAT(8F15.8)
      XD=0.
      EPSR=2.9
      UREL=1.0
       N=SQRT(UREL*EPSR)
       PI=4.0*ATAN(1.0)
106    FORMAT(1F15.8)
107   FORMAT(3F15.8)
108   FORMAT(6F15.8)
109   FORMAT(1F15.8,1F15.8,1F15.8,1F15.8,2F15.8)
      I=1
      AFRE(1)=842.5E+06
      AFRE(2)=928.8E+06
      AFRE(3)=1.032E+09
      AFRE(4)=1.167E+09
      AFRE(5)=1.224E+09
      AFRE(6)=1.318E+09
      AFRE(7)=1.405E+09
      FREQ=AFRE(I)
      ALPHA=(.50695,0.)
      L=25.6E-03
      D=9.2E-03
```

```
      UEPS=1.0/(3.0E+08)
      KO=2.0*PI*UEPS*FREQ
      KD=KO*D
      ZL2=0.
      SUM=(0.,0.)
      ZL1=0.
      ZL2=0.
      X=0.
C THIS SECTION OF THE PROGRAM DETERMINES THE SINGULARITY LOCATIONS.
      EPS=1.0E-06
       LAMS=1.0+(KD*KD/2.0)*(N*N-1.0)*(N*N-1.0)*(1.0/EPSR)*(1.0/EPSR)
      TAUO=1.0/KD
      LM=AMAX1(5.0*N,5.0*TAUO)
      CX1=(0.,-1.0)*CSQRT(ALPHA*ALPHA-1.0)
      CX2=(0.,-1.0)*CSQRT(ALPHA*ALPHA-LAMS*LAMS)
      RCX1=REAL(CX1)
      RCX2=REAL(CX2)
      IF(RCX1.GT.0.)GO TO 3
      GO TO 4
 3    S1=RCX1
      GO TO 5
 4    S1=0.
 5    CONTINUE
      IF(RCX2.GT.0.)GO TO 7
      GO TO 8
 7    S2=RCX2
      GO TO 9
 8    S2=0.
 9    CONTINUE
      S3=CSQRT(N*N-ALPHA*ALPHA)
      WRITE(6,107)S1,S2,S3
C IN THIS SECTION,THE INTEGRATION LIMITS ARE CALCULATED.
      LO=0.
      L1=.9*S1
      L2=S1*(1.0-1.0E-05)
      L3=S1*(1.0+1.0E-05)
      L4=S2*(1.0-1.0E-05)
      L5=S2*(1.0+1.0E-05)
      L6=S2*1.1
      L7=.8*S3
      L8=.99*S3
      L9=1.01*S3
      L10=1.2*S3
      L11=2.0*S3
      WRITE(6,108)LO,L1,L2,L3,L4,L5
      WRITE(6,108)L6,L7,L8,L9,L10
      WRITE(6,108)L11
      IF(RCX1.GT.0.)GO TO 10
      IF(RCX2.GT.0.)GO TO 20
      GO TO 26
C THIS SECTION DEALS WITH THE INTEGRATION OF EQ. 2-15.
 10   ZL2=L1
      IF(RCX1.LT.1.0E-05)GO TO 20
      FL=0.
      CALL INTER(ZL1,ZL2,EPS,1024,FEI,VAL,XX,G)
      X=X+XX
```

```
      SUM=SUM+VAL
      WRITE(6,109)FL,ZL1,ZL2,XX,VAL
11     CONTINUE
      ZL1=L1
      ZL2=L2
      FL=1.0
      CALL INTER(ZL1,ZL2,EPS,1024,FEI,VAL,XX,G)
      X=X+XX
      SUM=SUM+VAL
      WRITE(6,109)FL,ZL1,ZL2,XX,VAL
19    CONTINUE
      IF(L3.GT.L4)GO TO 25
      ZL1=L3
20    ZL2=L4
      IF(RCX1.LT.1.0E-05)ZL1=1.0E-05
      FL=2.0
      CALL INTER(ZL1,ZL2,EPS,1024,FEI,VAL,XX,G)
      X=X+XX
      SUM=SUM+VAL
      WRITE(6,109)FL,ZL1,ZL2,XX,VAL
25    ZL1=L5
      IF(L5.GT.L8)GO TO 29
      IF(L3.GT.L6)GO TO 26
      FL=3.0
      ZL2=L6
      CALL INTER(ZL1,ZL2,EPS,1024,FEI,VAL,XX,G)
      WRITE(6,109)FL,ZL1,ZL2,XX,VAL
      X=X+XX
      SUM=SUM+VAL
260   CONTINUE
      ZL1=L6
26    IF(L3.GT.L7.OR.L6.GT.L7)GO TO 27
      FL=4.0
      ZL2=L7
      CALL INTER(ZL1,ZL2,EPS,1024,FEI,VAL,XX,G)
      WRITE(6,109)FL,ZL1,ZL2,XX,VAL
      X=X+XX
      SUM=SUM+VAL
      ZL1=L7
27    IF(L3.GT.L8)GO TO 29
      ZL2=L8
      FL=5.0
      CALL INTER(ZL1,ZL2,EPS,1024,FEI,VAL,XX,G)
      WRITE(6,109)FL,ZL1,ZL2,XX,VAL
      X=X+XX
      SUM=SUM+VAL
29    CONTINUE
      ZL1=L9
      ZL2=L10
      FL=6.0
      CALL INTER(ZL1,ZL2,EPS,1024,FEI,VAL,XX,G)
      WRITE(6,109)FL,ZL1,ZL2,XX,VAL
      X=X+XX
      SUM=SUM+VAL
290    CONTINUE
      ZL1=L10
```

```
          FL=7.0
          ZL2=L11
          CALL INTER(ZL1,ZL2,EPS,1024,FEI,VAL,XX,G)
          WRITE(6,109)FL,ZL1,ZL2,XX,VAL
          SUM=SUM+VAL
C    ADAPTIVE INTEGRATION.
 30       ZL1=ZL2
          ZL2=ZL1+TAUO
          FL=8.0
          CALL INTER(ZL1,ZL2,EPS,1024,FEI,VAL,XX,G)
          SUM=SUM+VAL
          X=X+XX
          WRITE(6,109)FL,ZL1,ZL2,XX,VAL
          IF(ZL2.GE.LM)GO TO 40
          GO TO 30
 40       CONTINUE
          WRITE(6,100)SUM
C HERE,THE CORRECTION TERM FOR EQ. 2-15 IS CALCULATED AND ADDED TO
C THE FINITE RANGE INTEGRAL.
         CRFEI1=((2.+EPSR)*(EPSR-1.0))/(2.0*(1.0+EPSR))
          CRFEI=CRFEI1/(3.0*ZL2*ZL2*ZL2)
          WRITE(6,100)CRFEI
          A10=ALOG(KD*(1.0+EPSR)*SQRT(N*N-1.0)/EPSR)
          A11=(.5/S3)*ALOG((ZL2-S3)/(ZL2+S3))
          A12=A11*A10
          WRITE(6,100)A12
          SI1=1.0/(2.0*(N*N-1.0))
          SI2=1.0-(2.0*KD*SQRT(N*N-1.0))
          SI=(L9-L8)*SI1*SI2
          WRITE(6,100)SI
          CRFEI=A12+SI+CRFEI
          WRITE(6,100)CRFEI
          SUM=SUM+CRFEI
          WRITE(6,100)SUM
          RF1=CSQRT(ALPHA*ALPHA-1.0)
          RF2=(0.,1.0)*CSQRT(N*N-ALPHA*ALPHA)
          RF3=CSQRT(N*N-1.0)
          RFE=(0.,-1.0)*CLOG((RF1+RF2)/RF3)
C  ANS IS FE OF EQ. 2-12.
          ANS=RFE-(2./PI)*SUM*CSQRT(N*N-ALPHA*ALPHA)
          WRITE(6,100)RFE
          WRITE(6,100)ANS
          IF(ALPHA.EQ.0.)GO TO 700
C THIS SECTION PERFORMS THE INTEGRATION OF EQ. 2-14.
C    S1 AND S2 ARE THE SAME AS BEFORE.
*******
          ZL1=0.
          ZL2=0.
          SUMD=(0.,0.)
          VALD=(0.,0.)
          SP3=(1.0/(UREL*KD))*(1.0/(UREL*KD))
          S3=CSQRT(SP3-ALPHA*ALPHA+1.0)
C         RECALCULATE THE LIMITS AROUND S3.
          L7=.8*S3
          L8=.99*S3
          L9=1.01*S3
```

```
      L10=1.2*S3
      L11=2.0*S3
      WRITE(6,108)L7,L8,L9,L10,L11
      L1P=ALPHA
      L2P=5.0*ALPHA
      IF(RCX1.GT.0.)GO TO 60
      IF(RCX2.GT.0.)GO TO 70
      GO TO 80
60     CONTINUE
      IF(RCX1.LT.1.0E-05)GO TO 70
      IF(L1P.GT.L1)GO TO 55
      ZL1=L0
      ZL2=L1P
      CALL INTER(ZL1,ZL2,EPS,1024,DELTA,VALD,XXD,G)
      SUMD=SUMD+VALD
      XD=XD+XXD
      FL=10.0
      WRITE(6,109)FL,ZL1,ZL2,XXD,VALD
      IF(L2P.GT.L1)GO TO 54
      ZL1=L1P
      ZL2=L2P
      CALL INTER(ZL1,ZL2,EPS,1024,DELTA,VALD,XXD,G)
      SUMD=SUMD+VALD
      XD=XD+XXD
      FL=11.0
      WRITE(6,109)FL,ZL1,ZL2,XXD,VALD
      ZL1=L2P
      ZL2=L1
      CALL INTER(ZL1,ZL2,EPS,1024,DELTA,VALD,XXD,G)
      SUMD=SUMD+VALD
      XD=XD+XXD
      FL=12.0
      WRITE(6,109)FL,ZL1,ZL2,XXD,VALD
      GO TO 56
54     CONTINUE
      ZL1=L1P
      ZL2=L1
      CALL INTER(ZL1,ZL2,EPS,1024,DELTA,VALD,XXD,G)
      SUMD=SUMD+VALD
      XD=XD+XXD
      FL=13.0
      WRITE(6,109)FL,ZL1,ZL2,XXD,VALD
      GO TO 56
55     CONTINUE
      ZL1=L0
      ZL2=L1
      CALL INTER(ZL1,ZL2,EPS,1024,DELTA,VALD,XXD,G)
      SUMD=SUMD+VALD
      XD=XD+XXD
      FL=14.0
      WRITE(6,109)FL,ZL1,ZL2,XXD,VALD
56     CONTINUE
      ZL1=L1
      ZL2=L2
      CALL INTER(ZL1,ZL2,EPS,1024,DELTA,VALD,XXD,G)
      SUMD=SUMD+VALD
```

```
      XD=XD+XXD
      FL=15.0
      WRITE(6,109)FL,ZL1,ZL2,XXD,VALD
      IF(L3.GT.L4)GO TO 75
      ZL1=L3
70    ZL2=L4
      IF(RCX1.LT.1.0E-05)ZL1=1.0E-05
      CALL INTER(ZL1,ZL2,EPS,1024,DELTA,VALD,XXD,G)
      SUMD=SUMD+VALD
      XD=XD+XXD
      FL=16.0
      WRITE(6,109)FL,ZL1,ZL2,XXD,VALD
75     CONTINUE
      ZL1=L5
       ZL2=L6
      CALL INTER(ZL1,ZL2,EPS,1024,DELTA,VALD,XXD,G)
      SUMD=SUMD+VALD
      XD=XD+XXD
      FL=17.0
      WRITE(6,109)FL,ZL1,ZL2,XXD,VALD
      ZL1=L6
      GO TO 80
76    CONTINUE
      IF(L3.GT.L7.OR.L6.GT.L7)GO TO 77
      ZL2=L7
      CALL INTER(ZL1,ZL2,EPS,1024,DELTA,VALD,XXD,G)
      SUMD=SUMD+VALD
      XD=XD+XXD
      FL=18.0
      WRITE(6,109)FL,ZL1,ZL2,XXD,VALD
      ZL1=L7
77    CONTINUE
      IF(L3.GT.L8)GO TO 79
      ZL2=L8
      CALL INTER(ZL1,ZL2,EPS,1024,DELTA,VALD,XXD,G)
      SUMD=SUMD+VALD
      XD=XD+XXD
      FL=19.0
      WRITE(6,109)FL,ZL1,ZL2,XXD,VALD
79    CONTINUE
      ZL1=L9
      ZL2=L10
      CALL INTER(ZL1,ZL2,EPS,1024,DELTA,VALD,XXD,G)
      SUMD=SUMD+VALD
      XD=XD+XXD
      FL=20.0
      WRITE(6,109)FL,ZL1,ZL2,XXD,VALD
      ZL1=L10
      ZL2=L11
      CALL INTER(ZL1,ZL2,EPS,1024,DELTA,VALD,XXD,G)
      SUMD=SUMD+VALD
      FL=21.0
      WRITE(6,109)FL,ZL1,ZL2,XXD,VALD
C ADAPTIVE INTEGRATION FOR DELTA.
80    CONTINUE
      ZL1=ZL2
```

```
            ZL2=ZL1+TAUO
            CALL INTER(ZL1,ZL2,EPS,1024,DELTA,VALD,XXD,G)
            SUMD=SUMD+VALD
            XD=XD+XXD
            FL=22.0
            WRITE(6,109)FL,ZL1,ZL2,XXD,VALD
            IF(ZL2.GE.LM)GO TO 90
            GO TO 80
   90       CONTINUE
   C HERE THE CORRECTION TERM FOR EQ2-14 IS ADDED TO THE FINITE
   C RANGE INTEGRATION.
            CR1=(EPSR-1.0)*EPSR/(1.0+EPSR)
             CR2=.5*(3.0+EPSR)/(1.0+EPSR)
            CRDEL1=CR1*CR2
            CRDEL=CRDEL1/(3.0*ZL2*ZL2*ZL2)
            CRDEL2=EPSR*(UREL+1.0)/(1.0+EPSR)
            CRDEL2=(1.0/ZL2)*ALOG(CRDEL2)
            CRDEL=CRDEL+CRDEL2
   C SUMD IS THE INTEGRAL OF EQ.2-14
            SUMD=SUMD+CRDEL
            WRITE(6,100)SUMD
            ANSD=(ALPHA/PI)*SUMD
            GO TO 800
   700      ANSD=0.
   800        CONTINUE
            WRITE(6,100)ANSD
            U1=(0.,-1.0)
            U2=(0.,1.0)
            U3=U1*CSIN(U2*ANSD)/CCOS(U2*ANSD)
            U4=CSQRT(N*N-ALPHA*ALPHA)
           U5=(U4+U2*ALPHA*U3)/CSQRT(ALPHA*U3*ALPHA*U3+N*N-ALPHA*ALPHA)
            XAPH=U1*2.0*CLOG(U5)-ANS
   C XAPH1 IS THE RIGHT SIDE OF EQ. 2-21 WITH M=0.
            XAPH1=XAPH/CSQRT(N*N-ALPHA*ALPHA)
   C RFC IS THE WIENER-HOPF REFLECTION COEFFICIENT OF EQ. 2-9.
            RFC=CEXP(XAPH*U2)
   C MAGR IS THE MAGNITUDE OF THE WIENER-HOPF REFLECTION COEFFICIENT.
            MAGR=SQRT(AIMAG(RFC)*AIMAG(RFC)+REAL(RFC)*REAL(RFC))
   C PHASE IS THE PHASE OF THE W-H REFLECTION COEFFICIENT.
            PHASE=ATAN2(AIMAG(RFC),REAL(RFC))
   C PTR IS THE NORMALIZED TRANSMITTED POWER.
            PTR=1.-MAGR*MAGR
            WRITE(6,100)KD
            WRITE(6,110)ALPHA,XAPH1,XAPH,MAGR,PHASE,PTR
            CADM=(1-RFC)/(1+RFC)
            WRITE(6,100)CADM
            GO TO 500
   C THIS SECTION OF PROGRAM IS NOT NECESSARY TO COMPUTE THE W-H
   C REFLECTION COEFFICIENT,BUT IT IS USED TO OBTAIN A MORE EXACT
   C PROPAGATION CONSTANT.
   C FOR MORE DETAILS, CONSULT REFERENCE 5
            ALPR=REAL(ALPHA)
   ********
            EL=34.707209E-03
            BESF=2.0*KO*EL*SQRT(ALPR*ALPR-1.0)
           BES1=BESSKO(BESF)
```

```
      KUE1=XAPH/(2.,0.)-KO*L*CSQRT(N*N-ALPHA*ALPHA)
      KUE1=CSIN(KUE1)
      U6=CCOS(U2*ANSD)
      U6=U6*U6
      U6=(1.0,0.)/U6
      KUE2=(-KD/PI)*UREL*CSQRT(ALPHA*ALPHA-1.0)
      KUE2=KUE2*(CSQRT(ALPHA*ALPHA-1.0)-ALPHA*U3)
      KUE2=KUE2*BES1
      KUE2=KUE2/CSQRT(N*N-ALPHA*ALPHA*U6)
      WRITE(6,111)L
      WRITE(6,111)EL
      WRITE(6,111)KUE1,KUE2
500   CONTINUE
      STOP
      END
```

```
      COMPLEX FUNCTION DELTA(X)
C COMPUTE THE INTEGRAND OF EQ.2-14.
       COMPLEX Z1,Z2,Z3,Z4,Z5,Z6,Z7
      COMPLEX U0,UN
      COMPLEX ALPHA
       REAL KD,EPSR,UREL,N,PI,LAMDA
      COMMON/PRMTRS/KD,EPSR,UREL,N,PI,ALPHA
      LAMDA=X
      U0=CSQRT(LAMDA*LAMDA+ALPHA*ALPHA-1.0)
      UN=CSQRT(LAMDA*LAMDA+ALPHA*ALPHA-N*N)
      Z1=UN*KD
      Z2=(0.,-1.0)
      Z3=(0.,1.0)
       Z4=(Z2*CSIN(Z3*Z1))/CCOS(Z3*Z1)
      Z5=1.0+UREL*(U0/UN)*Z4
      Z6=EPSR*U0+UN*Z4
      Z7=1.0/(ALPHA*ALPHA+LAMDA*LAMDA)
      DELTA=Z7*(CLOG(U0*EPSR)+CLOG(Z5)-CLOG(Z6))
      RETURN
      END
```

```
      COMPLEX FUNCTION FEI(X)
C COMPUTE THE INTEGRAND OF EQ.2-15.
      COMPLEX ALPHA,UN,UO
       COMPLEX Y1,Y2,Y3,Y4,Y5,Y6,Y7
       REAL KD,EPSR,UREL,N,PI,LAMDA
       COMMON/PRMTRS/KD,EPSR,UREL,N,PI,ALPHA
       LAMDA=X
       UO=CSQRT(LAMDA*LAMDA+ALPHA*ALPHA-1.0)
        UN=CSQRT(LAMDA*LAMDA+ALPHA*ALPHA-N*N)
       Y1=UN*KD
       Y2=(0.,-1.0)
       Y3=(0.,1.0)
        Y4=(Y2*CSIN(Y3*Y1))/CCOS(Y3*Y1)
       Y5=(EPSR/(KD*SQRT(N*N-1.0)))*(Y4/UN)
       Y6=EPSR*UO+UN*Y4
       Y7=1.0/(LAMDA*LAMDA-(N*N-ALPHA*ALPHA))
       FEI=Y7*(2.0*CLOG(UO)+CLOG(Y5)-CLOG(Y6))
       RETURN
        END
```

```
      SUBROUTINE INTER(A,B,EPS,NSTEP,FCN,VALUE,X,G)
C THIS SUBROUTINE PERFORMS A ROMBERG INTEGRATION OF A COMPLEX
C FUNCTION ALONG THE REAL AXIS.
      COMPLEX FCN,FCNA,FCNB,FCNXI,T,SUM,  QX1,QX2,VALUE ,Q(16)
      LOGICAL G
      H=B-A
      FCNA=FCN(A)
      FCNB=FCN(B)
      T=H*(FCNA+FCNB)/2.
      NX=1
      N=1
    1 K=2**N
      H=H/2.
      SUM=(0.0,0.0)
      DO 2 I=1,NX
      XI=2.*FLOAT(I)-1.
      FCNXI=FCN(A+XI*H)
    2 SUM=SUM+FCNXI
      T=T/2.+H*SUM
      Q(N)=  (T+H*SUM)*2.0/3.
      IF (N-2) 10,3,3
    3 F=4.
      DO 4 J=2,N
      I=N+1-J
      F=F*4.
    4 Q(I)=Q(I+1)+(Q(I+1)-Q(I))/(F-1.)
      IF (N-3) 9,5,5
    5 XREAL=ABS(REAL(Q(1)-QX2))+ABS(REAL(QX2-QX1))
      XIMAG=ABS(AIMAG(Q(1)-QX2))+ABS(AIMAG(QX2-QX1))
      X=AMAX1(XREAL,XIMAG)
      COMP=X-3.*EPS
      IF (COMP) 11,11,8
    8 IF (NSTEP-K) 11,11,9
    9 QX1=QX2
   10 QX2=Q(1)
   12 NX=NX*2
      N=N+1
      GO TO 1
   11 VALUE=Q(1)
      G=NSTEP.LT.K
      RETURN
        END
```

```
      FUNCTION BESSKO(X)
C THIS SUBPROGRAM  COMPUTES THE MODIFIED BESSEL FUNCTION OF A
C REAL ARGUEMENT.
C THIS SUBPROGRAM IS NOT NECESSARY,BUT IT WAS USED TO OBTAIN A
C MORE ACCURATE PROPAGATION CONSTANT.
C     CONSULT REFERENCE 5 FOR MORE DETAILS
      REAL I0,KM0
      I0=0.
      KM0=0.
      Z=X
      IF(Z.GE.2.)GO TO 20
      Z=Z/3.75
      I0=1.0+3.5156229*Z*Z+3.0899424*(Z**4)
      I0=I0+1.2067492*(Z**6)
      I0=I0+.2659732*(Z**8)
      I0=I0+.0360468*(Z**10)
      I0=I0+.0045813*(Z**12)
      Z=Z*3.75
      KM0=-I0*ALOG(Z/2.0)-.57721566
      KM0=KM0+.42278420*(Z/2.)**2
      KM0=KM0+.23069756*(Z/2.)**4
      KM0=KM0+.03488590*(Z/2.)**6
      KM0=KM0+.00262698*(Z/2.)**8
      KM0=KM0+.00010750*(Z/2.)**10
      KM0=KM0+.00000740*(Z/2.)**12
      GO TO 30
20    CONTINUE
      KM0=1.25331414-.07832358*(2./Z)
      KM0=KM0+.02189568*(2./Z)**2
      KM0=KM0-.01062446*(2./Z)**3
      KM0=KM0+.00587872*(2./Z)**4
      KM0=KM0-.00251540*(2./Z)**5
      KM0=KM0+.00053208*(2./Z)**6
      KM0=(KM0/SQRT(Z))*EXP(-Z)
30    CONTINUE
      BESSKO=KM0
      RETURN
      END
```